Millimeter-wave Superconducting and Quantum Non-linear Kinetic Inductance Circuits and Devices

by

Farzad Faramarzi

A Dissertation Presented in Partial Fulfillment
of the Requirements for the Degree
Doctor of Philosophy

Approved January 2023 by the
Graduate Supervisory Committee:

Philip Mauskopf, Chair
Peter Day
Ralph Chamberlin
William Terrano

ARIZONA STATE UNIVERSITY

May 2023

ABSTRACT

Millimeter wave technologies have various applications in many science and engineering disciplines, from astronomy and chemistry to medicine and security. The superconducting circuit technology, in particular mm-wave, is one of the most appealing candidates due to their extremely low loss, near quantum-limited noise performance, and scalable fabrication. Two main immediate applications of these devices are in astronomical instrumentation and quantum computing and sensing. The kinetic inductance caused by the inertia of cooper pairs in thin-film superconductors dominates over the geometric inductance of the superconducting circuit. The nonlinear response of the kinetic inductance to an applied field or current provides a Kerr-like medium. This nonlinear platform can be used for mixing processes, parametric gain, and anharmonic resonance.

In this thesis, I present the development of an mm-wave superconducting on-chip Fourier transform spectrometer (SOFTS) based on a nonlinear kinetic inductance of superconducting thin films. The circuit elements of the SOFTS device include a quadrature hybrid and current-controllable superconducting transmission lines in an inverted microstrip geometry. Another similar device explored here is a kinetic inductance traveling wave parametric amplifier (KI-TWPA) with wide instantaneous bandwidth, quantum noise limited performance, and high dynamic range as a candidate for the readout of cryogenic detectors and superconducting qubits. I report four-wave mixing gain measurements of $\sim$ 30 dB from 0.2 - 5 GHz in KI-TWPAs made of capacitively shunted microstrip lines. I show that the gain can be tuned over the above-mentioned frequency range by changing the pump tone frequency. I also discuss the measured gain ($\sim$ 6 dB) of a prototype mm-wave KI-TWPA in the 75 - 100 GHz frequency range. Finally, I present, for the first time, the concept and simulation of a kinetic inductance qubit I named Kineticon. The qubit exploits the nonlinearity of the kinetic inductance of a very thin nanowire connecting two capacitive pads with a resonant frequency of ~ 96 GHz. the qubit is embedded in an mm-wave aluminum cavity. I show that mm-wave anharmonic microstrip resonators made of NbTiN have quality factors $\gtrapprox$ 60,000. These measurements are promising for implementing high-quality factor resonators and qubits in the mm-wave regime.

ACKNOWLEDGMENTS

First and foremost, I owe a great deal of debt to my mother, Nahid, for always being supportive and letting me follow my dreams. Without her, I would not have been the person I am today. My brother, Fardad, has always appreciated my work and was very supportive. I always cherish our conversations about philosophy, art, history, and science, and I truly appreciate his unique point of view. I was privileged to find my significant other during my Ph.D. years and have the support of my spouse, Sasha Sypkens. Not only has Sasha been a wonderful partner in life, but she has also been a great colleague. Without Sasha's help and insight, I can not imagine I would have been able to succeed with my research.

During my five years as a graduate student at ASU, I was exceptionally fortunate to be surrounded by an amazing group of friends who helped me through many life and work struggles and formed a great support group. Jacob Glasby, Jonathan Greenfield, Marko Neric, and Nani Glasby, especially, have been fantastic friends, and I owe a huge deal of my sanity to them. Other friends who have been dear to me and whom I had the privilege of meeting are Ryan Stephenson, Adrian Sinclair, Sam Gordon, Justin Mathewson, Tom and Barb Mozden, Kate Okun, Chris Knill, Shep Bryan, William Munizzi, Sean Tilton, Mathew Mircovich, Jeremy Mainke, Emily Linden, Emily Lunde, Christina Bell, Kathryn Chamberlin, Marco Colangelo, A.J. Woolson, Daniel Lu, Ayush Saurabh, Ed Buie, Harshad Surdi, and late Emily Boyce.

I would also like to thank my tiny furry overlords (kitties), Mr.Muon, The Cat, and Idle, for being super cute and cuddly.

I am very thankful that I could do my Ph.D. research in Professor Philip Mauskopf's group. I'm grateful for the opportunity that professor Mauskopf gave me to work on a variety of projects and gave me the freedom to explore different ideas. I am also very fortunate to have had the privilege of meeting Dr. Peter Day at a conference a few years ago. Peter has been generous enough to allow me to measure some of the devices he designed and made at JPL and taught me a great deal about nonlinear kinetic inductance devices. I can confidently say this thesis would not have been possible without Peter's devices and guidance. Even though Peter is a world-renowned physicist, his exemplary demeanor, such as modesty, kindness, and patience, is inspirational and educational. I would also like to thank Professors Ralph Chamberlin and William Terrano for their support and encouragement and for being extremely approachable and helpful. I would also like to mention Professor John Spence, who is not with us anymore. John was a world-renowned experimental condensed matter physicist and director of the BioXFEL center, with a wide range of expertise from superconductivity to bio-physics. I took Quantum Theory of solids I & II with John, who also served on my committee from 2019 to 2021 until he passed away. I learned a lot from John and enjoyed our one-on-one discussions about solid-state physics. I dearly miss him.

I am indebted to the former electronics engineer in our lab, Hamdi Al-Mani, for teaching me almost everything regarding cryogenic RF/Microwave measurements. Hamdi helped me with the design of a cryostat that we named ForKy, which has been extensively used during my Ph.D. Even though Hamdi left the lab when I was still in my third year, his impact on my life and career is endless. I would also like to thank Dr. Ritoban Basu Thakur for mentoring me with the Superconducting On-chip Fourier Transform Spectrometer. Even with his very busy schedule, he was always happy to help and answer questions any time of the week and day. Rito has been a great mentor, and he has become a very dear friend.

I would also like to thank Professors Tracee Jamison-Hooks, Kevin Schmidt, Chris Groppi, and George Thrichopoulos for all their help and patience with me over the past five years. I also spent a good amount of my time as a Ph.D. student in the ASU

Nanofabrication facility. I want to thank Kevin Hilgers, the director of the Nanofab facility, and Engineers Jaime Quintero, Kevin Nordquist, Carry Sinclair, Scott Ageno, and Arthur Handugan. Without the help of these folks, I would have been lost.

TABLE OF CONTENTS

Page

APPENDIX

LIST OF TABLES

LIST OF FIGURES

Chapter 1

INTRODUCTION

1.1 Motivation

Millimeter wave technology is used in a wide range of disciplines, such as in telecommunication (Lawrence *et al.* (2017)), astronomical instrumentation (Lazareff (2009)), Earth observation (Piironen (2022)), chemistry (Jepsen *et al.* (2010)), medicine (Sizov (2018)), security (Galati *et al.* (2016)), and more recently in quantum sensing and information science (Suleymanzade (2021)). The millimeter wave region of the electromagnetic spectrum is considered to be between 30 GHz - 300 GHz, as shown in Fig. 1.2. In recent years, the need for faster communication and higher bandwidths has pushed the telecommunication community to move towards millimeter-wave 5G technology (Rappaport *et al.* (2013), Roh *et al.* (2014)).

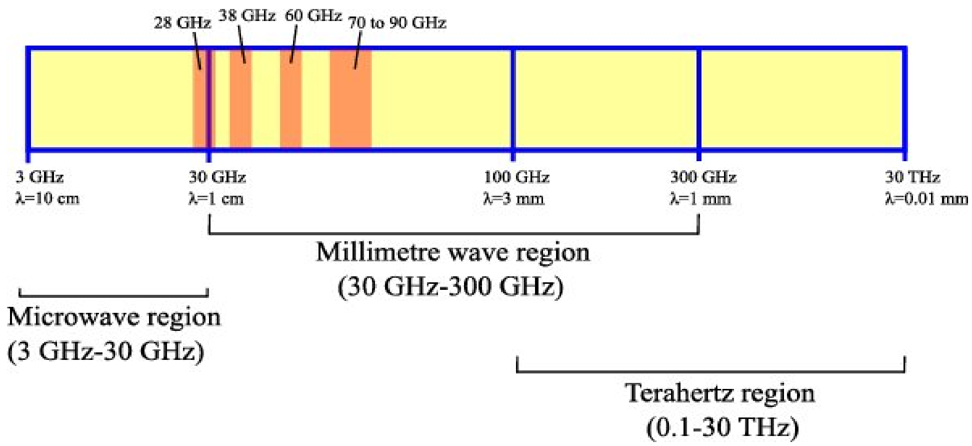

Figure 1.1: The Millimeter-Wave Region of the Electromagnetic Spectrum.(credit: Lawrence *et al.* (2017))

The millimeter and sub-millimeter regions contain rich astronomical signals from the early universe. For example, the Cosmic Microwave Background (CMB) radiation, the remnant light left over from the big bang, peaks in the millimeter waves, and the star formation signal lies in the sub-millimeter range due to redshift (Scott (2006), Hashimoto (2019)). In addition, spectral measurements in the far-infrared band (300 GHz- 20 THz) can tell us the interstellar medium's chemical composition and the protostellar medium's chemical evolution (Auston and Cheung (1985)). Due to this richness, NASA and other space agencies and government entities have invested in the large-scale ground, sub-orbital, and space surveys/missions covering millimeter to micron wave bands to explore the origin and evolution of the universe. Examples of these experiments include Planck (aip (2016)), PICO (Pogosian *et al.* (2019)), Herschel (Pilbratt *et al.* (2010)), HIFI (Swinyard *et al.* (2014)), a future Probe class FIR mission (Leisawitz (2004),Renard *et al.* (2008)), and the space VLBI mission (Gurvits (2020)).

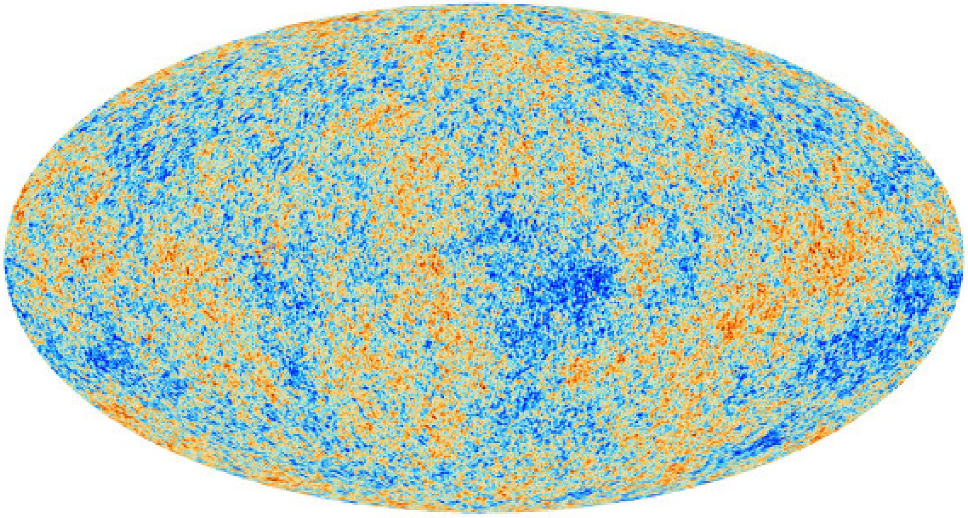

Figure 1.2: The Cosmic Microwave Background (CMB) Radiation the Afterglow of Big Bang Peaks in the Millimeter Wave Region of the Spectrum. (Credit: Planck Satellite, European Space Agency)

The primary technologies used in these experiments are superconducting devices such as Microwave Kinetic Inductance Detectors (MKIDS) (Zmuidzinas (2012)), Superconductor-Insulator-Superconductor (SIS) mixers (Zmuidzinas and Richards (2004)), and Transition-Edge Sensors (TES) (Irwin (1995)), which are used either in direct detection or heterodyne detection schemes.

In more recent years, many research groups have been exploring the possibility of developing mm-wave quantum systems for various applications (Suleymanzade (2021), Faramarzi *et al.* (2021), Anferov *et al.* (2020a), Multani *et al.* (2020)). The high transition frequency in this band allows for higher operating temperatures. For example, the standard quantum limit (SQL) for the W-band range (75 - 110 GHz) is about four Kelvin. Operating these devices would be possible using a He4 fridge which is easier to use and much less expensive than dilution refrigerators used for the state-of-the-art 1-7 GHz qubits and quantum circuits. Another advantage is that the higher available cooling powers at higher temperatures allow large-scale circuits to be implemented in the cryostat.

Millimeter quantum circuits can also bridge the gap between microwave frequency qubits and optical systems as an interface. This will allow for the long-distance transfer of information which will be a great milestone in quantum information. Even though attempts by Mirhosseini *et al.* (2020) using a microwave to optical transducers have shown potential kilo-meter scale entanglement distribution, there are shortcomings, such as low efficiency, short repetition time, and high optical power dissipation, which makes the scalability of such systems very difficult. Due to a smaller frequency gap between mm-wave frequencies and microwave frequencies (1-8 GHz), using mm-wave quantum interconnects instead (Pechal and Safavi-Naeini (2017)) could allow for the construction of lab-scale quantum networks.

Finally, advancements in millimeter-wave quantum technologies can benefit other disciplines, such as astrophysics, chemistry, and engineering, by providing quantum-limited parametric amplifiers, single-photon detectors, emitters, and other mm-wave superconducting on-chip circuits. More research groups have been using quantum circuits for fundamental physics experiments such as dark matter searches (Asztalos *et al.* (2010); Dixit *et al.* (2021); Bartram (2021)). For example, mm-wave parametric amplifiers and single-photon detectors in the hundreds of GHz range can be good candidates for experiments of heaver dark matter candidates (Ramanathan *et al.* (2022)).

In this thesis, we explore a few of the technologies listed above, such as kinetic inductance parametric amplifiers, cavity-qubit systems, interferometers, and on-chip mm-wave resonators.

1.2 Superconductive Devices

1.2.1 Superconductivity

According to the basic quantum theory of solids at $T = 0$ K in metals with perfect crystal structure and without defects, dislocations, or impurities, the electrons behave like a plane wave in a periodic lattice without scattering. This leads to zero electric resistance in the metal. However, at temperatures above absolute zero, where lattice vibrations are significant, and when the material contains defects, dislocations, and impurities, most metals show resistance to the flow of charge carriers (Fig. 1.3 from Rose-Innes and Rhoderick (1994)).

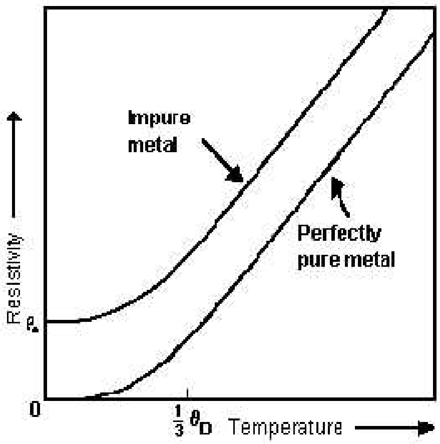

Figure 1.3: The Resistivity Versus Temperature Plot of an Impure Metal and a Perfect Conductor. ρ_0 is the Residual Resistivity Due to Impurities in the Crystal Structure of the Metal, and θ_D is the Debye Temperature.

Some metals lose their electric conductivity below a specific temperature called the critical temperature (T_c). Kamerlingh Onnes called these metals superconductors. As shown in Fig. 1.4, the impurities in a superconductor will mainly change the sharpness of transition from the normal state to the superconducting state. Magnetic impurities may cause the metal to have a lower T_c.

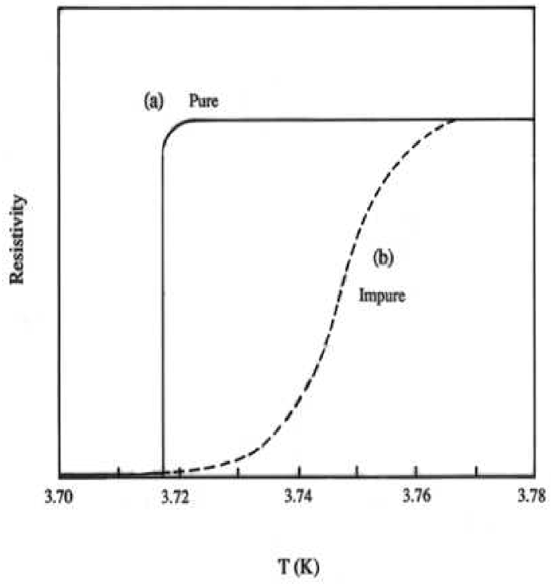

Figure 1.4: This Plot Shows the Sharpness of Superconducting Transition at T_c of a Pure Specimen (a) Versus Transition of an Impure Specimen (b).

According to the two-fluid model of superconductivity, there are two types of charge carriers in a superconductor: normal electrons and super-electrons. Using the Drude model of conductivity within metals, it is assumed that these two ”fluids” conduct electricity through a superconducting material. Normal electrons are scattered by ions in the crystal structure of the superconductor, similar to conduction electrons in a normal metal. As it is assumed in this model, super-electrons can move without scattering off ions or defects in the crystal structure. This has to do with the fact that the super-electrons (Cooper pairs) occupy the lowest energy state.

At the critical temperature and higher, all the conduction electrons consist of normal electrons. As we cool down the superconductor below its T_c, the ratio of super-electrons to normal electrons ($\frac{n_s}{n_n}$) gets larger, and eventually, at $T = 0$ all the conduction electrons become super-electrons. When a superconductor below its T_c experiences a D.C. bias, the super-electrons short the normal electrons, and therefore all the charge is carried by super-electrons.

We can model a superconducting wire as a parallel RL circuit, as shown in Fig. 1.5. The super-electrons short the circuit when the superconducting wire is connected to the D.C. power supply because they do not dissipate any power as opposed to normal electrons. However, if we A.C. bias a superconducting wire at a high enough frequency, we expect to see dissipation due to the scattering of normal electrons. At lower frequencies, most of the current will be carried by super-electrons. Therefore, the A.C. resistance won't be significant.

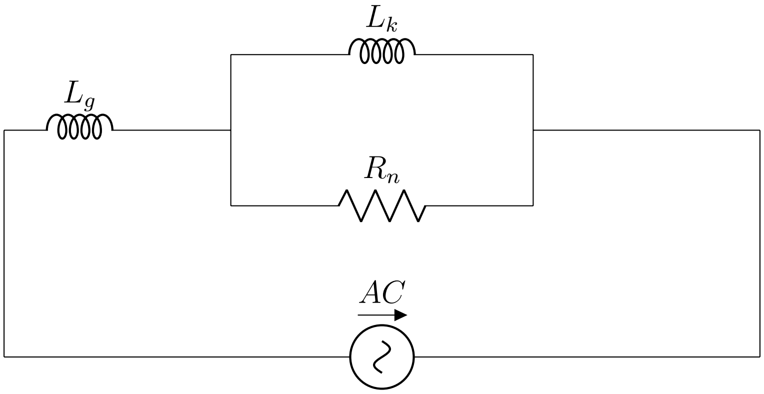

Figure 1.5: Circuit Diagram of a Superconducting Wire According to Two-Fluid Model. $\mathcal{L}_K$ is the Kinetic Inductance of Super-Electrons, and R_n is the Resistance Due to Scattering of Normal Electrons.

In 1933, Meissner and Ochsenfeld discovered that superconductors expel an applied magnetic field. This phenomenon happens independently of whether the superconducting specimen was initially cooled below its critical temperature and then put in the external magnetic field or if it was cooled while being inside an external field. When cooled inside an external magnetic field, a perfect conductor would not expel the external field from its interior (Fig. 1.6). However, the external magnetic field can only penetrate into the interior of the superconductor by a mount of λ_L called the London penetration depth. The external field dies out exponentially as a function of the penetration depth.

$$B(x) = B(0)\, e^{-x/\lambda_L} \tag{1.1}$$

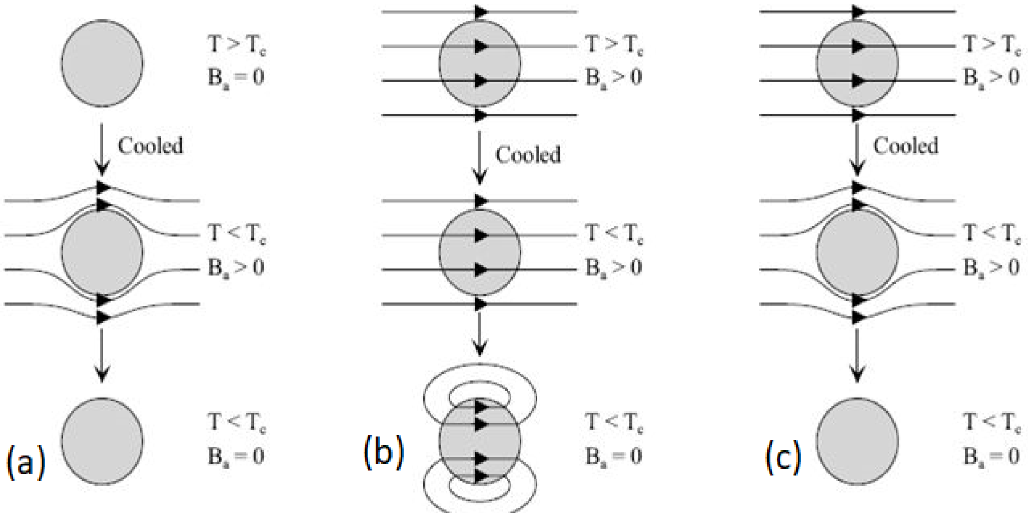

Figure 1.6: The Meissner-Ochsenfeld Effect. (a) Effect of Cooling and Applying a Magnetic Field to a Perfect Conductor and a Superconductor. (b) Effect of Applying a Magnetic Field and Then Cooling for a Perfect Conductor. (c) Effect of Applying a Magnetic Field and Cooling for a Superconductor Rose-Innes and Rhoderick (1994).

The Londons' equations as defined in Rose-Innes and Rhoderick (1994) are

$$\frac{\partial}{\partial t}\vec{J} = \frac{1}{\mu\lambda_L^2}\vec{E} \tag{1.2}$$

$$\boldsymbol{\nabla} \times \vec{J} = -\frac{1}{\lambda_L^2}\vec{H}, \tag{1.3}$$

where the following expression is the London penetration depth is given by λ_L:

$$\lambda_L^2 = \frac{m}{\mu_0 n_s e^2}, \tag{1.4}$$

In the above equation, n_s is the number density of the super-electrons and e is the elementary charge $e = 1.6 \times 10^{-19}\,\mathrm{C}$. Since the number density of super-electrons changes as a function of temperature, we can write the temperature-dependent London penetration depth as (Tinkham (2014))

$$\lambda_L(T) = \frac{\lambda_L(0)}{\sqrt{1 - \left(\frac{T}{T_c}\right)^4}} \tag{1.5}$$

where $\lambda_L(0)$ is given by Equation (1.6) and T_c is the critical temperature of the superconductor. For Al, $\lambda_L(0)$ is 50 nm and for Nb, it is 47 nm. In the London gauge where $\boldsymbol{\nabla} \cdot \vec{A} = 0$, we arrive at the following relation between the current density and the vector potential

$$\vec{J} = -\frac{1}{\lambda_L^2} \vec{A}, \tag{1.6}$$

which is a local relation between $\vec{J}$ and $\vec{A}$.

The application of a high enough magnetic field can destroy superconductivity. The magnitude of this field is called the critical magnetic field B_c. For a current-carrying superconducting wire with a thickness $t \gg \lambda_L$, this corresponds to a critical current I_c,

$$I_c = \frac{2\pi t}{\mu_0} B_c \tag{1.7}$$

where μ_0 is the permeability of free space.

Two other important length scales in superconducting materials are the mean free path l and the coherence length ξ. The mean free path is the distance over which electrons are scattered by impurities, and its momentum changes and therefore conservation of momentum can not be applied.

$$l = v_F \tau \tag{1.8}$$

where v_F is the Fermi velocity and τ is the relaxation time of the electrons. The coherence length is the distance over which the wave function of electrons stays coherent. When electrons are scattered by impurities and dislocation in the lattice structure, they undergo dephasing. Therefore, the coherence length can not be larger than the mean free path. The following equation shows the relationship between coherence length and the mean free path.

$$\frac{1}{\xi} = \frac{1}{\xi_0} + \frac{1}{l} \tag{1.9}$$

Where ξ_0 is the coherence length for a pure sample. As we can see from Equation (1.9) for a very pure sample $l \to \infty$, therefore $\xi = \xi_0$. If $l \ll \lambda_L$, then the field will not change significantly, and we can use a local approach to find a relationship between the current density and the applied field, as shown in the following section.

1.2.2 *Kinetic Inductivity*

If the $l \ll \lambda_L$, we can apply conservation of momentum to the charge carriers and derive the relationship between the current and the applied field in metals.

$$p(t + dt) \approx p(t) + \frac{dp}{dt}\delta t = p(t) + qE(t)\delta t \tag{1.10}$$

where $p(t)$ is the momentum, q is the charge and $E(t)$ is the time-varying electric field. Substituting the current density J instead of momentum p we get

$$\frac{m}{nq}\frac{\mathrm{d}\vec{J}}{\mathrm{d}t} = q\vec{E}(t) - \frac{m}{\tau}\frac{1}{nq}\vec{J}(t) \tag{1.11}$$

where m is the mass of the charge carriers, n is the number per volume of the carriers, and τ is the scattering time constant. With a bit of rearranging, we come down to the following equation.

$$\vec{J}(t) = \sigma(\omega)\vec{E}(t) \tag{1.12}$$

with

$$\sigma(\omega) = \sigma_n(\omega) - i\sigma'(\omega) = \frac{\sigma_{DC}}{1 + i\omega\tau} \tag{1.13}$$

where $\sigma_n(\omega)$ is the normal conductivity, $\sigma'(\omega)$ is the imaginary part of conductivity and $\sigma_{DC} = \frac{\tau n q^2}{m}$ is the DC conductivity. For normal metals $\omega\tau \ll 1$, therefore, $\sigma(\omega) \approx \sigma_{DC}$ and we reach the famous Ohm's law $\vec{J} = \sigma_{DC}\vec{E}$. For superconductors $\tau \to \infty$, however, since $\sigma_{DC} \to \infty$, the ratio of the two remains finite, and then we have

$$\sigma(\omega) \approx \frac{\sigma_{DC}}{i\omega\tau} = -i\frac{nq^2}{\omega m}. \tag{1.14}$$

Using the definition of susceptance, we find the kinetic inductivity for superconductors with $m = 2m_e$, $q = -2e$, and $n = n_e/2$ to be

$$\boxed{\mathcal{L}_k = \frac{m_e}{n_e e^2}.} \tag{1.15}$$

Thus, the kinetic inductivity, which can be thought of as the inductance due to the finite mass of the charge carriers, is proportional to the inverse of the number density of charge carriers. This property can be exploited to design sensors that track the kinetic inductance of a material as it changes due to the interaction of electromagnetic radiation with the charge carriers, such as in Microwave Kinetic Inductance Detectors (Day *et al.* (2003)).

If the vector potential associated with the applied field varies over a distance comparable to the coherence length, then we can not use the above approach, and we need to use a "non-local" relationship between the current density $\vec{J}(\vec{r})$ and the vector potential $\vec{A}(\vec{r})$, as proposed by Pippard in 1953 (Combescot (2022)). This can especially happen with high-quality superconductors at low temperatures where the mean free path becomes significant.

$$\vec{J}(\vec{r}) = -\frac{3}{4\pi\xi_0\mu_0}\frac{1}{\lambda_L^2}\int d\vec{r'}\frac{\vec{R}\Big(\vec{R}.\vec{A}(\vec{r'})\Big)}{R^4}\,e^{-\frac{R}{\xi}} \tag{1.16}$$

where $\vec{R} = \vec{r} - \vec{r'}$.

According to Bardeen-Cooper-Schrieffer (BCS) theory (Bardeen *et al.* (1957)), below T_c, electrons near the Fermi level form pairs of electrons (Cooper pairs) through a phonon-mediated interaction. The energy required to break apart Cooper pairs at $T = 0$ is $\Delta_0 = 1.7\,k_b\,T_c$, called the bandgap energy. Using the BCS theory, ξ_0 is given by

$$\xi_0 = \frac{\hbar v_F}{\pi\Delta}. \tag{1.17}$$

In the context of the BCS theory, the coherence length ξ_0 can be thought of as a lower bound on the size of a Cooper pair. Mattis and Bardeen used the BCS theory to derive a non-local relation between the current density and vector potential (Mattis and Bardeen (1958a)). Doing so, they arrived at the following equations for real and imaginary parts of the complex conductivity $\sigma(\omega) = \sigma_1(\omega) - i\sigma_2(\omega)$.

$$\frac{\sigma_1(\omega)}{\sigma_n} = \frac{2}{\hbar\omega}\int_{\Delta}^{\infty} dE\,\frac{E^2 + \Delta^2 + \hbar\omega E}{\sqrt{E^2 - \Delta^2}\sqrt{\left(E + \hbar\omega\right)^2 - \Delta^2}}\left[f(E) - f(E + \hbar\omega)\right] \tag{1.18}$$

and

$$\frac{\sigma_2(\omega)}{\sigma_n} = \frac{1}{\hbar\omega} \int_{\Delta}^{\Delta+\hbar\omega} dE \, \frac{E^2 + \Delta^2 - \hbar\omega E}{\sqrt{E^2 - \Delta^2}\sqrt{\Delta^2 - \left(E - \hbar\omega\right)^2}} \left[1 - 2f(E)\right] \tag{1.19}$$

where Δ is the gap energy as a function of temperature and $f(E)$ is the Fermi distribution function of the normal electrons.

At temperatures close to absolute zero, the Fermi function approaches zero; therefore, $\sigma_1(\omega)$ vanishes. However, $\sigma_2(\omega)$ remains finite and following Zmuidzinas (2012) we get

$$\frac{\sigma_2(\omega)}{\sigma_n} \approx \frac{\pi\Delta_0}{\hbar\omega}, \tag{1.20}$$

where Δ_0 is the superconducting bandgap in the absence of an applied field. Following the procedure in Kher (2017), we get the following expression for the surface kinetic inductance.

$$L_s = \frac{\hbar\rho_n}{\pi\Delta_0 t}, \tag{1.21}$$

in which ρ_n is the normal resistivity of the superconducting film and t is the thickness of the film.

1.2.3 Non-linear Kinetic Inductance

Ginzburg and Landau developed a phenomenological theory of superconductivity in 1950 (Tinkham (2015)) in which they introduced a macroscopic wave function ψ, also called the order parameter. The modulus square of the order parameter gives the number density of the Cooper pairs. They also showed that the difference between the free energy of the superconducting state and the normal state could be written as follows.

$$F - F_n = \alpha|\psi|^2 + \frac{\beta}{2}|\psi|^4 + \frac{B^2}{2\mu_0} + \frac{1}{2m}\Big|\Big(- i\hbar\nabla - 2e\vec{A}\psi\Big)\Big|^2, \tag{1.22}$$

where α and β are phenomenological parameters, A is the vector potential, and B is the magnetic field. Minimizing the free energy with respect to the order parameter for $T < T_c$, we arrive at the following solution for the density of Cooper pairs:

$$n_c = |\psi|^2 = \frac{\alpha}{\beta}\Big(1 - \frac{1}{2\alpha}mv_s^2\Big). \tag{1.23}$$

In the above equation, v_s is the velocity of Cooper pairs. With no magnetic field present and zero momentum, we can calculate the equilibrium value of the number density of charge carriers.

$$n_{eq} = |\psi_{eq}|^2 = -\frac{\alpha}{\beta} \tag{1.24}$$

Using the above equation, we can rewrite Equation (1.23) as

$$n_c = n_{eq}\Big(1 + \frac{1}{\alpha}m_e v_s^2\Big). \tag{1.25}$$

At the critical field B_c, superconductivity is destroyed, and the free energy is equal to the normal state free energy. From Equation (1.24), we can show

$$\alpha = -\frac{B_c^2}{\mu_0|\psi|^2}. \tag{1.26}$$

Also, the effective penetration depth in Ginzburg-Landau theory is given by (Kher (2017))

$$\lambda_{eff} = \sqrt{\frac{2m_e}{4\mu_0^2 e^2 |\psi|^2}} \tag{1.27}$$

The kinetic inductance can be calculated from Equation (1.15).

$$L_k = \mathcal{L}_k \frac{l}{A} = \frac{m_e}{n_c e^2} \frac{l}{A} \tag{1.28}$$

where l and A are the length and cross-sectional area of the wire, respectively. Combining Equations (1.25) and (1.28), we get

$$L_k = \frac{m_e}{e^2 n_{eq}} \frac{l}{A} \Big[1 + \frac{1}{\alpha} m_e v_s^2\Big]^{-1} \tag{1.29}$$

For small v_s, we can approximate the above equation as

$$L_k \approx \frac{m_e}{e^2 n_{eq}} \frac{l}{A} \Big[1 - \frac{1}{\alpha} m_e v_s^2\Big] \tag{1.30}$$

Let $\mathcal{L}_{k0} = \frac{m_e}{e^2 n_{eq}}$. Then

$$L_k = L_{k0} \Big[1 - \frac{1}{\alpha} m_e v_s^2\Big] \tag{1.31}$$

Combining Equations (1.26) and (1.31) and using

$$v_s^2 = \frac{J^2}{4 n_c^2 e^2}, \tag{1.32}$$

we can write the kinetic inductance in terms of current density J:

$$L_k = L_{k0} \left(1 + \frac{\mu_0 m_e}{4 e^2 B_c^2} J^2 \right) \tag{1.33}$$

The factor in front of the current density J sets the scale of nonlinearity and has the same units as the current density. Hence, we define a characteristic current density as follows.

$$J_* = \sqrt{\frac{4e^2 B_c^2}{\mu_0 m_e}} \tag{1.34}$$

Using $I = Jwt$, we can rewrite Equation (1.31) as

$$L_k = L_{k0}\left(1 + \frac{I^2}{I_*^2}\right) \tag{1.35}$$

Where I_* is the characteristic current.

Anthore *et al.* (2003), by conducting tunneling experiments and using Usadel equations for analysis (Usadel (1970)), showed that the bandgap suppression due to either an external magnetic field or a current follows the relation below.

$$\frac{\Delta}{\Delta_0} \approx 1 - 1.9\,\frac{J^2}{J_*^2} - 3.5\,\frac{J^4}{J_*^4} - ... \tag{1.36}$$

Combining Equations (1.21) and (1.36) and assuming $\frac{J}{J_*} \ll 1$, we get

$$L_k = L_{k0}\left[1 + 1.9\,\frac{J^2}{J_*^2} + 7\,\frac{J^4}{J_*^4} + ...\right]. \tag{1.37}$$

Using $I = Jwt$ and absorbing all the constants, we arrive at

$$L_k = L_{k0}\left(1 + \frac{I^2}{I_*^2} + \frac{I^4}{I_*'^4} + ...\right), \tag{1.38}$$

in which I_* and I_*' are the second and fourth-order nonlinearity scale factors, respectively.

The nonlinear kinetic inductance provides a nonlinear medium that allows for different mixing processes, such as three-wave and four-wave mixing, which can be taken advantage of to design parametric amplifiers, qubits, and other nonlinear superconducting devices. In the following chapters, we go over a few of these examples.

Chapter 2

MM-WAVE SUPERCONDUCTING CIRCUITS

2.1 Introduction

In this chapter, I go over the basic theory of millimeter-wave superconducting circuits, such as coupling circuits, diplexers, phase shifters, hybrids, etc. These circuits are the building blocks of on-chip integrated circuits and are essential for improving the performance of superconducting millimeter devices. In the last section, I explain the theory of operation of an On-Chip Superconducting Fourier Transform Spectrometer (SOFTS) complex circuit consisting of sub-circuits, including diplexers, probe antennas, quadrature hybrids, etc.

2.2 Superconducting Transmission Lines

The Telegrapher equation for a superconducting transmission line with a high-quality factor Q substrate can be written as follows

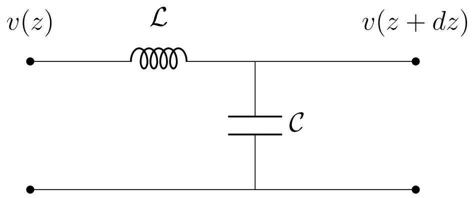

Figure 2.1: Lumped-Element Model of a Superconducting Transmission Line.

$$\frac{\partial^2 I}{\partial z^2} - \mathcal{L}\mathcal{C}\frac{\partial^2 I}{\partial t^2} = 0 \tag{2.1}$$

Following Pozar (2011), we arrive at the following solution

$$I(z) = \frac{V_0^+}{Z_0}\, e^{-i\omega\sqrt{\mathcal{L}\mathcal{C}}\, t} - \frac{V_0^-}{Z_0}\, e^{i\omega\sqrt{\mathcal{L}\mathcal{C}}\, t} \tag{2.2}$$

where Z_0 is the characteristic impedance, and for a transmission line with thick superconducting material and vacuum as a dielectric is given by

$$Z_0 = \sqrt{\frac{\mathcal{L}_g}{\mathcal{C}}} \tag{2.3}$$

where $\mathcal{L}_g$ is the geometric inductance per unit length and $\mathcal{C}$ is the capacitance per unit length. If we assume that the transmission line is made of a thin superconducting film with kinetic inductance per unit length of $\mathcal{L}_K$ and a dielectric layer with a dielectric constant of ϵ_r, then

$$Z_{TL} = \sqrt{\frac{\mathcal{L}_g}{\mathcal{C}}} \times \sqrt{\frac{1}{\epsilon_r(1-\alpha)}} = Z_0\sqrt{\frac{1}{\epsilon_r(1-\alpha)}} \tag{2.4}$$

where α is the kinetic inductance fraction and is given by

$$\alpha = \frac{\mathcal{L}_K}{\mathcal{L}_g + \mathcal{L}_K}. \tag{2.5}$$

The characteristic impedance of a propagating wave in free space is $Z_0 = 377$

ohms. The phase velocity can be calculated using

$$v_{ph} = \sqrt{\frac{1}{\mathcal{L}_g \mathcal{C}}}. \tag{2.6}$$

Following the same steps as above, we can write the phase velocity of a traveling wave on a transmission line with dielectric constant ϵ_r and kinetic inductance per unit length of $\mathcal{L}_K$ as

$$v_{ph}^{TL} = \sqrt{\frac{1}{\mathcal{L}_g \mathcal{C}}} \times \sqrt{\frac{1-\alpha}{\epsilon_r}} = v_{ph}\sqrt{\frac{1-\alpha}{\epsilon_r}} = c\sqrt{\frac{1-\alpha}{\epsilon_r}} \tag{2.7}$$

v_{ph} for a traveling wave in a vacuum is the speed of light c. However, by adjusting the kinetic inductance fraction α, we can change the phase velocity of light in the transmission line.

Now we can estimate the half-wavelength $\lambda/2$ and quarter-wavelength $\lambda/4$ values for a given transmission line resonator circuits using

$$f\,\lambda = v_{ph}^{TL} \tag{2.8}$$

as follows

$$l_{\lambda/2} = \frac{c}{2f}\sqrt{\frac{1-\alpha}{\epsilon_r}} \tag{2.9}$$

and

$$l_{\lambda/4} = \frac{c}{4f}\sqrt{\frac{1-\alpha}{\epsilon_r}}. \tag{2.10}$$

2.2.1 DC Biased Phase Shift

When a superconducting transmission line is biased with a constant current close to its characteristic current I_*, the kinetic inductance will become current-dependent, and the phase of the traveling wave as a function of DC becomes

$$\phi(I) \approx 2\pi f l \sqrt{\mathcal{C}\mathcal{L}_{K0}\left(1 + \frac{I^2}{I_*^2} + ...\right)} \tag{2.11}$$

Where $\mathcal{C}$ is the capacitance per unit length of the transmission line, and l is the length of the transmission line. The total phase shift due to a DC bias can be calculated as the difference between the phase shift with no DC bias (just from the length of the transmission line) and the phase shift caused by the constant current.

$$\Delta\phi(I) = 2\pi f l \sqrt{\mathcal{C}\mathcal{L}_{K0}}\left[\sqrt{\left(1 + \frac{I^2}{I_*^2} + ...\right)} - 1\right] \tag{2.12}$$

For a highly nonlinear transmission line $I_* \ll$ then $\frac{I^2}{I_*^2} \gg 1$ we can approximate the above equation

$$\Delta\phi(I) \approx 2\pi f l \sqrt{\mathcal{C}\mathcal{L}_{K0}}\left(\frac{I}{2I_*}\right) \tag{2.13}$$

And the total time delay can be calculated as follows.

$$\tau = \frac{\Delta\phi(I)}{2\pi f} = \frac{l'}{v_{ph}} = l\sqrt{\mathcal{C}\mathcal{L}_{K0}}\left(1 + \frac{I^2}{I_*^2} + ...\right)^{\frac{1}{2}} \tag{2.14}$$

Where l' is the effective length of the transmission line given by

$$l' = l\left(1 + \frac{I^2}{I_*^2} + ...\right)^{\frac{1}{2}} \tag{2.15}$$

2.3 Superconducting On-Chip Fourier Transform Spectrometer

2.3.1 Introduction

Interferometric techniques are widely used in astronomy for imaging and spectroscopy purposes Earle *et al.* (2006); Naylor *et al.* (2003); Fixsen *et al.* (1998); Greve *et al.* (2005); Aalto, S. *et al.* (2002); Bradford *et al.* (2004). The measured signal using an interferometer is in the conjugate space to focal plane imaging. Therefore, the signal from any one element of an imaging instrument is spread out among all the elements of the spectrometer Zmuidzinas (2003). For millimeter / sub-millimeter astronomy, imaging interferometers can be used for measurements of Cosmic Microwave Background (CMB) fluctuations, and spectral distortions Kouveliotou *et al.* (2014); Serra *et al.* (2016); Ghribi *et al.* (2009), line intensity mapping of spectral lines Visbal and Loeb (2010); Gong *et al.* (2013); Casey *et al.* (2014), and novel on-chip calibration technology for sub-millimeter focal planes. Some current experiments that use Fourier transform spectrometers are HERSCHEL Swinyard *et al.* (2014), SCUBA Naylor and Gom (2004), and OLIMPO Schillaci, Alessandro *et al.* (2014). The average size of such FTS instruments is one meter, with a frequency resolution ranging from 150 MHz to 6 GHz. Other experiments, such as DESHIMA Endo *et al.* (2012), and Superspec Wheeler *et al.* (2016), use on-chip filter bank technology with spectral resolutions of 200 -1000.

We show a superconducting on-chip Fourier transform spectrometer (SOFTS) with a Mach-Zehnder interferometer geometry. Taking advantage of materials with high normal resistivities such as NbN, NbTiN (Basu Thakur *et al.* (2022)) and the non-linear kinetic inductance property we can engineer ultra-compact and broadband spectrometers. The superconducting transmission lines behave like the optical arms of an FTS, however, with the advantage of not requiring any heavy or moving parts. I will go over the operating principles of the SOFTS device in the next section.

2.3.2 Device Physics

SOFTS is a four-port Mach-Zehnder interferometer, as shown in Fig. 2.2. The input signal is coupled to the device via an antenna and then split between two superconducting transmission lines (STL) using a superconducting quadrature hybrid (Pozar (2011)). The superconducting quadrature hybrid splits the signal's power in half, and phase shifts on half of the signal relative to the other half by $\pi/2$. After the signal passes through both STLs, it is recombined in another quadrature hybrid and read out using two detectors. The DC biasing is done through the low-pass port of a diplexer, with its high-pass port connected to the hybrid and the common port going to the STLs. Diplexers also prevent the current from DC bias from going through the hybrids. Another advantage of diplexers is that they allow us to explore low-frequency (audio band) biasing. We usually DC-bias one of the transmission lines to impose additional phase shift (delay) in one STL relative to the other STL. By scanning the DC bias in one arm, we can take a Fourier transform.

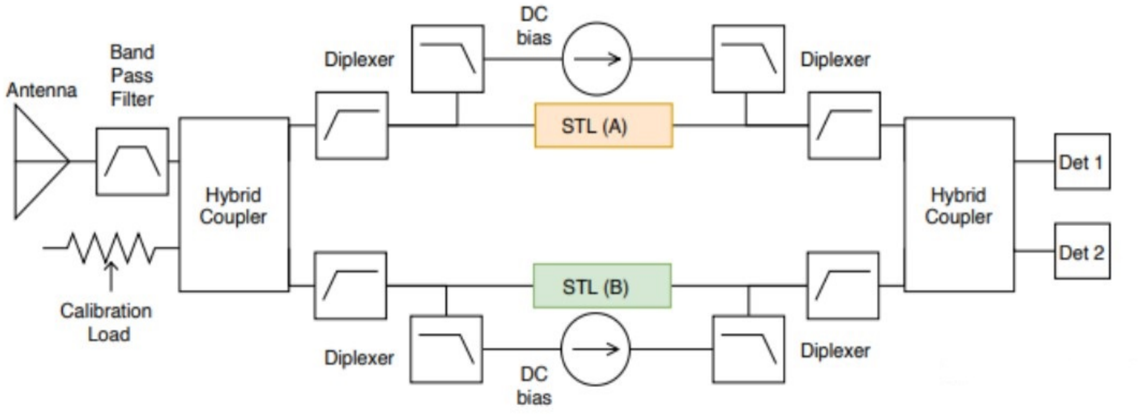

Figure 2.2: Circuit Diagram of the SFOTS Device. The Input Signal is Coupled to the Device Via an Antenna and Filtered Using a Band Pass-Filter. Then the Signal is Split Between Two Superconducting Transmission Lines (STL) Using a Superconducting Quadrature Hybrid. After the Signal Passes Through Both STLs, it is Recombined in Another Quadrature Hybrid and Read Out Using Two Detectors. The DC Biasing is Done Through the Low-Pass Port of a Diplexer, with its High-Pass Port Connected to the Hybrid and the Common Port Going to the STLs. Diplexers Also Prevent the Current from DC Bias from Going Through the Hybrids.

The current dependent time delay in one arm of the SOFTS can be expressed as follows (Basu Thakur *et al.* (2022))

$$\tau(I) \approx \frac{L_{\square} l}{Z_0 w}\left[\sqrt{\left(1+\frac{I^2}{I_*^2}+...\right)}-1\right] \tag{2.16}$$

Where $L_{\square}$ is the inductance per square, l is the length, Z_0 is the characteristic impedance, and w is the width of the STL. If we assume an incident field with power P_{inc} on the antenna and call the input port of the first hybrid 3, the power measured by the receiver will be

$$P_r = \frac{P_{inc}}{4}\left(|S_{13}+S_{23}|^2\right) \tag{2.17}$$

Where S_{13} and S_{23} are transmissions between the input port of the first hybrid (port 3) and the detectors 1 and 2. To calculate the total power detected at a detector

(P_Σ), we take the integral of power over all frequencies as follows

$$P_\Sigma(I) = \int_o^\infty \frac{P_0(f)}{2}\left[1 + C(f)\cos\left(2\pi f l\sqrt{\mathcal{C}\mathcal{L}_{K0}}\sqrt{\left(1+\frac{I^2}{I_*^2}+...\right)} - 1\right)\right]df \quad (2.18)$$

$P_0(f)$ is the power with no phase shift and $C(f)$ is the fringe contrast. If we parameterized current as $I = I(t)$ and chose a proper sweeping parameter, we can calculate the spectrum of the incident power $P_i(f)$

$$P_i(f) = 4P_0(f)\,\frac{|S_{13}|^2 + |S_{23}|^2}{C(f)}\int_0^\infty \Big(P_\Sigma(t) - P_\mu\Big)\cos\big(2\pi f t\big)\,dt \quad (2.19)$$

Where $P_\mu = \int_0^\infty P_0(f)df$. A more detailed and complete derivation of the power spectrum has been done by our collaboration in Klimovich (2022), and Basu Thakur *et al.* (2022).

The minimum frequency resolution of the SOFTS device is

$$\Delta f_{min} = \frac{1}{\tau_{max}} \quad (2.20)$$

τ_{max} is the maximum amount of time delay possible before reaching the critical current of the transmission line; thus, $\tau_{max} = \tau(I = I_{max} < I_c)$.

The resolution of the SOFTS device is given by

$$R = \frac{\lambda}{\Delta\lambda} = \frac{f}{\Delta f} \quad (2.21)$$

The maximum achievable resolution can be calculated by

$$R_{max} = \frac{f}{\Delta f_{min}} = f\tau_{max} \tag{2.22}$$

Therefore both the frequency resolution and the resolution of the SOFTS device will be determined by the critical current of the transmission lines.

Chapter 3

SIMULATION, DESIGN, AND FABRICATION

3.1 EM Simulation and Design

3.1.1 Radiation Coupling

Coupling mm-wave radiation to the superconducting microstrip lines requires a waveguide to microstrip transition by implementing a radial probe (Faramarzi *et al.* (2021)). In this configuration, the dominant mode of the rectangular waveguide, TE_{01}, is parallel to the plane of the probe, as shown in Fig. 3.1. To increase the coupling of the radiation to the probe, we add a waveguide size open cavity called a " backshort " that is a quarter-wavelength of the desired band and place it under the probe. This is due to choosing silicon as the substrate and its high refractive index of ~ 3.5. Other approaches, such as using Quartz, have also been explored by Kooi *et al.* (2003).

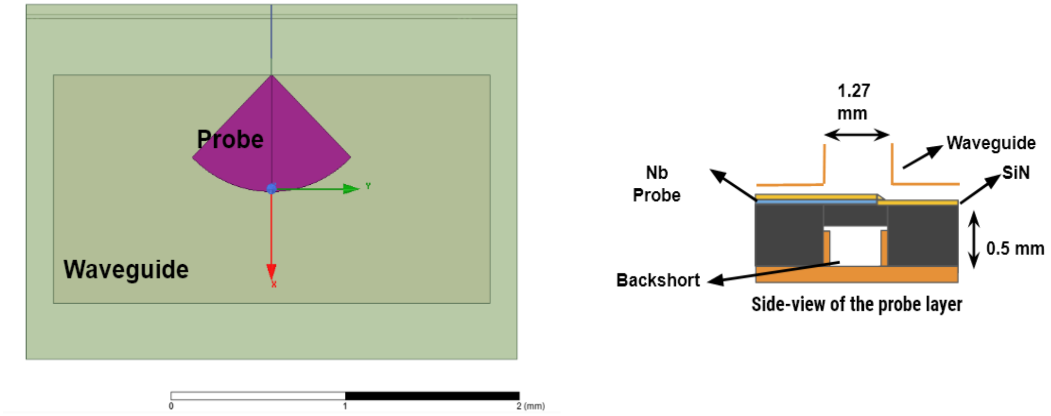

Figure 3.1: a) Shows a Top View of the Simulation Layout in HFSS Used for Optimizing Coupling Efficiency of the Radial Probes. b) Side View of the Chip Within the Housing of the Device. The Probes are Made of a Deposited Layer of NbN on a Silicon Substrate with a SiN Dielectric Layer on Top of the Probes. The Silicon on the Back Side of the Chip Where the Backshort is Positioned is Removed by a Deep Trench Etching Process to Maximize the Coupling Efficiency.

Optimization of the coupling efficiency of the probes was carried out using Ansys Electronics Suite high-frequency simulator (HFSS), a commercial electromagnetic simulator software. In these simulations, I included the surface inductance of the 20 nm thick NbN films used to fabricate the probes, plus the stepped structure of the silicon substrate. I also optimized the radius, angle, and backshort distance from the probe to maximize the coupling. As shown in Fig. 3.2, we expect to achieve a coupling efficiency of more than 80 percent across the full band.

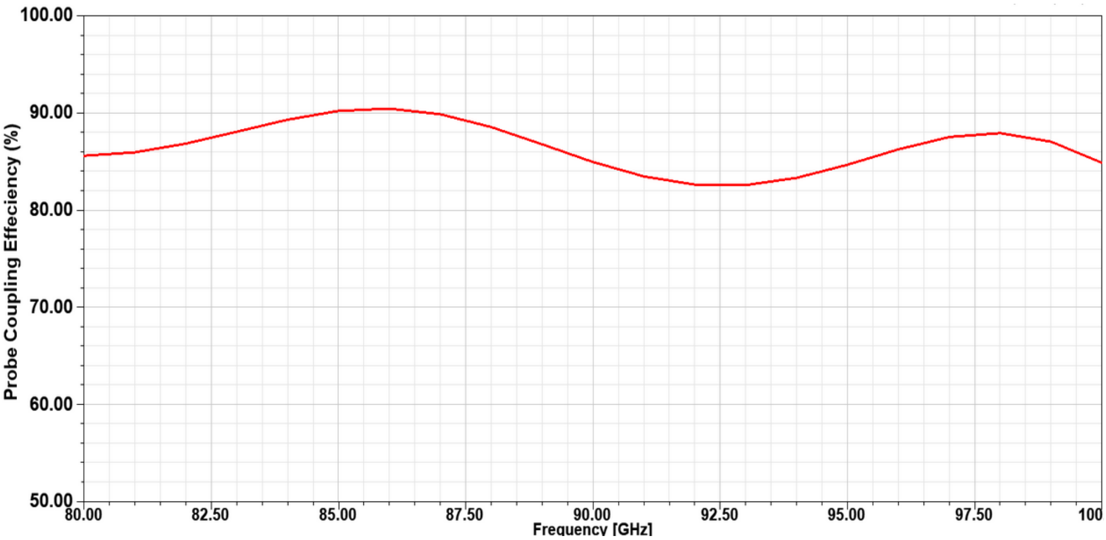

Figure 3.2: Optimized Coupling Efficiency of the Radial Probe to the Waveguide as a Function of Frequency.

3.1.2 Superconducting On-Chip Quadrature Hybrid Design

For dividing and combining the signal between the two arms of the interferometer (STLs), I designed a superconducting on-chip quadrature hybrid coupler. To avoid radiation loss into the silicon wafer, we have designed the device into a multi-layer inverted microstrip geometry (Fig. 3.3).

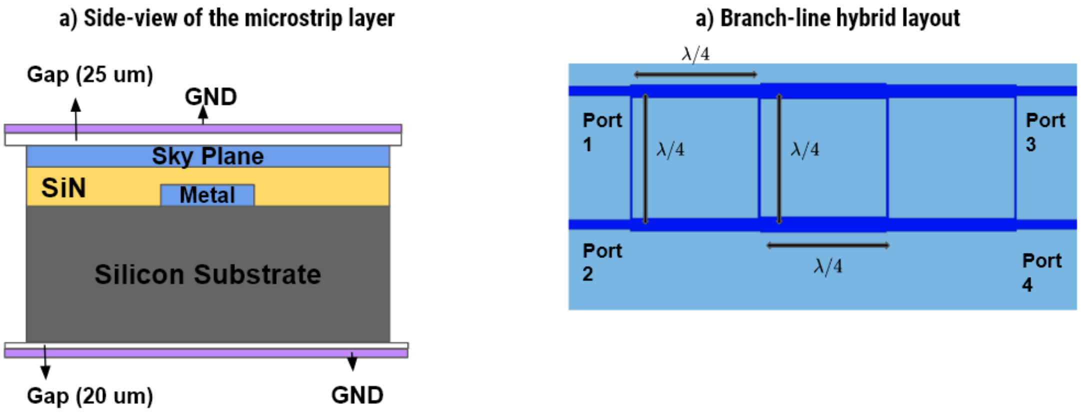

Figure 3.3: a) A Multi-Layer Microstrip Structure to Contain the Fields in the SiN Dielectric Medium. b) HFSS Simulation Layout of a Branch-Line Quadrature Hybrid with Three-Quarter Wavelength by Quarter Wavelength Branches.

This device is a branch-line hybrid Pozar (2011) with added branches to make it wider bandwidth for the frequency range of interest. As shown in Fig. 3.3, the length of each branch is a quarter wavelength of the center frequency. Using HFSS we optimized the impedance of each line to reject reflections and get 3 dB of power divided between the two output ports. Fig. 3.4 shows the optimized simulation results in HFSS. As we can see from the results, the designed hybrid almost covers the entire W-band region.

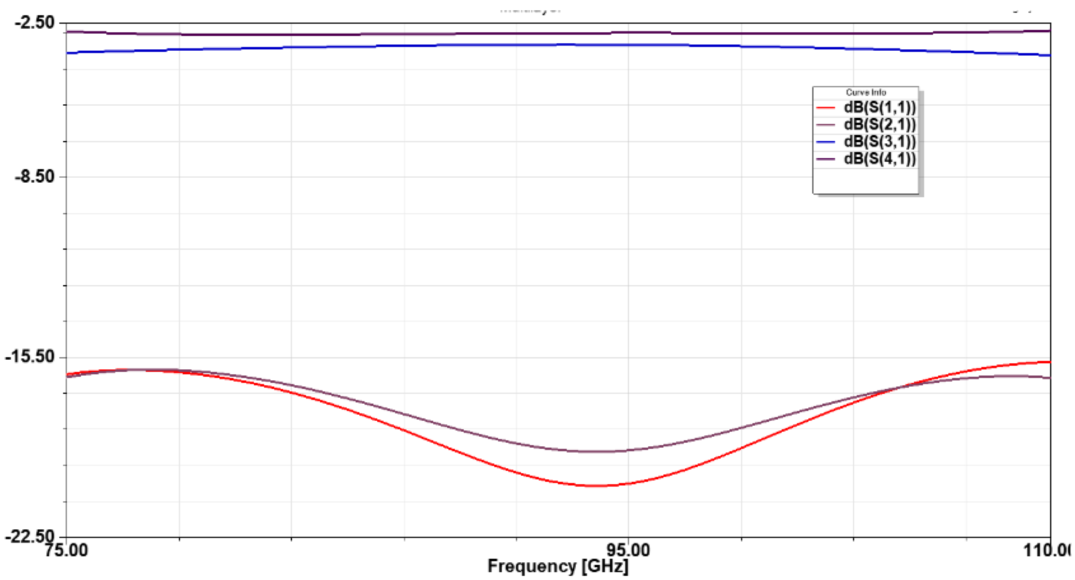

Figure 3.4: Simulated Scattering Parameters of the Quadrature Hybrid with Ports Corresponding to Fig.3.3.

3.1.3 Superconducting Transmission Line (STL) Design

The superconducting transmission lines have the same structure as the quadrature hybrid (Fig. 3.3). The microstrip transmission lines are made of a thin film of NbN. We DC bias the STLs to modulate their kinetic inductance and change the wave carrier's phase velocity. The length and width of the transmission line have been designed to meet the criteria mentioned in the previous chapter. The thickness of the STLs are 20 nm with the sheet inductance of $L_\square = 28$ pH/$\square$

3.1.4 SOFTS Split-Block Housing Design

The housing for the chip consists of three parts, with the top parts being the split-block waveguide as shown in Fig. 3.5, and a chip holder, which consists of the waveguide backshorts and acts as a heat sink for the SOFTS chip.

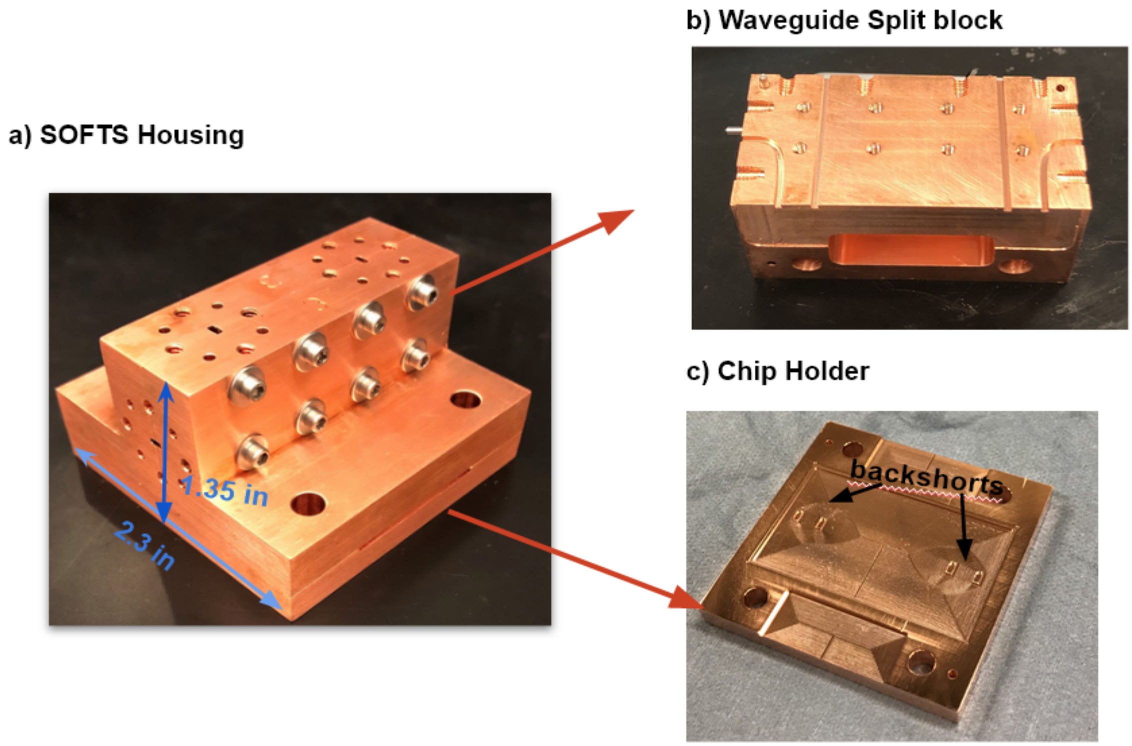

a) SOFTS Housing

b) Waveguide Split block

c) Chip Holder

Figure 3.5: a) Complete Housing Assembly of the SOFTS Chip. Four Waveguide Flange Fittings are on the Housing for Each Port of the SOFTS Device. Four Clearance Holes Mount the Top Part of the Housing to the Chip Holder and 4 Kelvin Stage of the Cryostat. b) This is Half of the Top Part of the Housing and Shows a Split-Block Waveguide from the Waveguide Sections to the Probes on the Chip. c) Chip Holder Design Consists of Backshorts for each Probe and Cutouts for DC Bias PCBs.

We have two extrude cuts on the chip holder to place printed circuit boards for DC biasing of the STLs.

3.2 Nano-Fabrication

In this section, we will describe the fabrication process of the SOFTS device in detail. Deposition of NbN thin films has been done as part of a collaboration at the Massachusetts Institute of Technology (MIT) by Marco Colangelo, a Ph.D. student in Karl Berggren's group. The rest of the processing, plus the deposition of niobium and SiN, has been carried out by myself and the help of a fellow graduate student, Sasha Sypkens, at the ASU Nanofabrication facility.

3.2.1 Wafer Cleaning

For this device, a 100 mm high resistivity ($\rho \gtrsim 2000\ \Omega$.cm) undoped silicon wafer with a thickness of $\sim$ 500 μm was chosen as the substrate. We start with cleaning the silicon wafer with a standard wafer cleaning procedure using piranha, RCA2, and HF. Piranha is a mixture of hydrogen peroxide and sulfuric acid that removes organic material. The wafer is submerged in piranha for 15 - 20 minutes and then rinsed with water. RCA-2 is a mixture of water, hydrogen peroxide, and hydrogen chloride that removes metal ions from the substrate. The wafer is then submerged in RCA-2 for 10 minutes and then rinsed with water. During the RCA-2 clean, the substrate develops a thin oxidation layer. To strip off the native oxide layer, an HF dip is used.

3.2.2 Deposition and Patterning

After cleaning the wafer, we put it in a sputtering chamber, pump it to 10^{-10} torr, and deposit 20 nm of NbN. After film deposition, we spin coat HMDS to help the photoresist adhere to NbN. The HMDS is then baked on a heater at 100°C for one minute, then 1 μm of AZ 3312 positive photoresist was deposited and baked at 100°C for one minute. Using a 1:1 photolithography method, we pattern the surface of the photoresist by projecting ultraviolet light through a mask. We carried out a post-exposure bake of the wafer at 110°C for one minute and then developed the photoresist by submerging it in AZ MIF 300 developer for about a minute. This step dissolves the exposed parts of the photoresist to UV light and will leave the desired pattern on the photoresist layer. After rinsing the wafer with water and blow drying it with nitrogen gas, it was baked at 110°C for 3 minutes to harden the photoresist. We then etch away the NbN layer not covered by the photoresist using a Reactive Ion Etcher (RIE) in a CF_4 chemistry. Fig. 3.6 shows the NbN antenna probes after the etch process.

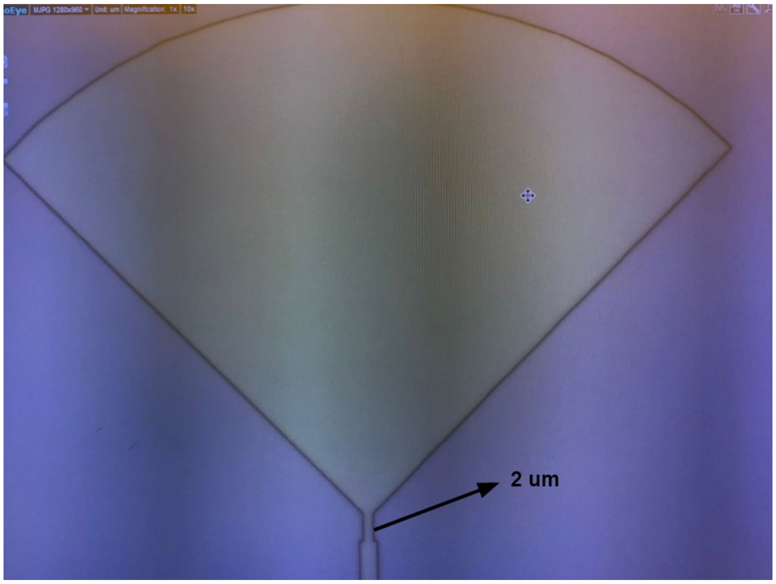

Figure 3.6: NbN Probe Antenna After the Etch Process.

After the etch process, the photoresist is removed by acetone and isopropyl alcohol and blow-dried by pressurized nitrogen. The fluorine in CF4 reacts with the photoresist, leaving a dark smudge on top of the features. To clean these residues, we ash the wafer in an oxygen atmosphere. After cleaning the wafer, we deposit 545 nm of SiN using a Plasma-Enhanced Chemical Vapor Deposition (PECVD) technique and pattern the SiN layer to remove it from the bond pads. The figure below shows the quadrature hybrid after the SiN deposition.

Figure 3.7: The Quadrature Hybrid Coupler After NbN Etch, and SiN Deposition.

3.2.3 Niobium Lift-off Process

The next step is the deposition and pattering of the Nb skyplane. For this, we use a lift-off process developed by myself and the help of the ASU Nanofab facility engineers Carrie Sinclair and Kevin Nordquist. For this process, we use a bilayer photoresist method as shown in Fig. 3.8

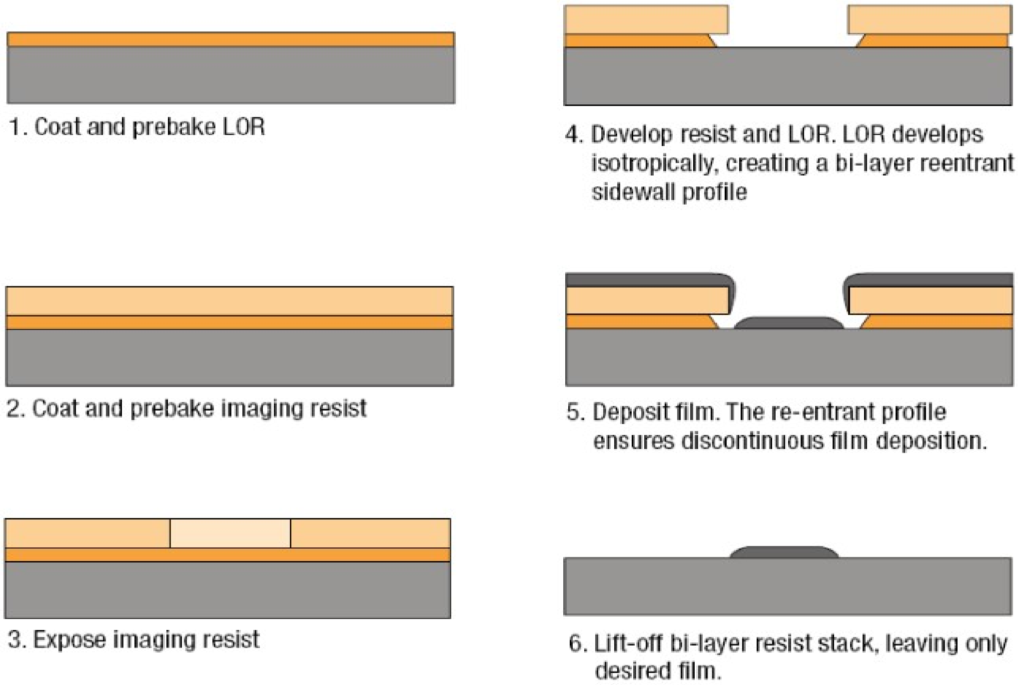
1. Coat and prebake LOR

2. Coat and prebake imaging resist

3. Expose imaging resist

4. Develop resist and LOR. LOR develops isotropically, creating a bi-layer reentrant sidewall profile

5. Deposit film. The re-entrant profile ensures discontinuous film deposition.

6. Lift-off bi-layer resist stack, leaving only desired film.

Figure 3.8: 1) Spin Coating and Pre-Bake of the LOR Photoresist. 2) Spin Coating and Pre-Bake of the Imaging Photoresist. 3) Exposure of the Imaging Photoresist. 4) Development of Photoresists. 5) Film Deposition. 6) Lift-off Step.

We start with spin coating LOR 10A photoresist at a rate of 5000 RPM for 30 seconds and then soft bake it at 180°C for 2 minutes. After the wafer cools to room temperature, we spin coat 1μm of AZ 3312 on top of the LOR 10A resist. We then expose the photoresist to define the patterns and develop them in AZ MIF-300 for 55 seconds. After both photoresists are developed, we should see a bi-layer re-entrant profile that ensures a discontinuous film deposition.

The next step is depositing Nb on the wafer, which is done by a sputtering method. After the deposition, we lift off the Nb deposited on the photoresist by dipping the wafer in a AZ 400T photoresist stripper for 40 minutes. When the unwanted Nb layer is completely stripped, we rinse the wafer with water and blow dry it with nitrogen gas.

3.2.4 Silicon Blind Etch

After the front processing is done, we need to pattern and etch the back of the wafer for optical enhancement. This requires us to protect the front of the wafer with a thick photoresist layer. We coat 4μm of AZ 4330 and soft bake it using a heater and bake it at 105°C for 2 minutes. Now we can process the back of the wafer by coating about 11μm of AZ4620 photoresist and setting the heater to proximity mode to ensure the front side photoresist would not stick to the heat plate. Now we can expose the photoresist using contact lithography. To align the features on the back with the patterns on the front, we use the backside alignment capability of the EVG photolithography system. After we are done with the exposure step, we develop the photoresist and hard bake it at 113° C in proximity mode for 33 minutes. Now, we can etch the silicon using a Deep Reactive Ion Etcher with the Bosch process (Fig.3.10).

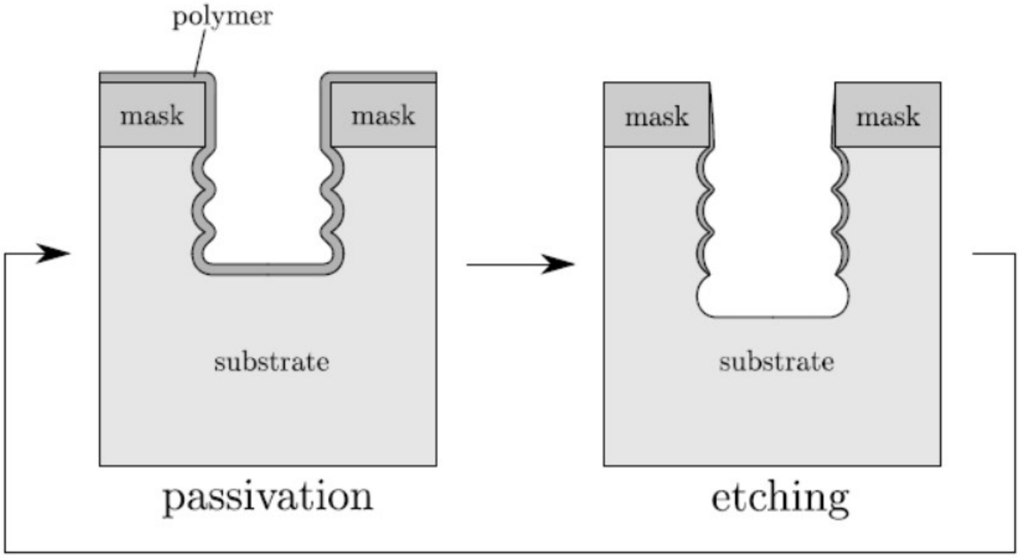

Figure 3.9: The Bosch Process Consists of an Etching Step and a Passivation step, as Shown Here. (from :www.iue.tuwien.ac.at/phd/ertl/node68.html)

The Bosch process consists of the following steps:

1. Etching of the bottom passivation film using sulfur hexafluoride SF_6.
2. Deposition of a passivation film on the side walls and the bottom of the trench using Octafluorocyclobutane C_4F_8.

Before putting the wafer in the DRIE tool, we put blue tape on the front side of the wafer to protect the wafer from cracking and falling into the tool. We usually start with 100 to 150 cycles and then measure the thickness of the photoresist and the trench height to determine the etch rate. The recipe we use yields an etch rate of $1\,\mu$m/cycle on average for silicon and $0.1\,\mu$m/cycle for the AZ4620 photoresist. We continue the etch process and measure the depth of the trench every 50 to 100 cycles until we reach the desired thickness underneath the probes. Table 3.1 shows some of the etch parameters.

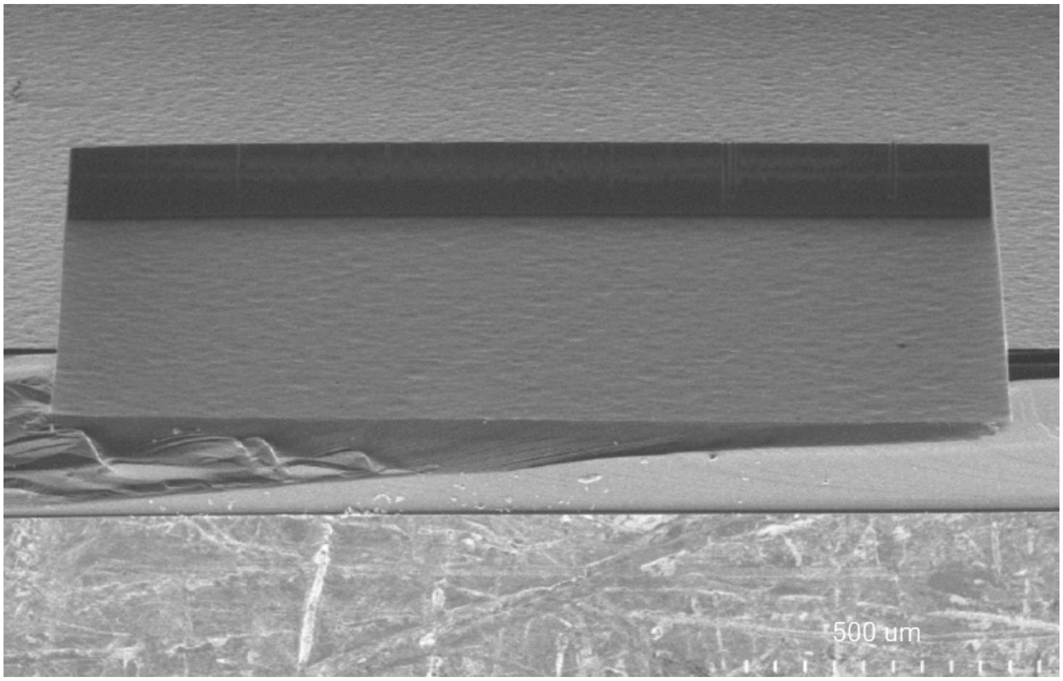

Figure 3.10: SEM Micrograph of the Silicon Blind Etch Taken by ASU NanoFab Engineer Dr. Scott Ageno.

PR Etch Rate (μm/cycle)	Si Etch Rate (μm/cycle)	Selectivity (%)
0.13	1.186	91.23

Table 3.1: The Etch Parameters for DRIE of Silicon Using the Bosch Process.

After the etch is done, we ash the wafer in an oxygen atmosphere for 20 minutes to help strip the photoresist off the wafer. We then submerge the wafer in AZ 400T at 80°C until the photoresist and the blue tape are completely stripped. In the end, we gently rinse the wafer with water.

Chapter 4

MEASUREMENTS AND RESULTS

4.1 Introduction

In this chapter, I will review the cryogenic testbed designed at ASU for low-temperature measurements. The cryostat is a closed cycle Sumitomo 4 K Gifford-McMahon cryocooler, and it can reach slightly lower than 3 K in roughly one and a half hours with no thermal load. I also present the measurements done at ~ 4 Kelvin at ASU to test some non-linear properties of the devices designed and fabricated, as mentioned in the previous chapter, including the SOFTS device measurements.

4.2 4K Cryogenic Testbed

The 4K test bed used to measure mm-wave devices at ASU was designed and assembled by Hamdi Mani, Sasha Sypkens, and myself. We used a refurbished RDK20 Gifford-McMahon cryocooler to get to 4 Kelvin. A hollow aluminum cylinder was designed as a shell to engulf the cryocooler and was mounted to the room temperature mounting flange of the cryocooler and vacuum sealed using proper o-ring (Fig4.1). An 8-inch × 8-inch aluminum enclosure was designed and mounted to the cylinder with an o-ring in between to help vacuum seal the entire 300 K shell. The top of the square enclosure has an o-ring groove to place an o-ring and vacuum seal the top using a square aluminum lid. There are round holes on either side of the enclosure and two larger rectangular holes on the other side for access to the interior of the testbed.

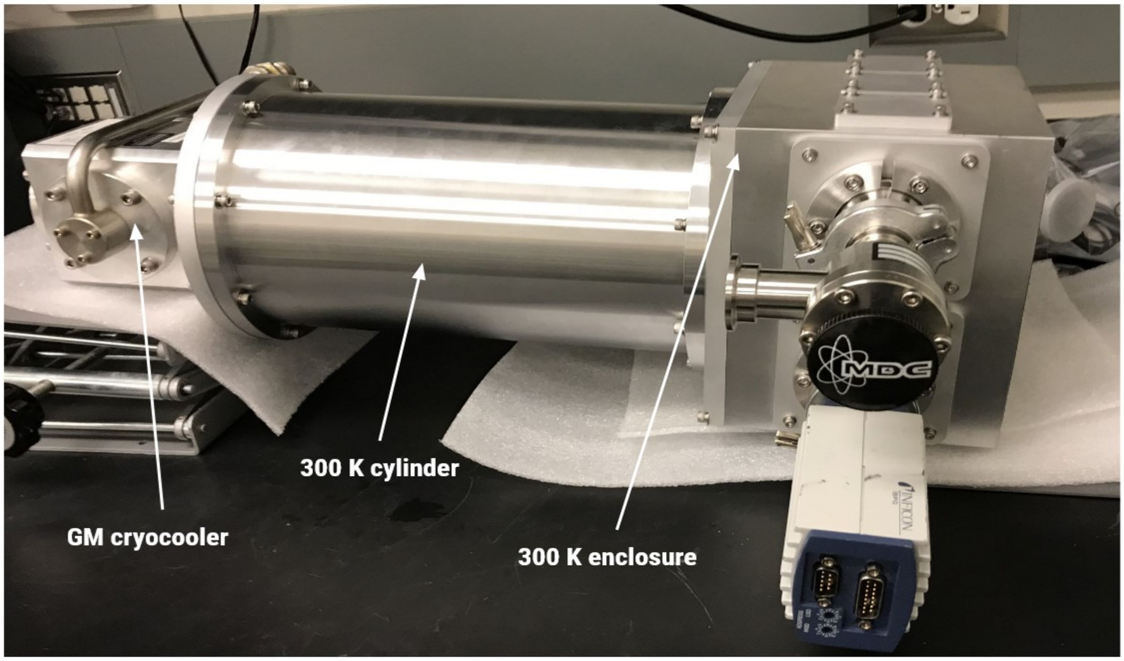

Figure 4.1: The Room Temperature Shell is Fully Assembled and Mounted to the Room Temperature Flange of the Cryocooler.

The unused access points are sealed using rectangular caps. We use hermetically sealed SMA connectors on the enclosure caps to conduct microwave frequency measurements inside the testbed. For DC measurements, we use BNC connectors on the 300 K side, which lead to 10 kHz low pass filters for each center conducting line before going into the cryostat. On the cold side, a quad-twist cryo wire from Lakeshore is used.

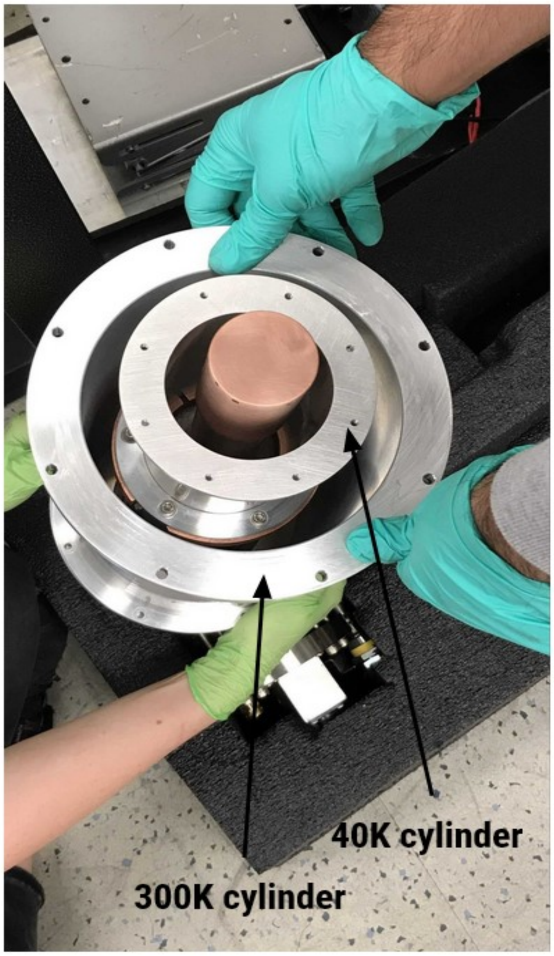

Figure 4.2: 300 K and 40 K Aluminum Cylinder Shields.

A smaller aluminum cylinder was designed, machined, and mounted to the first stage (40 K) of the cryocooler. On top of that, four aluminum plates were mounted to the cylinder to form a box to isolate the second stage from radiation emitted from the room-temperature shell.

A 6-inch × 6-inch gold-plated copper plate was designed and mounted to the second stage of the cryocooler. We also made a 0.5-inch × 0.5-inch hole pattern and used press-in nuts to mount devices to the 4K plate.

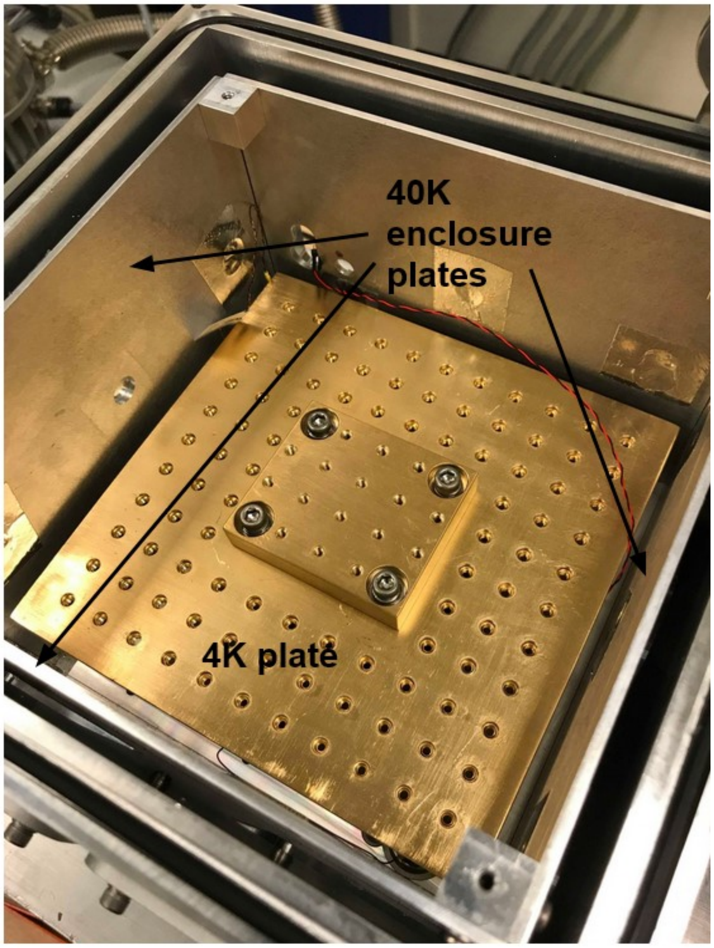

Figure 4.3: Picture of the Inside of the Cryostat Showing the Gold-Plated Copper Plate with Half an Inch Hole Spacing and 40 K Shields.

To mount the 4 K plate to the cold head, we used 2” × 2” × 0.25” gold-plated copper piece to clamp the 4 K plate to the cold head.

4.3 Test Features and Measurements

Some test features designed for DC and low-frequency measurements were a DC-biased half-wave resonator and a $\sim 10\,\mu$m NbN wire. The half-wave resonator was designed to measure the frequency response of the NbN film, and the NbN wire was made for T_c and I_c measurements. Fig. 4.4 shows the resistance vs. temperature plot of the wire. As we can see from this plot, the critical temperature of the NbN film appears to be around 5 K. The test features are located close to the edge of the wafer. Due to the lack of uniformity across the 4-inch wafer, we suspect the lower critical temperature is due to a thinner NbN layer closer to the edges of the wafer. A 20 nm thick layer of NbN was deposited across the wafer, and we expect a T_c of 8 K.

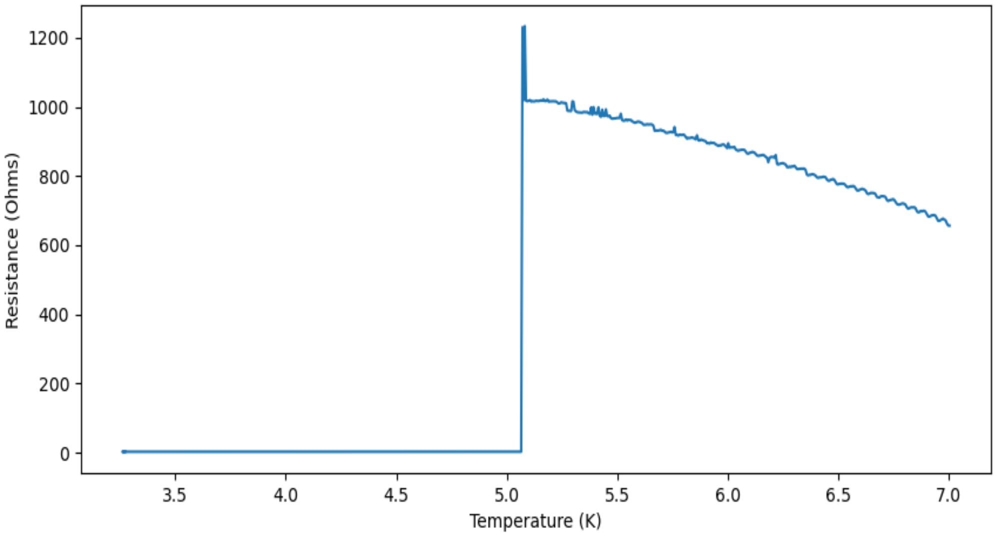

Figure 4.4: The Resistance vs. Temperature of the NbN Wire.

We also measured the critical current of the test structure by applying a DC bias to the NbN line and measuring the voltage drop across the NbN wire. The circuit diagram of the measurement setup is shown in Fig. 4.5. We used a 1kΩ resistor to current-bias the device under test (DUT), and the amount of current was adjusted by changing the output of the DC power supply.

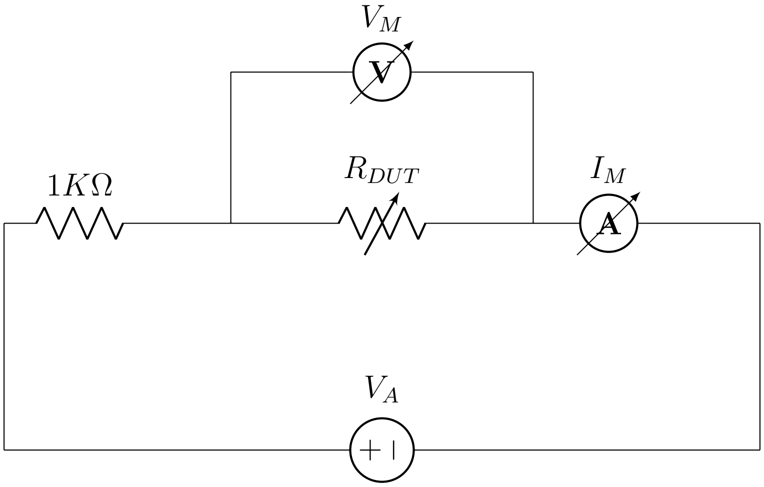

Figure 4.5: Circuit Diagram of a Measurement Test Setup of the Critical Current. R_{DUT} is the Resistance of the Device Under Test, V_M is the Measured Voltage Across the DUT. I_M is the Measured Current Through the DUT, and V_A is the Applied Voltage.

The plot of measured voltage V_M across the DUT as a function of the applied voltage V_A is shown in Fig. 4.6. As we expect, there is a discontinuity in the voltage measured across the DUT due to an abrupt resistance change when NbN transitions from the superconducting state to the normal state above its critical current.

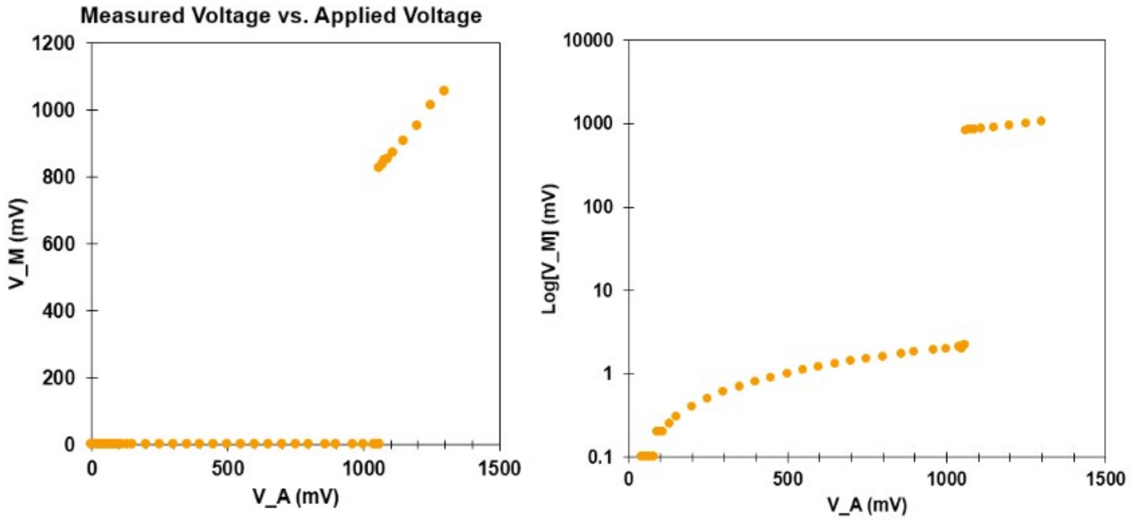

Figure 4.6: *left* Plot of Measured Voltage Across the 10-Micron Wire vs. the Applied Voltage to the Wire. *right* Semi-log Plot of the Plot to the Right.

Fig.4.7 shows the plotted voltage versus current of the wire for low applied currents. As we can see, there is an ohmic relationship between the voltage and current past the superconducting regime. By fitting the data to Ohm's law, we extract a value of 2.3 Ω, close to the value expected for the series resistance from the wires in the measurement setup.

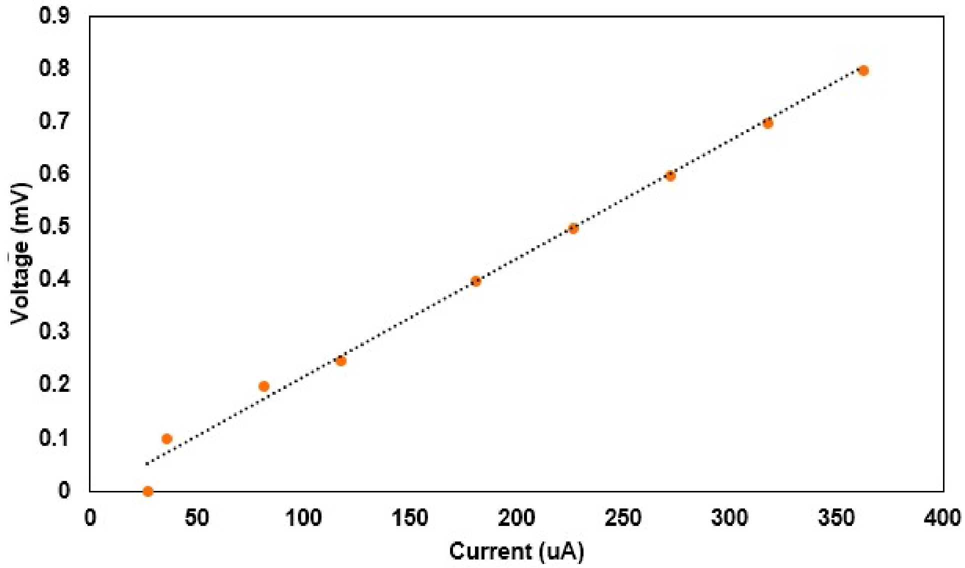

Figure 4.7: Plot of Voltage Across the Wire vs. the Measured Current Through the Wire for Low Currents at 3.5 K.

Subtracting the residual resistance due to cables and test fixtures, we can now plot the resistance of the DUT. The abrupt change in the resistance of the wire happens around 0.9 mA, which is assumed to be the critical current of the wire. The normal resistance of the superconducting wire is around 4.8 kΩ as shown in Fig. 4.8.

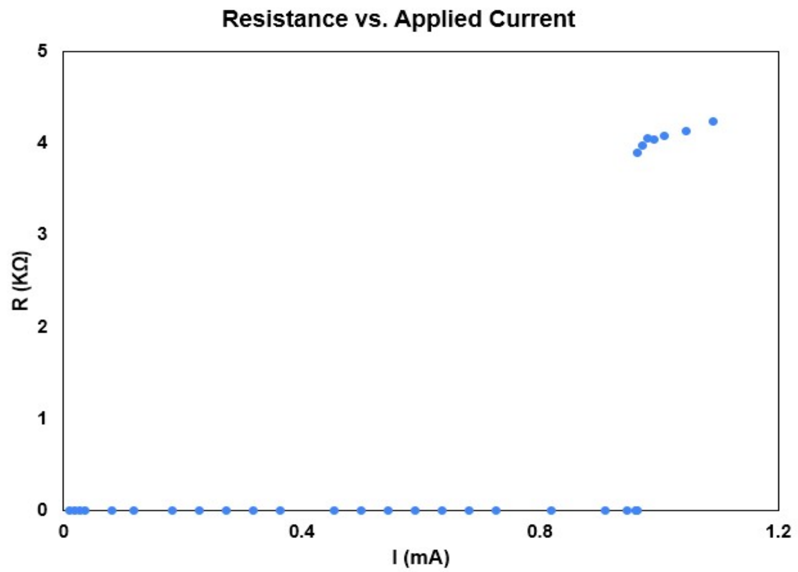

Figure 4.8: Plot of Resistance of the Superconducting Wire as a Function of the Applied Current.

The next test feature is a 10 μm wide half-wave coplanar waveguide (CPW) resonator on the same wafer as shown in Fig.4.9. The resonator was designed to measure the shift in resonant frequency as a function of DC bias. Bias wires go directly to the half-wave resonator transmission line for DC biasing.

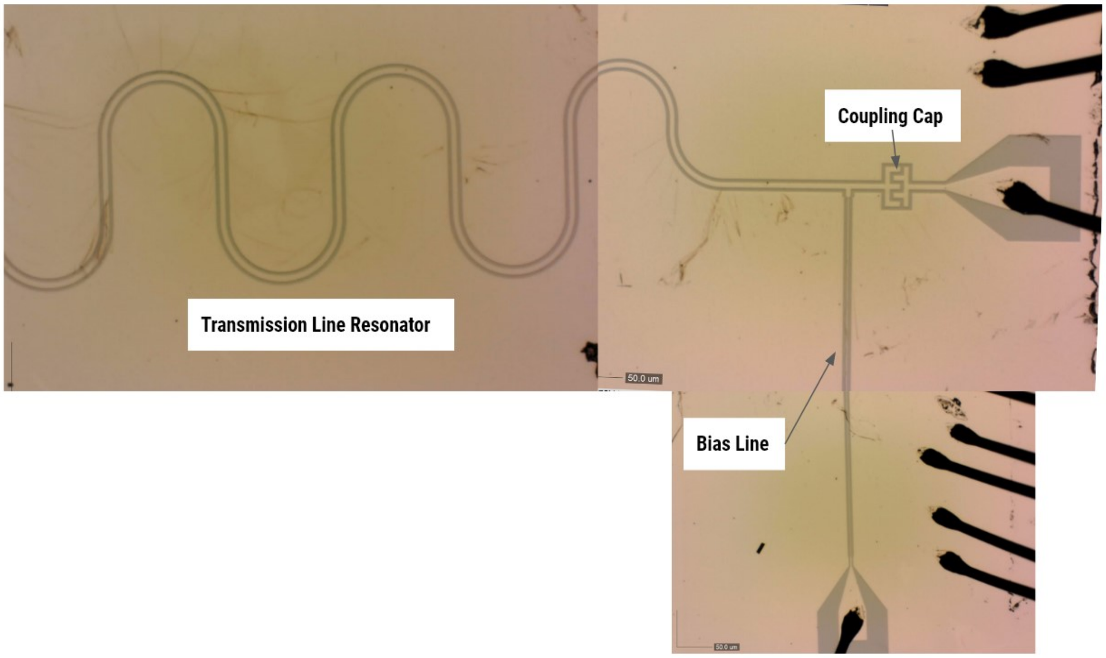

Figure 4.9: Optical picture of the NbN Half-Wavelength CPW Resonator Patterned on 500 μm of Silicon. The Dark Lines on the Right Edge of the Picture are the Wirbonds Connecting the Chip to a PCB.

The response of the resonator was measured using a VNA as a function of applied current. The test setup for this measurement is drawn in Fig. 4.10. We used a combination of copper and stainless steel SMA cables from 300 K to the 4 K stage. The stainless steel cables were used to reduce the heat load on the 4K stages. A 5 dB attenuator was used between the 300 K and 40 K stages. An inner-outer DC block was used at the 40 K input and output stages to reduce heat load and low-frequency noise further. A 20 dB attenuator was placed on the 4 K plate before the resonator. We then used a cryogenic low-noise amplifier (LNA) to read out the resonator. A twisted pair of wires biased the resonators.

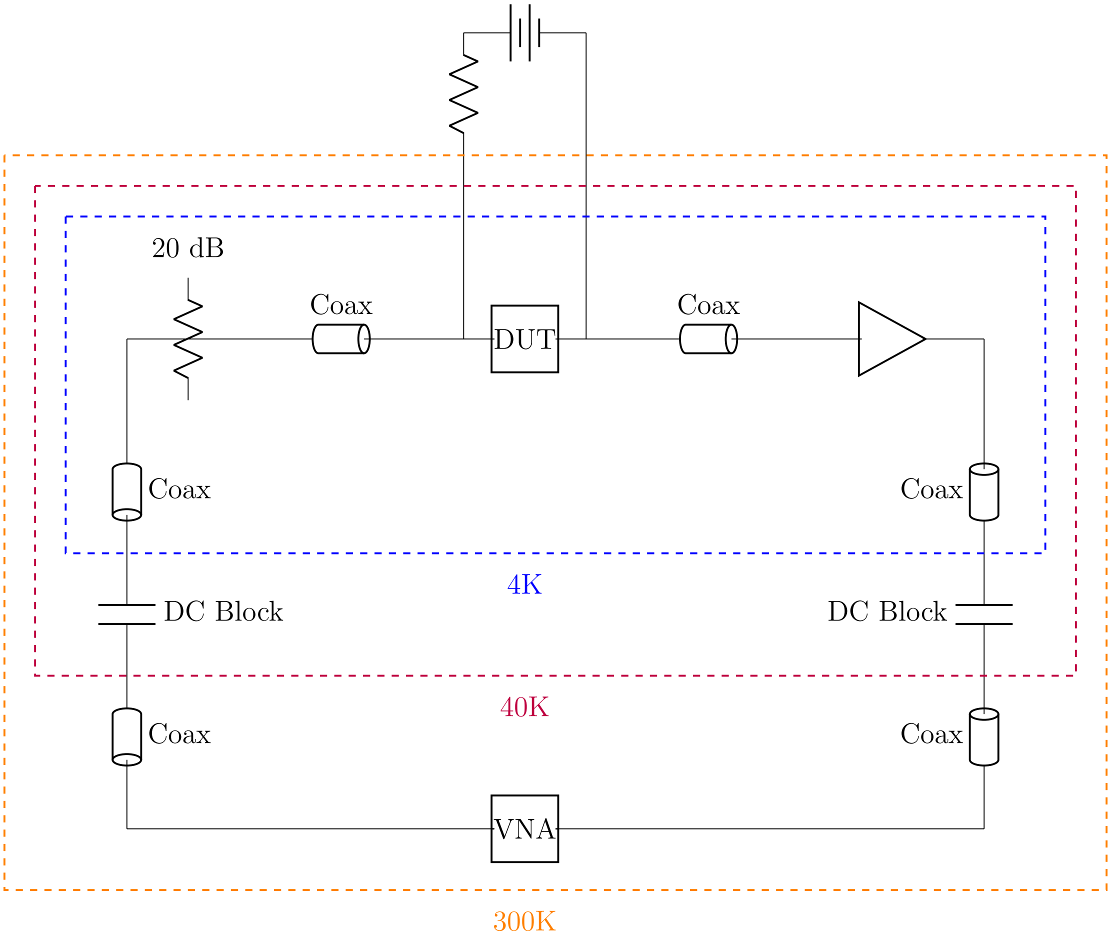

Figure 4.10: Circuit Diagram of the Measurement Test Setup Used for Resonator Measurements. An Inner-outer DC Block was Used at the 40 K Input and Output Stages to Reduce Heat Load and Low-Frequency Noise Further. A 20 dB Attenuator was Placed on the 4 K Plate Before the Resonator. We Then Used a Cryogenic LNA to Read out the Resonator. A Twisted Pair of Wires Biased the Resonators.

Proper EMI filtering was done using a combination of room temperature and cryogenic low-pass filters. The current bias was set using a 1 kΩ resistor and a power supply by adjusting the voltage. The resonator's response was measured using a Network Vector Analyzer (VNA) after applying different current biases. We particularly looked at the S_{21} element of the S-matrix of a two-port network (Pozar (2011)) defined as follows

$$\begin{pmatrix} V_1^- \\ V_2^- \end{pmatrix} = \begin{pmatrix} S_{11} & S_{12} \\ S_{21} & S_{22} \end{pmatrix} \quad \begin{pmatrix} V_1^+ \\ V_2^+ \end{pmatrix}$$

V_1^- and V_2^- are the scattering waveform voltages from ports one and two. V_1^+ and V_2^+ are the incident waveform voltages. The S_{21} parameter is therefore given by

$$S_{21} = \frac{V_2^-}{V_1^+}. \tag{4.1}$$

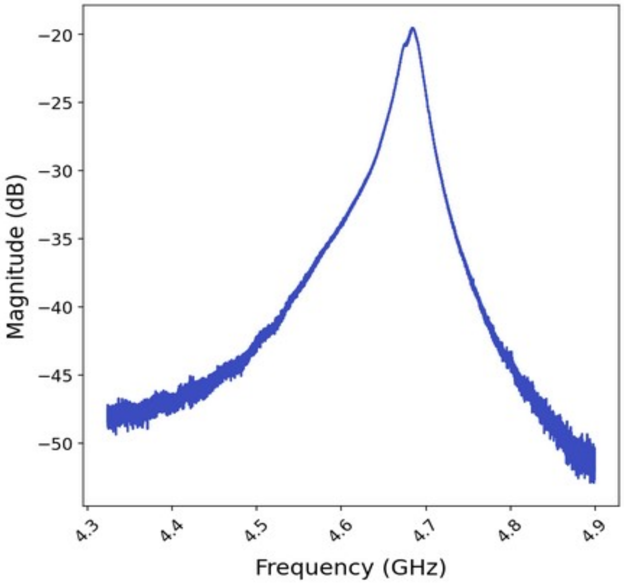

Figure 4.11: Plot of S_{21} of the Half-Wave Co-Planar Waveguide (CPW) NbN Resonator with no Current Bias. On Resonance we Expect Maximum Transmission from Port-1 to Port-2 Because the Impedance of the Resonator Goes to Zero.

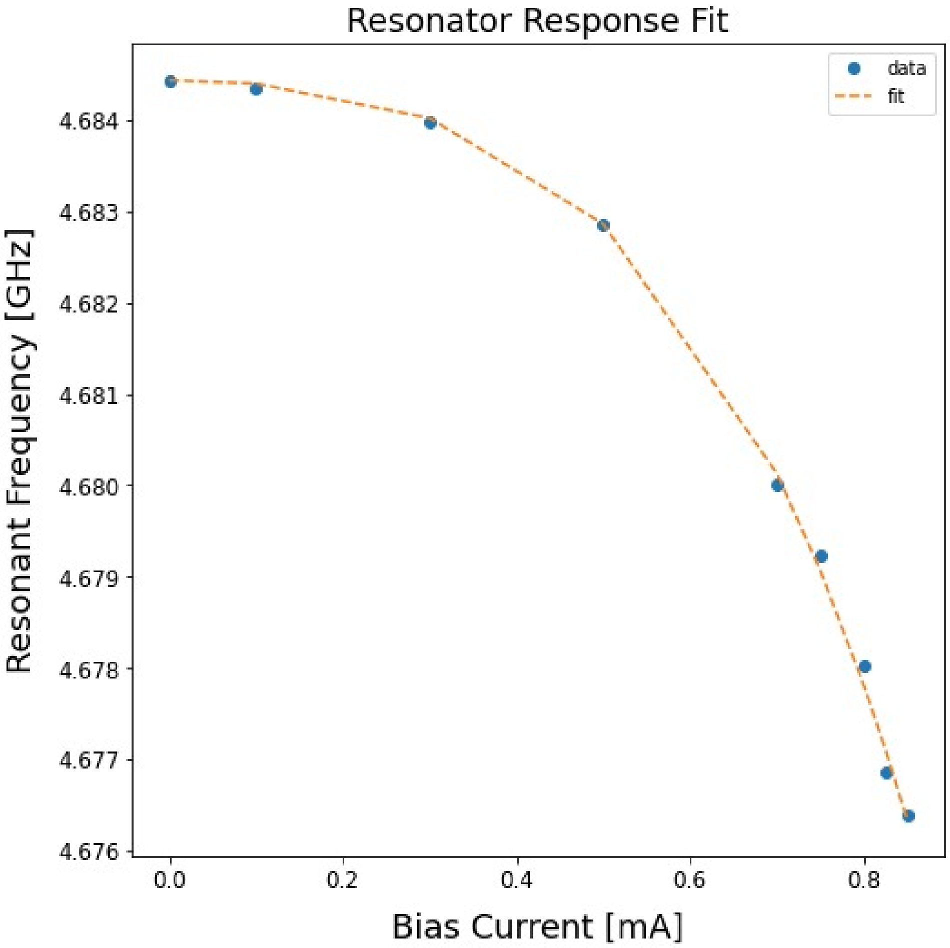

Figure 4.12: Plot of the Shift in Resonance Frequency vs. the Applied Current to the Resonator.

The resonant frequency of the resonator depends on the bias current as follows.

$$f_r(I) = f_r(0)\left[1 + \left(\frac{I^2}{I_*^2}\right) + \left(\frac{I^4}{I_{**}^4}\right)\right]^{-\frac{1}{2}} \tag{4.2}$$

where $f_r(I)$ is the current dependent resonant frequency of the CPW resonator, $f_r(0)$ is the resonant frequency with no current bias $I = 0$, I_* is the second-order characteristic current, and I_{**} is the fourth-order characteristic current. Using Eq. (4.1) and fitting it to the measured data, we can extract the value of the characteristic current I_*, which is about ~ 25 mA. This only corresponds to a four percent change in the fractional kinetic inductance for this resonator at the critical current. Fig. 4.12 shows the plot of the measured resonant frequency as a function of bias current with the best fit.

4.4 W-band Test Setup

The test setup to measure the W-band FTS requires a VNA with extenders to get to the required frequency and waveguide feed-throughs from the VNA extenders at 300K to the 4K stage of the cryostat, which holds the split-block housing and device. When designing the waveguide feed-throughs, thermal contraction due to a steep gradient in temperature was considered. We use mica windows and bulkhead waveguide flanges to ensure no vacuum leak.

For SOFTS measurements, we used a 2.6-inch stainless steel straight waveguide section placed between the waveguide bulkhead flanges and the 40K stage, followed by a half an inch standard gold-plated copper section, a 20 dB attenuator, and the split-block waveguide housing. We used a combination of copper and stainless steel waveguides from the waveguide housing on the 4K plate to the VNA extender outside of the cryostat.

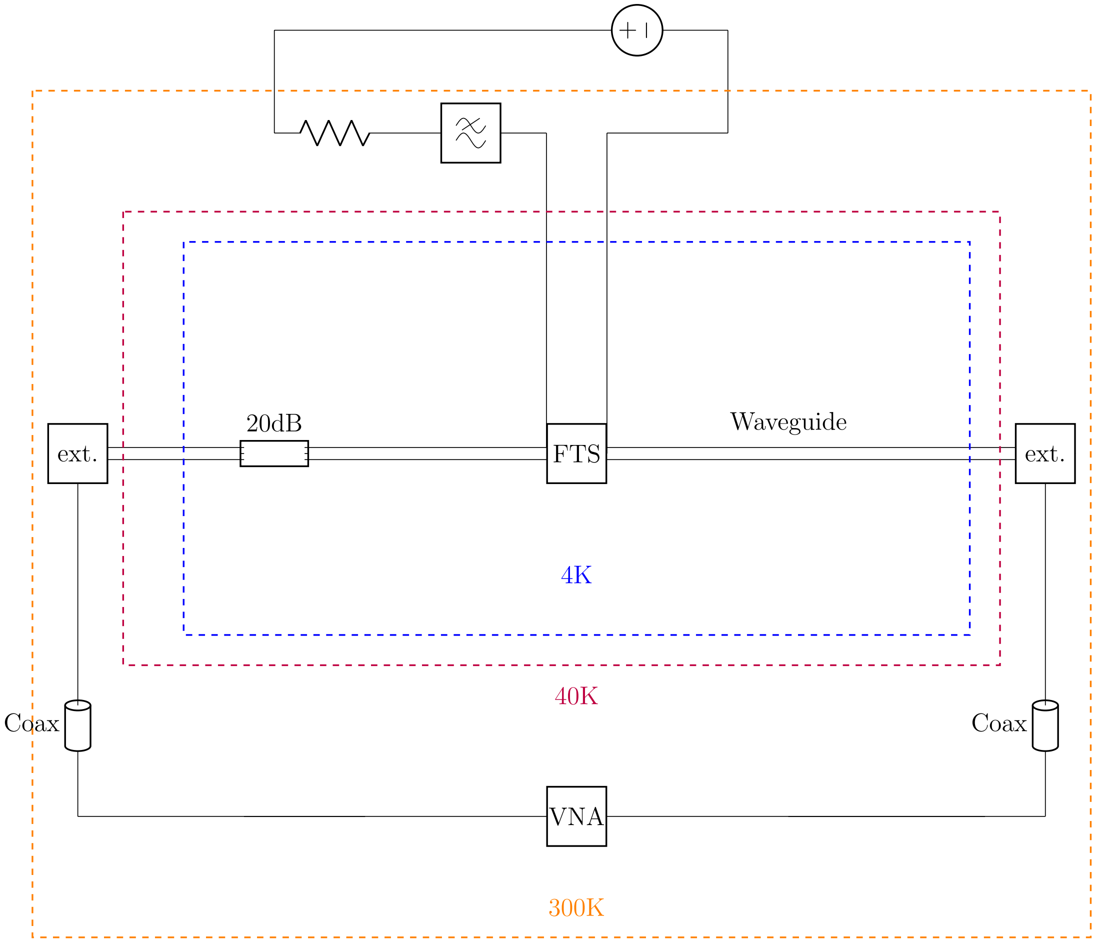

Figure 4.13: Circuit Diagram of the Measurement Test Setup Used for W-band SOFTS.

One end of the stainless steel waveguide is heat sunk at the 40 K stage using copper straps. A second stainless steel waveguide section of 1.4 inches connects the device directly to the 40 K stage (Fig.4.14).

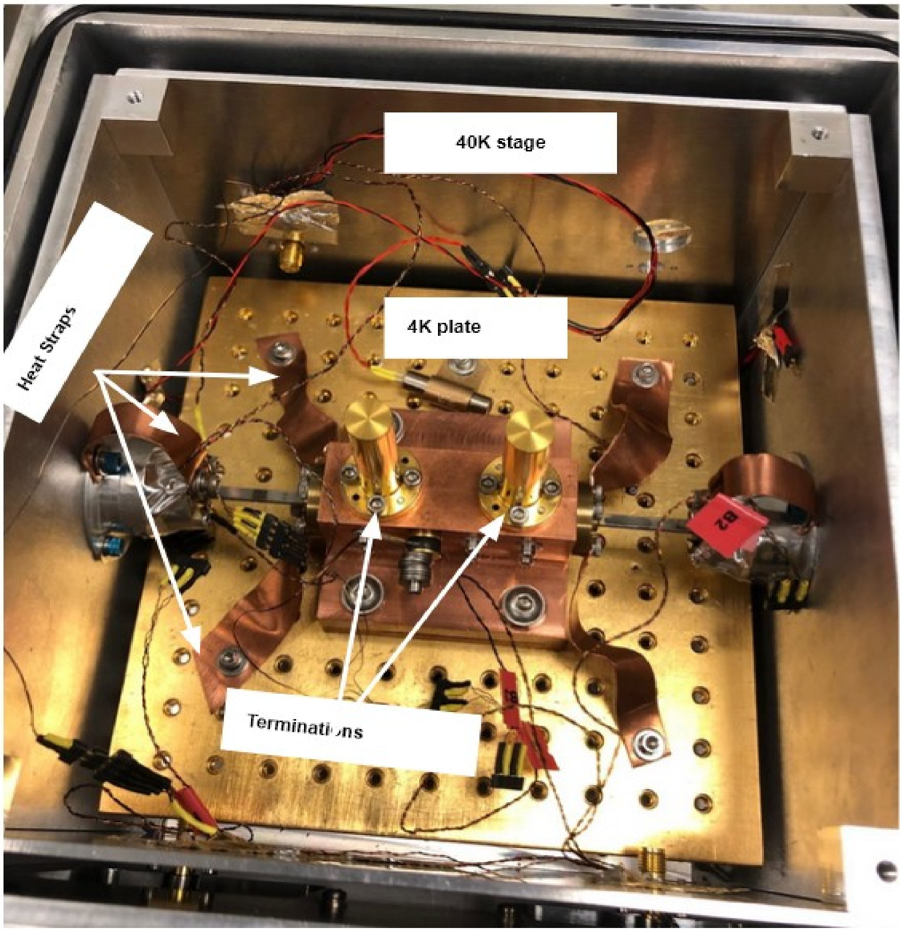

Figure 4.14: SolidWorks Layout of the Cryostat with the SOFTS Housing Mounted to the 3 K Stage.

To DC bias the superconducting transmission line, we used a microstrip printed circuit board (PCB) mounted on the SOFTS housing using silver epoxy and wire bonded the superconducting transmission lines to them. A twisted pair of wires were soldered to the PCB and routed out of the cryostat. We then used a DC power supply with a resistor to current bias the STLs as shown in Fig. B.1.

Heat transfer from 300 K to 40 K occurs through the 3-inch waveguide with the cross-sectional area, A $= 2.2 \times 10^{-6}$ mm^2, and using data from NIST for 304 stainless steel, the heat load on the 40 K stage is

$$\dot{Q} = -\frac{A}{L}\int_{T=\,300\,\mathrm{K}}^{T=\,40\,\mathrm{K}} \kappa(T)\, dT = 80\,\mathrm{mW} \tag{4.3}$$

where L is the length of the waveguide and $\kappa(T)$ is the temperature-dependent thermal conductivity. This value is much less than the cooling capacity of our GM cooler at 40 K, which is 45 W. Following the same procedure, we calculate the heat transfer from the 40 K to 4 k stages through a 1.4-inch long stainless steel material. We expect five mW of heat transfer which is considerably below 1 W of the cooling capacity of our GM cooler at 4 K.

Another consideration is the length contraction of the waveguide due to the high-temperature gradient from the cryostat vacuum flanges at 300 K to the device housing mounted on the 4K stage. Using the linear thermal expansion equation,

$$\Delta L = L_0 \alpha_L \Delta T, \tag{4.4}$$

where ΔL is the linear expansion, L_0 is the initial length and α_L is the coefficient of the linear thermal expansion. With $L_0 = 3.4$ inch and α_L for stainless steel is 10 $\mathrm{C}^{\circ -1}$, we expect a thermal contraction of ~ 0.3 mm.

4.5 W-band Measurements

Using the setup in Fig. B.1 we measured the transmission through the housing/chip system. The S_{21} measurements at different temperatures are shown in Fig. 4.15. The transmission is higher at lower temperatures, especially below the superconducting transition temperature ($\sim$ 6 K).

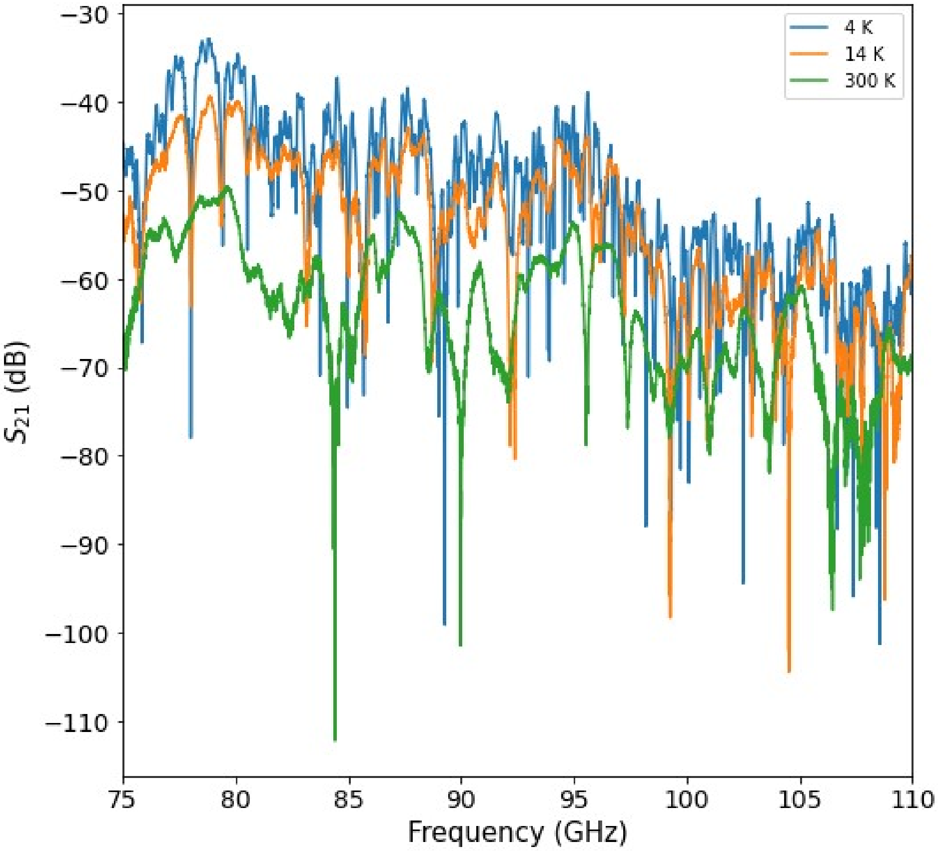

Figure 4.15: Plot of S_{21} Transmission Measurements of the Full Waveguide/Housing/Chip System at 300 K (Orange), 14 K (Green), and 4 K (Blue).

However, the difference between the 4 K measurement and the 14 K measurement is not as significant as we expect it should be for normal versus superconducting states, which is normally within a few tens of dB. To confirm that the chip is superconducting, we measured the DC behavior of the DC-biased transmission line.

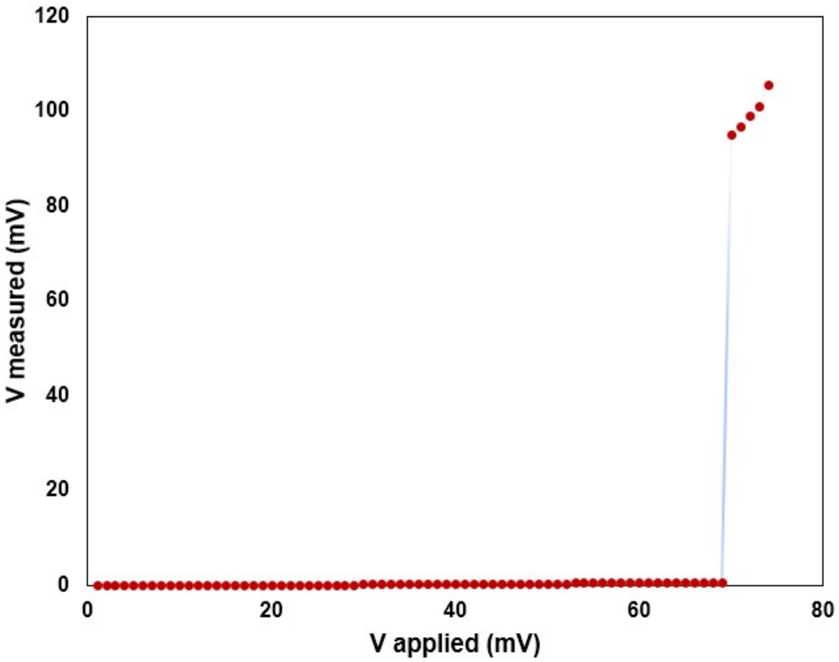

Figure 4.16: Plot of Voltage Across the Superconducting Transmission Line of the SOFTS Device as a Function of Applied Voltage.

Fig.4.16 shows the voltage across the STL. There's an abrupt change in voltage from zero to 100 mV, which indicates the device is superconducting. To confirm the W-band signal is going into and out of the cryostat, we measured the transmission through the waveguide feed-throughs. As we can see from Fig. 4.17, the transmission through the waveguides, bulkhead flange, and mica is about ∼ -3 dB on average across the W-band.

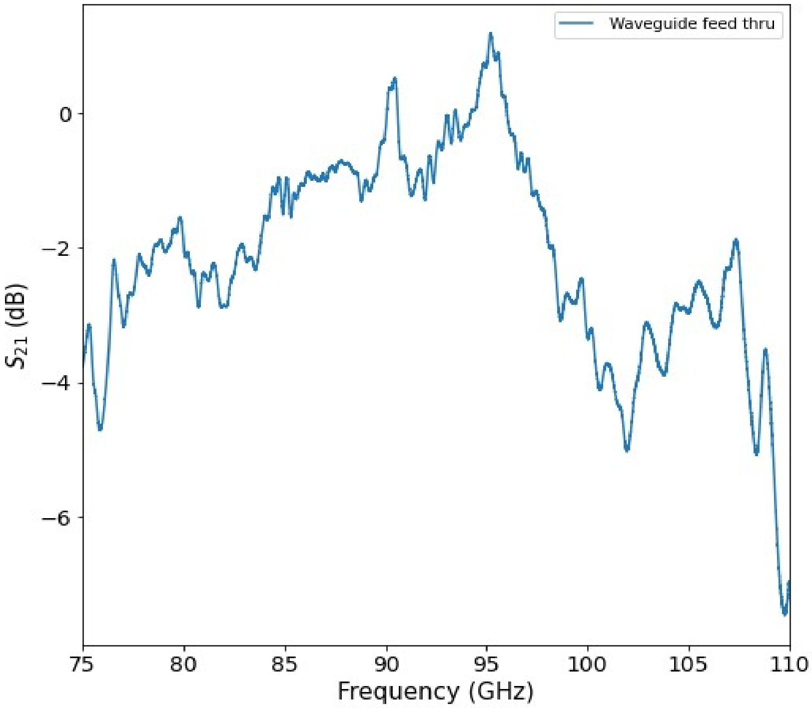

Figure 4.17: Plot of Measured S_{21} of the Waveguide Cryostat Feed Throughs.The Transmission (S_{21}) Through the Waveguides, Bulkhead Flanges, and Mica Windows is About $\sim$ -3 dB on Average Across the W-band. Since this Transmission is Higher than the Transmission Measured with the Devices in Fig. 4.16, we can conclude that the Source of Poor Transmission is not the Feed Throughs.

Another potential issue that can explain the lack of abrupt change in the system's transition below and above the T_c of the device may be poor optical coupling between the split-waveguide housing and the chip. We first measured the transmission through the waveguide bends on the housing to ensure no reflections occurred at the bend.

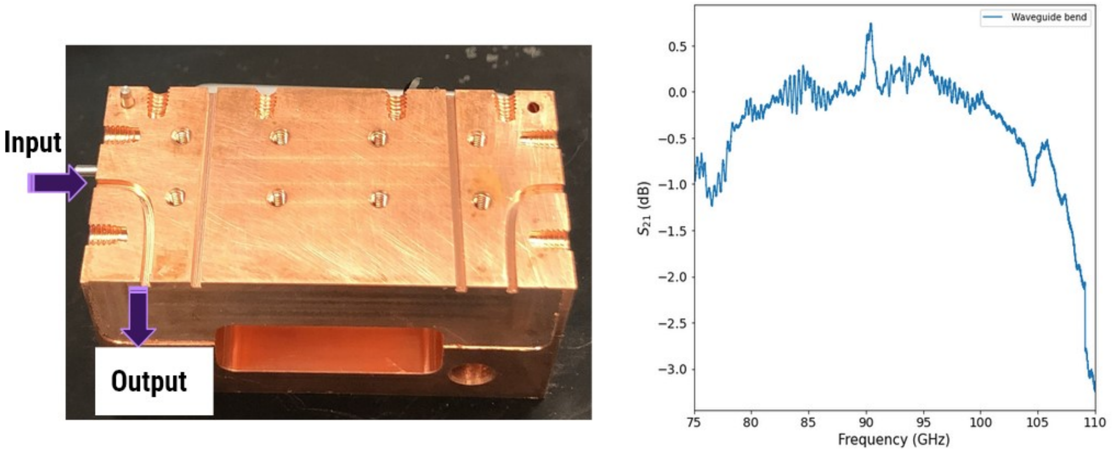

Figure 4.18: *left* Picture of the Waveguide Bend in the Split Block Housing of the SOFTS Device. *right* Plot of Measured S_{21} of the Waveguide Bend in the Split-Block Housing of the SOFTS Chip.

As we can see from Fig. 4.18 we see a transmission of about $\sim$ - 0.5 dB from 75 GHz to 105 GHz range.

The transmission measurements of the waveguide feed-throughs and the waveguide bend in the split block housing confirm there is no problem with getting the signal from the VNA extenders through the waveguides into the cryostat and the waveguide housing. Because the Transmission Measured of All of These Components is Higher than the Transmission Measured with the Devices in Fig. 4.16. Given these measurements, the optical coupling between the housing and the probes on the chip, W-band loss in the superconducting thin film, and the box modes in the thick silicon substrate and the housing are the possible causes of poor radiation coupling.

By looking at Fig. 4.15 we can find regions where the change between the 4 K measurement and the 14 K measurement is greater and look for phase shift in the measured output of the device in those regions.

We calculate the delay by measuring the phase difference between the data with zero bias current and the biased data set and divide by the frequency of the input tone as follows.

$$\tau = \frac{\phi(I) - \phi(I = 0)}{2\pi f_{tone}} \tag{4.5}$$

We can also look at the imaginary and real parts of the tone as a function of the bias current.

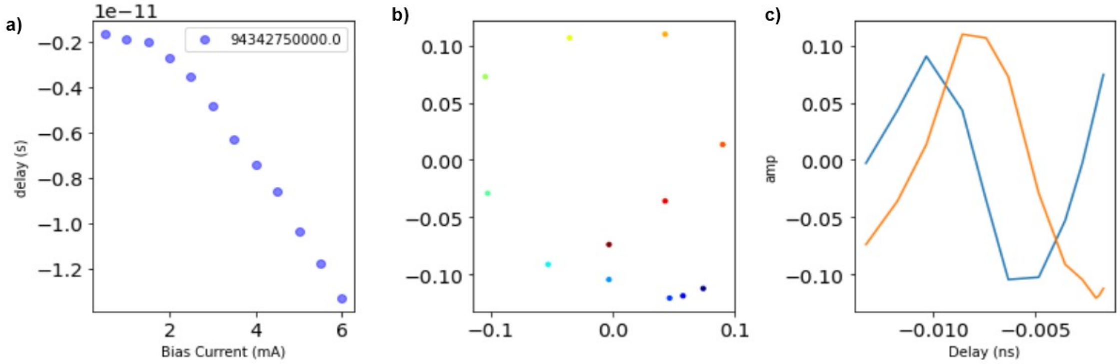

Figure 4.19: *a)* Plot of Measured Delay as a Function of Bias Current, *b* Plot of Imaginary Versus Real Part of the Tone, and *c)* Plot of the Amplitude of the Signal in Each Quadrature as a Function of Delay.

Fig. 4.19 a shows the delay as a function of current bias, and plot b shows the imaginary and real parts of the tone as different bias currents, and plot c shows the amplitude of both imaginary and real parts of the tone. From these plots, we see what looks like one full rotation as we increase the bias current from 0 mA to 5 mA. We can fit the delay vs. bias current data point to the theoretical delay function

$$\tau(I) \approx -K \frac{1}{2} \frac{I^2}{I_*^2} \tag{4.6}$$

where K is $\frac{L_\square l}{Z_0 w}$.

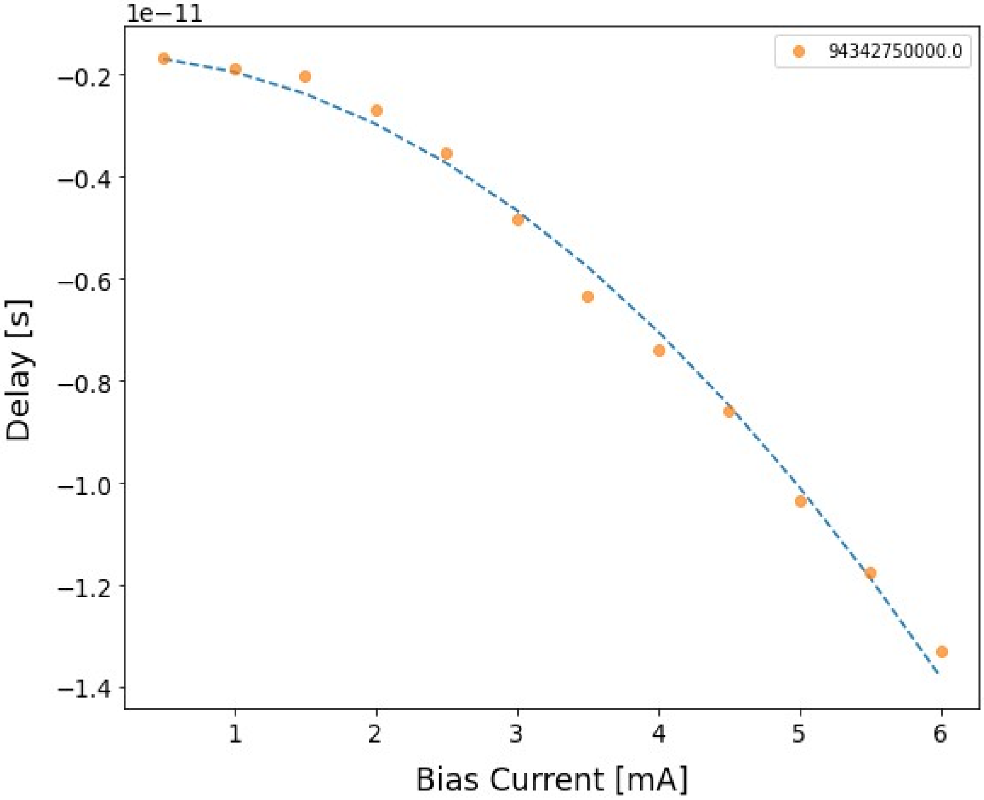

Figure 4.20: Plot of Measured Delayed for a 94.342 GHz Tone as a Function of Applied Current to the Superconducting Transmission Line with the Fit. From this Fit, We Estimate a Characteristic Current of about ~ 25 mA.

The fit parameters extracted from the Fig. 4.20 are $K = 4.80 \times 10^{-10}$s and $I_* = 24.9$ mA. Given that $L_\square = 28\,\text{pH}$, $l = 101\text{mm}$, $W = 15\,\mu\text{m}$ and $Z_0 = 32\ \Omega$, we get a theoretical value of $K = 5 \times 10^{-9}$s (using Equation (2.16)) which is an order of magnitude greater than the fit value. A measurement of the resistance of the STL as a function of the applied voltage is shown in Fig. 4.21. We estimated the critical current of the STL from this plot to be around 0.2 mA which is very low compared to the estimated I_*. Therefore, even if the optical coupling were reasonable, we would not expect a significant delay from this device.

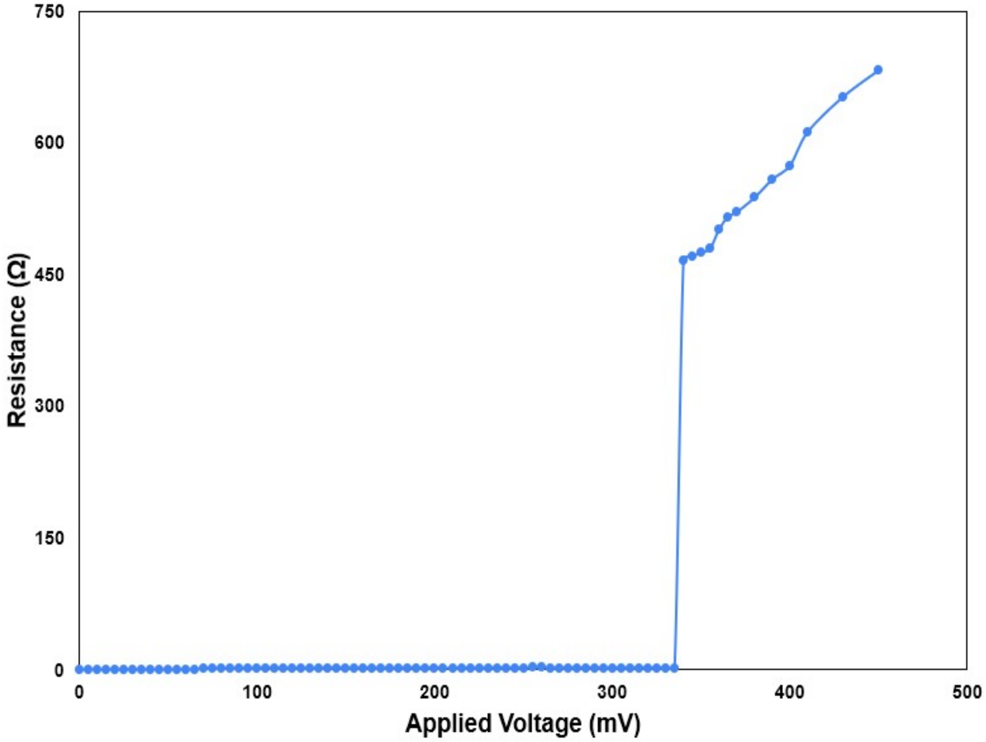

Figure 4.21: Plot of Measured Resistance of the STL as a Function of the Voltage Applied Across the Transmission Line. The Plot has Multiple Jumps Above 0.2 mA and Does Show an Ohmic Behavior. This can be Explained by Assuming Weak Spots on the Transmission Line that go Normal When the Rest of the Circuit Stays Superconducting.

The resistance versus applied voltage plot of the STL has multiple jumps above 0.2 mA and does show an ohmic behavior. This can be explained by assuming weak spots on the transmission line that go normal when the rest of the circuit stays superconducting. As a result, it will produce a negative feedback loop, and the current will drop, as explained in more detail in Klimovich (2022). In this case, we suspect that over-etching of the exposed bias lines in the SiN etch step and the large footprint of the STLs are the main contributors to the problem.

4.6 Summary and Path Forward

The full W-band SOFTS device with a waveguide-coupled cryostat system has been designed and fabricated. W-band testing required a 4-port waveguide setup in a cryogenic environment. We built a comprehensive testing infrastructure, Fig. 4.22. At the device integration level, the chip housing consists of three parts, the top part being the split-block waveguide and a chip holder, which consists of the waveguide backshorts and acts as a heat sink. At the cryostat level, this includes thermo-mechanically robust waveguide coupling; see Fig. 4.22. The scale of commercial waveguide components sets the split-block geometry.

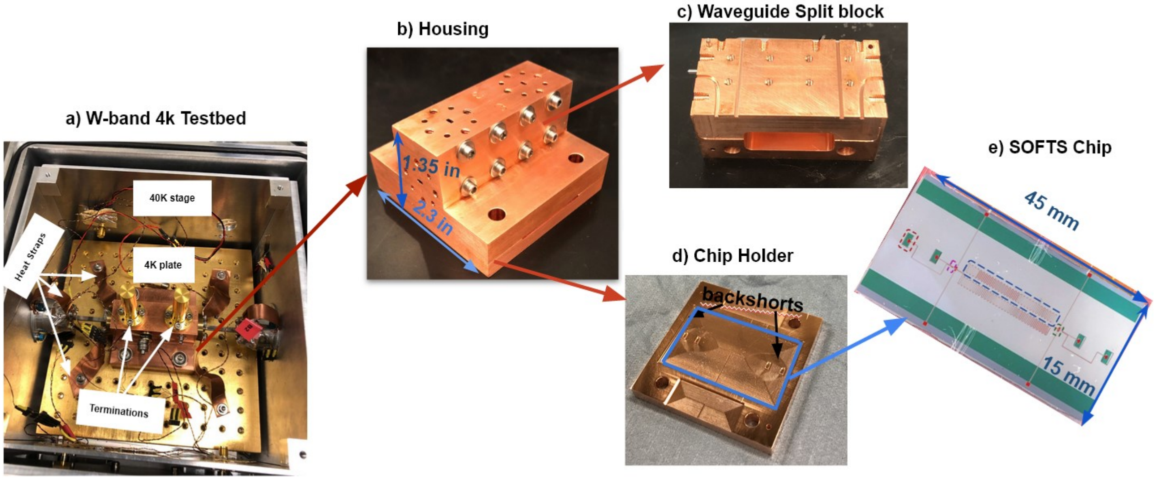

Figure 4.22: a) 4K Cryogenic Test Bed with the SOFTS Measurement Setup, Including the Housing and Waveguide Sections, All Properly Heat Sunk, b) Picture of Housing with Exterior Dimensions, c) Disassembled SOFTS Housing to Show Split-Block Waveguide, d) Bottom Section of SOFTS Housing, Which Functions as a Chip Holder with Backshort Aligners, e) Optical Photograph of Wire-Bonded SOFTS Chip with Dimensions

Matching these dimensions, a NbN W-band SOFTS was fabricated with 20nm of niobium nitride (NbN STL for current-biased non-linearity) and 500 nm of silicon nitride (dielectric layers). The NbN layer was patterned using a reactive ion etching, and the SiN was deposited with a Plasma-Enhanced Chemical Vapor Deposition. We thus developed a complete cryogenic test bed for comprehensive W-band SOFTS testing.

Our initial tests showed that STLs are superconducting; however, interferometric measurements were inconclusive. Since we confirmed that the device is superconducting through a DC measurement but observed poor transmission with the W-band measurements, we suspect that the current design and setup are limited by misalignment between the probes and waveguides due to in-line E-plane coupling design. This problem can be solved by implementing a standard E-plane coupling scheme as shown in Kooi *et al.* (2003) with a proper air channel underneath the microstrip layer to enhance coupling by cutting off box modes. Reducing the footprint of the device also helps with making the thermo-mechanical coupling more robust. It reduces the box modes on top of fabricating the device on a thinner (100 μm) silicon substrate. Another very important factor that needs to be considered for W-band measurements is the base temperature and T_c of the device. Using materials with higher T_c and operating temperatures below 2 K will be essential for future measurements.

Chapter 5

KINETIC-INDUCTANCE TRAVELLING-WAVE PARAMETRIC AMPLIFIER

5.1 Introduction

Direct detectors and heterodyne receivers can benefit from amplifiers with wide instantaneous bandwidth and quantum-limited noise performance as a microwave frequency amplifier and a first-stage amplifier, respectively.
Transistor-based amplifiers are a common choice for frequencies below 100 GHz, but their noise temperature is in the tens of kelvin (Bryerton *et al.* (2013)). Superconducting-insulating-superconducting (SIS) mixers are commonly used at higher frequencies but operate at noise temperatures a few times the quantum-noise limit (Pospieszalski (2012), Kerr *et al.* (2014)). A new promising superconducting amplifier technology is the Kinetic Inductance Traveling-Wave Parametric Amplifier (KI-TWPA) (Eom *et al.* (2012)). The KI-TWPA exploits the nonlinear kinetic inductance of superconducting thin films (Kher (2017)) as a nonlinear medium to amplify an input signal using four-wave and three-wave mixing processes (Goldstein *et al.* (2020), Vissers *et al.* (2016)). These amplifiers have demonstrated quantum noise-limited performance and wide bandwidth for lower frequencies (Klimovich (2022)).

Coherent receivers are an irreplaceable tool for measuring the narrow atomic and molecular lines that trace the cool interstellar medium, providing the primary motivation for the HERO instrument on the Origins Space Telescope (Wiedner *et al.* (2018)) and the HIFI instrument (Helmich (2011)) on the last major far-IR mission, Herschel. At present, the most sensitive technology available for such observations is the SIS mixer. The most advanced SIS mixers achieve a sensitivity of 3-4 times the noise limit imposed by quantum mechanics (Shan *et al.* (2007)) and can instantaneously access 30 GHz of frequency space (Uzawa *et al.* (2021)) or 10-20 percent fractional bandwidth for millimeter and submillimeter bands. An alternative to the SIS mixer is the KI-TWPA because it can achieve quantum-limited noise, as demonstrated at lower frequencies by Klimovich (2022)(Fig.5.1).

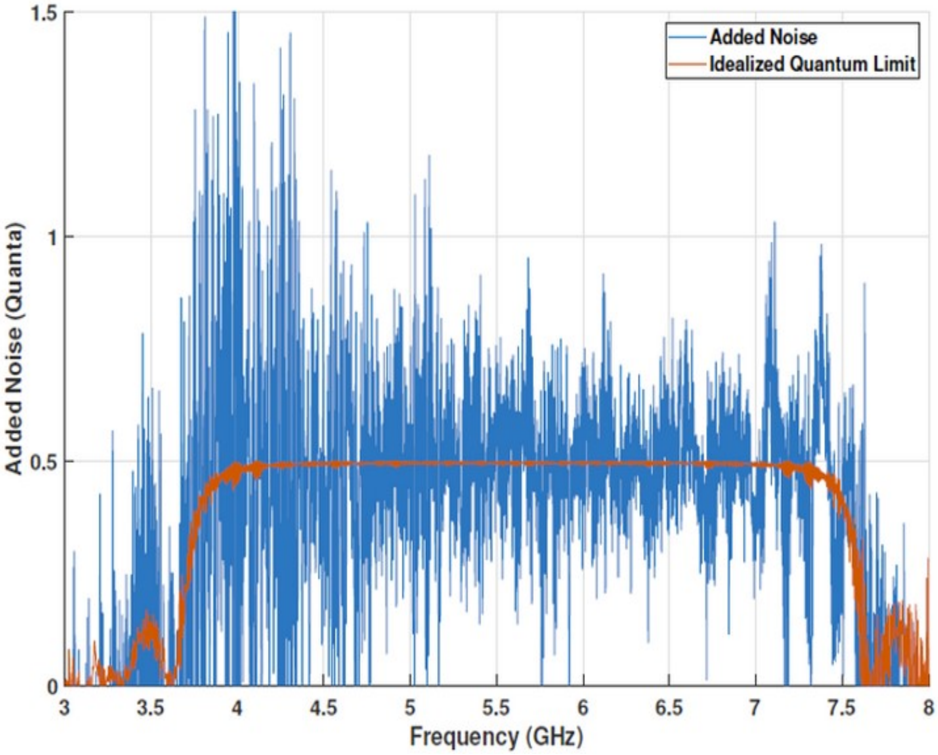

Figure 5.1: The Measured Added Noise in Units of Quanta for the Parametric Amplifier(Blue) Compared to the Theoretical Quantum Noise Limit (Orange). Figure Reprinted From Klimovich (2022)

Moreover, paramps can instantaneously amplify much larger fractional bandwidths (e.g., Fig. 5.2), enabling substantial increases in the speed at which the millimeter/submillimeter spectral range can be surveyed. Through a factor of ten reduction in required integration time and the factor of five to ten improvement in bandwidth, parametric amplifiers can speed up millimeter/submillimeter spectral line studies by a revolutionary factor of 50-100. For ALMA, which must also contend with atmospheric noise, the integration time improvement will be a factor of 3-4 across the frequency range of 100 - 300 GHz, equivalent to nearly doubling the number of antennas in the array.

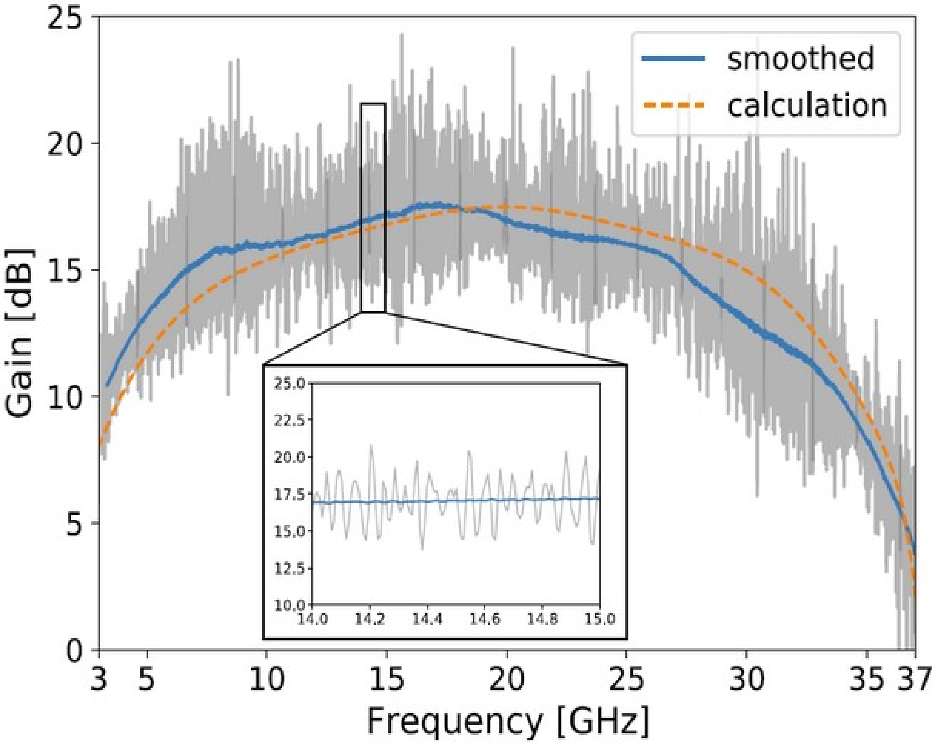

Figure 5.2: Three-Wave Mixing Gain of the Parametric Amplifier Measured at 1 Kelvin with a -29.3 dBm Pump Tone at 38.8 GHz and $I_{DC} = 0.75$mA The Gray Curve Shows the Raw Data as Measured by the VNA, While the Blue Curve is Smoothed Over Frequency and the Inset Shows the Gain Ripple in More Detail. The Orange Curve Shows the Coupled-Mode Calculation for the Expected Performance. Figure Reprinted from Klimovich (2022)

The millimeter-wave and sub-millimeter-wave amplifiers will extend the existing state-of-the-art by providing quantum-noise-limited gain blocks through the millimeter-wave band. Improving receiver sensitivity would be a basic and relatively low-cost way to enhance the scientific value of any instrument employing heterodyne receivers.

The Low-Temperature Detector (LTD) technologies that would benefit from parametric amplifiers are the primary candidate sensors for imaging, polarimetry, and spectroscopy for a broad range of astrophysics missions operating in the millimeter/submillimeter/far-infrared bands and also in the X-ray region. Low-temperature detectors, particularly MKID and SNSPD arrays, have potentially transformative applications in the ultraviolet, visible, near-infrared, and mid-infrared bands.

Quantum-limited amplifiers have a wide range of applications in quantum information science (QIS) and quantum sensing. For example, quantum noise-limited amplifiers allow fast and high-fidelity readout of superconducting qubits (Peng *et al.* (2022); Barzanjeh *et al.* (2014); Didier *et al.* (2015)). KI-TWPAs are an appealing choice for the readout of a large number of qubits due to their high dynamic range, wideband, and quantum-limited performance(Ranzani *et al.* (2018)). Taking advantage of the three-wave mixing process in DC-biased TWPAs, we can utilize photon entanglement and quantum squeezing for applications in quantum communication and sensing (Zorin (2019); Klimovich (2022)). In addition, with the advent of millimeter-wave quantum systems (Faramarzi *et al.* (2021); Suleymanzade (2021)), there will be a need for millimeter-wave quantum noise-limited amplifiers. Recently, more research groups have been using quantum-noise-limited amplifiers for fundamental physics experiments such as dark matter searches (Asztalos *et al.* (2010); Dixit *et al.* (2021); Bartram (2021)). KI-TWPAs in the hundreds of GHz range can be good candidates for experiments of heaver dark matter candidates (Ramanathan *et al.* (2022)).

Non-linearity and Kerr Coefficient

For a superconducting transmission line with non-linear kinetic inductance per unit length of

$$\mathcal{L}_K(I) = \mathcal{L}_0\left(1 + \frac{I^2}{I_*^2} + ...\right) \tag{5.1}$$

where I_* is the scale of non-linearity, the phase velocity is given by

$$v_{ph} = \frac{1}{\sqrt{\mathcal{L}(I)\mathcal{C}}} \tag{5.2}$$

where $\mathcal{L}(I) = \mathcal{L}_K(I) + \mathcal{L}_G$ is the total inductance per unit length of the transmission line. Re-writing Equation (5.2), we get

$$\begin{aligned} v_{ph} =& \frac{1}{\sqrt{(\mathcal{L}_K(I) + \mathcal{L}_G)\mathcal{C}}} = \frac{1}{\sqrt{\mathcal{C}}}\left[\mathcal{L}_G + \mathcal{L}_0\left(1 + \frac{I^2}{I_*^2}\right)\right]^{-\frac{1}{2}} \\ =& \frac{1}{\sqrt{\left(\mathcal{L}_0 + \mathcal{L}_G\right)\mathcal{C}}}\left[1 + \frac{\mathcal{L}_0}{\mathcal{L}_0 + \mathcal{L}_G}\frac{I^2}{I_*^2}\right]^{-\frac{1}{2}} \\ v_{ph}(I) =& v_{ph}(0)\left[1 + \alpha\frac{I^2}{I_*^2}\right]^{-\frac{1}{2}} \approx v_{ph}(0)\left[1 - \frac{\alpha}{2I_*^2}I^2\right]. \end{aligned} \tag{5.3}$$

The magnitude of the Kerr effect (quadratic non-linearity) is then proportional to

$$\text{Kerr Magnitude} \propto \frac{\alpha}{I_*^2} \tag{5.4}$$

the magnitude of the Kerr effect scales with the normal resistivity of the superconducting thin film ρ_n.

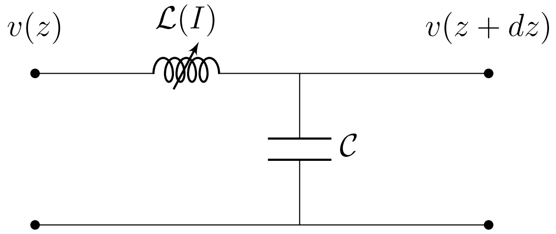

Figure 5.3: Lumped-Element Model of a Superconducting Transmission Line.

Coupled-Mode Equation

The telegrapher equation for a non-linear superconducting transmission line with a high Q substrate can be written as follows

$$\frac{\partial^2 I}{\partial z^2} - \frac{\partial}{\partial t}\left[\mathcal{L}(I)\,\mathcal{C}\frac{\partial I}{\partial t}\right] = 0 \tag{5.5}$$

assume a solution of the form

$$I = \frac{1}{2}\left(\sum_n A_n(z)e^{i(k_n z-\omega_n t)} + c.c\right). \tag{5.6}$$

For the four-wave mixing (4WM) case we have the pump tones (ω_{p1},ω_{p2}), the signal tone (ω_s) and the idler tone (ω_i) which obey the following relation

$$\omega_i = \omega_{p1} + \omega_{p2} - \omega_s \tag{5.7}$$

for the degenerate 4WM case, $\omega_{p1} = \omega_{p2} = \omega_p$.

Plugging Equation (5.6) into the telegrapher equation and applying the SVEA approximation, we get the following equations for the rate of change of amplitudes of each tone.

$$\begin{aligned}\frac{\mathrm{d}A_p}{\mathrm{d}z} &=\frac{i\omega_p}{8v_{ph}(0)I_*^2}\left[\left(|A_p|^2+2|A_s|^2+2|A_i|^2\right)A_p+2A_sA_iA_p^*\exp\{i\Delta\beta z\}\right]\\ \frac{\mathrm{d}A_s}{\mathrm{d}z} &=\frac{i\omega_s}{8v_{ph}(0)I_*^2}\left[\left(|A_s|^2+2|A_i|^2+2|A_p|^2\right)A_s+A_p^2A_i^*\exp\{-i\Delta\beta z\}\right]\\ \frac{\mathrm{d}A_i}{\mathrm{d}z} &=\frac{i\omega_i}{8v_{ph}(0)I_*^2}\left[\left(|A_i|^2+2|A_s|^2+2|A_p|^2\right)A_i+A_s^*A_p^2\exp\{-i\Delta\beta z\}\right]\end{aligned} \tag{5.8}$$

where $\Delta\beta = k_s + k_i - 2k_p$.

The 4WM process creates odd pump harmonics $(2n+1)\,\omega_p$ with $n = 1, 2, 3, ..$ and tones of $(2n+1)\,\omega_p \pm (\omega_s - \omega_p)$ which are upper and lower sideband frequencies. By implementing geometric dispersion in the transmission line, we can control the phase matching. This technique is referred to as Dispersion Engineering (Shu *et al.* (2021)). Using dispersion engineering, we can create a mismatch that does not allow higher-frequency tones to interact coherently with lower-frequency tones.

Since the signal tone is weaker, we can drop those terms. We also assume $\frac{\mathrm{d}|A_p|}{\mathrm{d}z} = 0$, which means the pump is undepleted; thus, the first line in Equation(5.8) becomes

$$A_p(z) = A_p(0)\, exp\left(\frac{i\omega_p|A_p|^2 z}{8v_{ph}(0)I_*^2}\right) \tag{5.9}$$

Non-linearity of the circuit introduces an additional phase-shift of

$$\Delta\phi_p = \frac{\omega_p|A_p|^2}{8v_{ph}(0)I_*^2} \tag{5.10}$$

due to the nonlinear kinetic inductance of the transmission line, the pump tone interacts with itself and causes this additional phase shift called the *self-phase modulation*. The same interactions between the pump tone and the idler and signal tones produce phase shifts, as indicated below. These are called *signal-cross modulation* and *idler-*

cross modulation. As the pump power P_{in} is proportional to $|A_p|^2$, the self-phase modulation is linear in pump input power.

We can then solve Equations (5.8) analytically for $\omega_s \approx \omega_i$. Following Hansryd *et al.* (2002), Stolen and Bjorkholm (1982) and Eom *et al.* (2012) the signal gain can be written as

$$G_s = 1 + \left(1 + \frac{\Delta\phi_p}{g} \sinh gL\right)^2 \tag{5.11}$$

Where L is the length of the transmission line and g is the gain factor, and it is given by

$$g = \frac{1}{2}\sqrt{(2\Delta\phi_p)^2 - k^2} \tag{5.12}$$

where $k = \Delta\beta + 2\Delta\phi_p^2$,

$$G_s \approx 1 + \left(L\Delta\phi_p\right)^2 \tag{5.13}$$

Where $\Delta\phi$ is the phase shift of the pump tone, the gain is quadratic in the length of the transmission line due to phase mismatch caused by non-linearity. This is the case for dispersionless superconducting transmission lines.

To achieve maximum gain, we require $k = 0$ or

$$\Delta\beta = -2\Delta\phi_p = \frac{\omega_p|A_p|^2}{8v_{ph}(0)I_*^2} \tag{5.14}$$

This will result in an exponential gain of

$$G_s = \frac{1}{4}\exp\{\Delta\phi L\} \tag{5.15}$$

Therefore the phase-matching criterion for exponential gain is given by

$$\Delta\beta = k_s + k_i - 2k_p = \frac{\omega_p |A_p|^2}{8 v_{ph}(0) I_*^2} \tag{5.16}$$

It should be noted that in most cases, we are not operating around $\omega_p \approx \omega_s$, and therefore, we need to solve Equations (5.8) numerically to estimate the bandwidth of the KI-TWPA and its gain.

5.3 Low-Frequency KI-TWPA

5.3.1 Device Design

The KI-TWPA devices were designed and fabricated at JPL's Micro-Devices Laboratory (MDL). Some of the fabricated devices were provided by Dr. Peter Day to Sasha Sypkens and myself for testing in the 4 K cryogenic testbed at ASU. These measurements were supervised by Dr. Day. The devices are made of a 35 nm thick NbTiN on a silicon wafer. The transmission line made of the NbTiN is a microstrip geometry with amorphous silicon (a-Si) as a dielectric layer and a thick NbTiN layer as the ground plane. The width of the transmission line is designed to be 250 nm to maximize the Kerr non-linearity, which means a very low characteristic current I_*. To keep the characteristic impedance around 50 Ω, a series of open microstrip stubs were added to the transmission line to increase the capacitance per unit length and decrease the impedance. Adding a periodic modulation to the length of the microstrip stubs allows dispersion engineering to suppress the unwanted non-linear processes in the device, such as higher harmonic generation. For more details, refer to Shu *et al.* (2021).

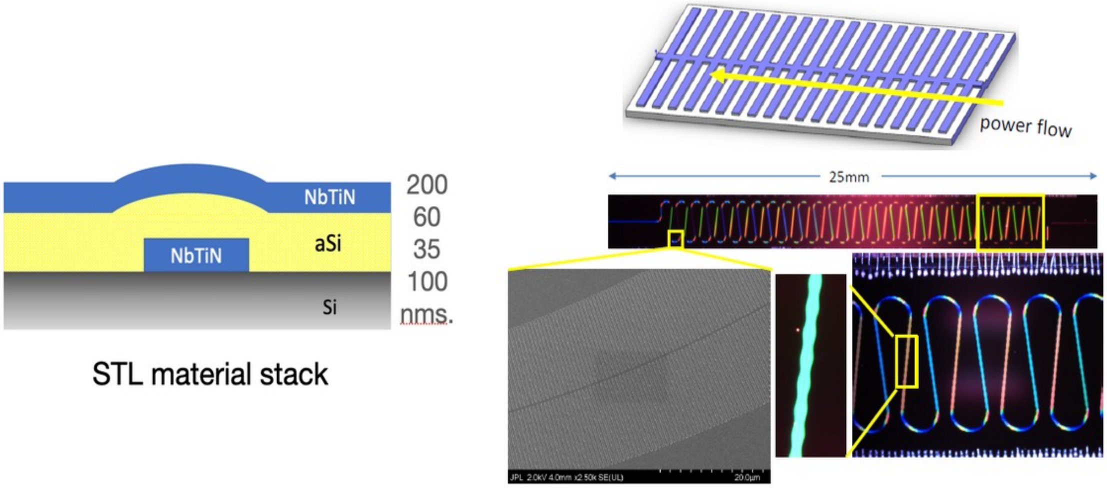

Figure 5.4: *left* Drawing of The Material Stack of the Microstrip Structure Used for KI-TWPA (Reprinted from Shu *et al.* (2021)). The Numbers Next to the Layers is the Thickness in Nanometers. *right* Picture of the KI-TWPA Chip with Detail of the Device (Courtesy of Dr.Day).

5.3.2 Four-Kelvin Measurements

To measure the KI-TWP in the cryostat, the VNA input signal port was routed with a series of copper/stainless steel cables, a DC block, and a 20 dB attenuator to the KI-TWPA device at the 4K plate. The signal is then routed back to the VNA from the device with a series of cables and a DC block. To add the pump tone to the input of the device, we used a signal generator and a power combiner, and we combined the pump tone with the signal coming from the VNA. The circuit diagram used for the four-kelvin measurements is shown in Fig. 5.5.

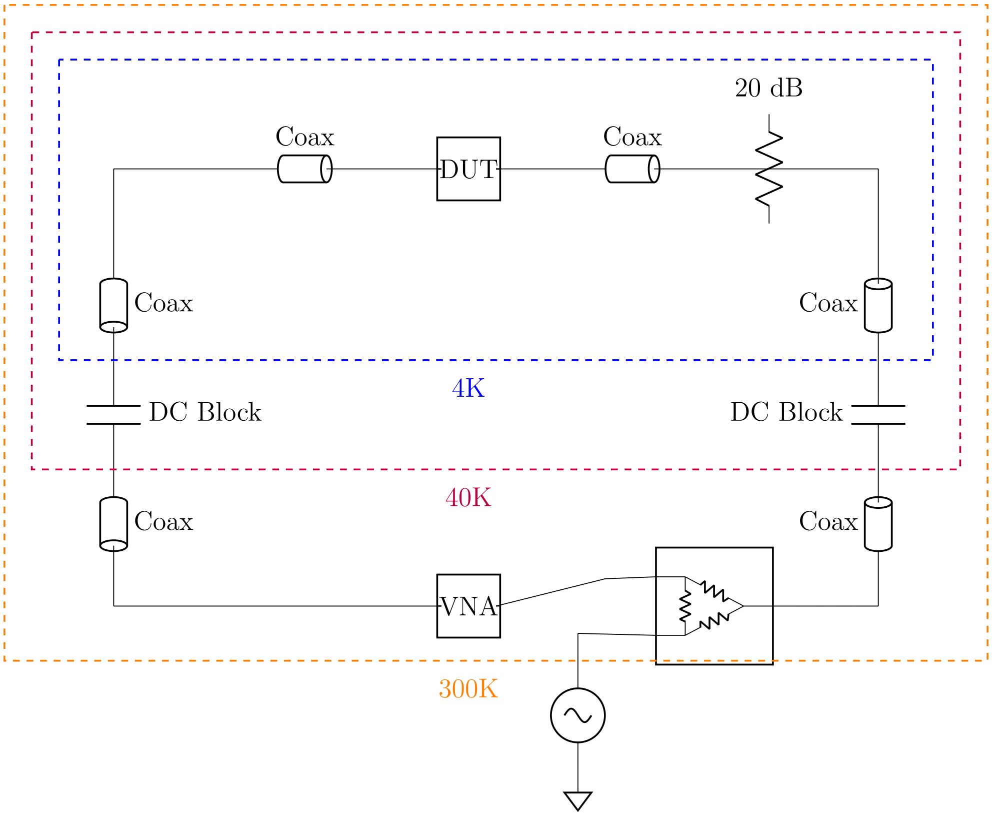

Figure 5.5: Circuit Diagram of the 4 K Measurement Test Setup for the KI-TWPA.

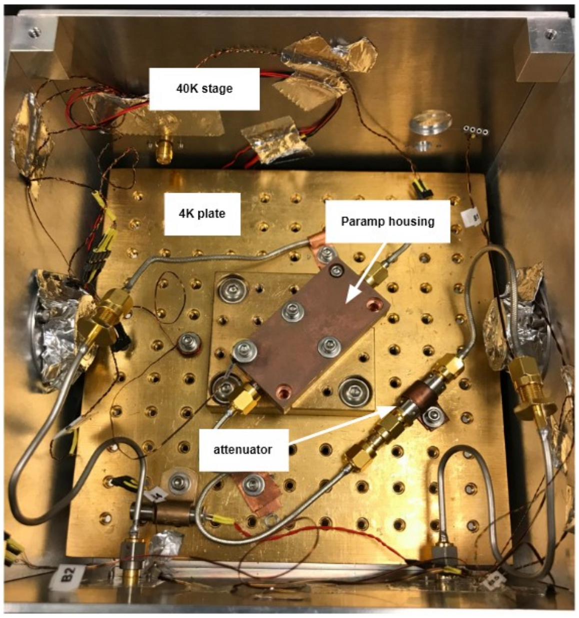

Figure 5.6: Picture of the Cryogenic Testbed Used for KI-TWPAs Measurements at 4 K.

First, we look at the transmission of the device with the pump off to look for the bandgap, as shown in Fig. 5.7

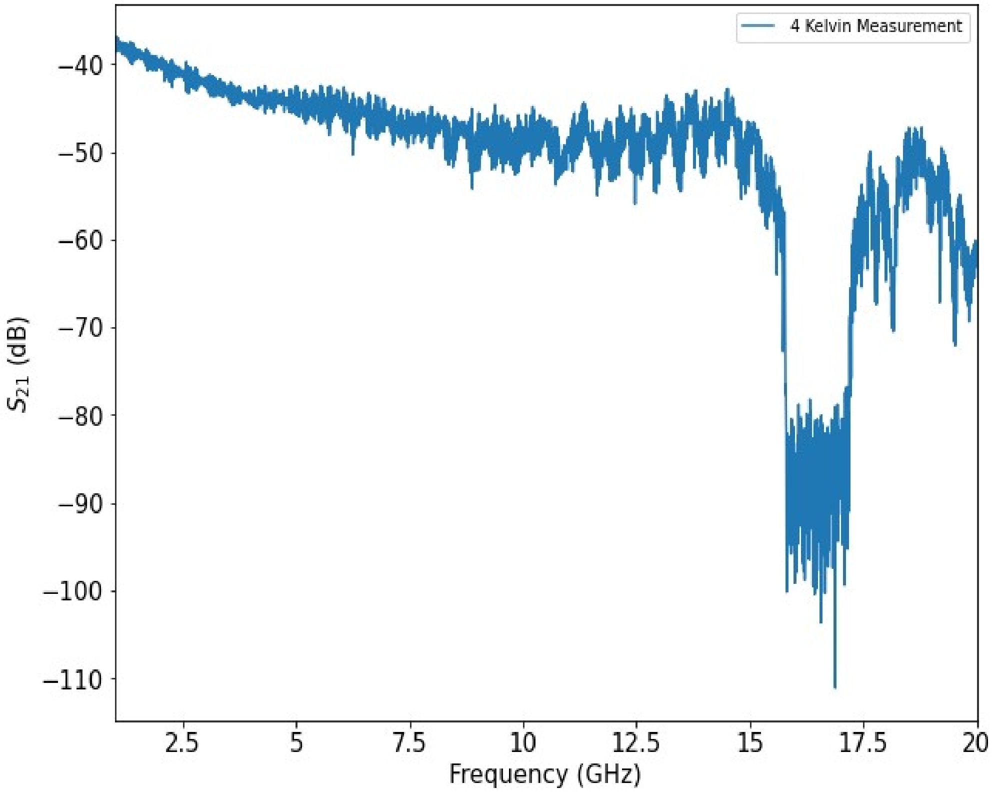

Figure 5.7: Plot of Measured S_{21} in dB of a KI-TWPA Device at Four Kelvin with Pump Tone Off with Frequency. The Band Gap for this Device was Designed to be Near $\sim$ 17 GHz.

For Four-Wave Mixing (4WM) operation (explained in Section 5.2), we apply the pump tone below the bandgap of the paramp and adjust both the frequency and the input power of the gain tone to maximize the amplified output signal. For the above device, we see a wide-band gain between 1 GHz - 10 GHz with a maximum gain of around 22 dB. The gain plot is made by dividing the measured S_{21} with the pump tone on by the S_{21} when the tone power is off. The pump tone power for this measurement was 15 dBm, and the frequency of the pump was 5.5 GHz.

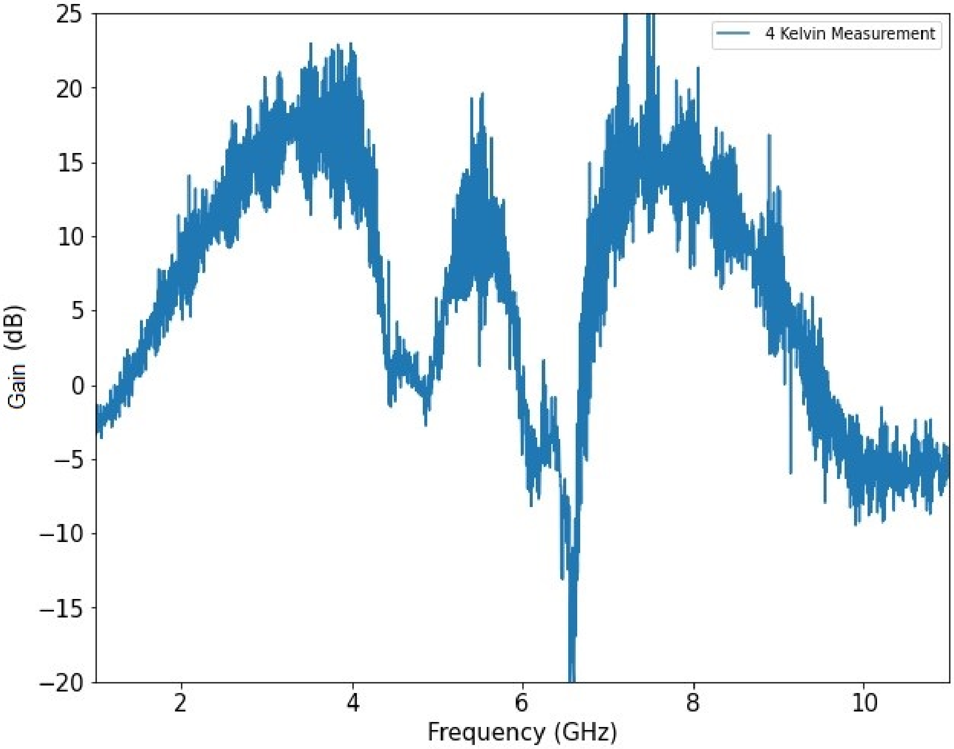

Figure 5.8: Plot of Measured Gain of Device 19b5 with Pump Tone of 5.5 GHz and Pump Power of 15 dBm at the Signal Generator.For the Above Device, we See a Wide-band Gain Between 1 GHz - 10 GHz with a Maximum Gain of Around 22 dB. The Gain Plot is Made by Dividing the Measured S_{21} with the Pump Tone on by the S_{21} When the Tone Power is off.

It is important to note for GHz frequency paramp devices operating at 4 Kelvin temperatures, loss in the transmission of the device will degrade the gain performance and is not directly indicative of lower temperature operation. An interesting property of the 4WM KI-TWPA devices is the frequency translating gain operating mode, where the signal gain of the device can be tuned by changing the frequency of the pump tone below the bandgap frequency. The relationship between the signal, idler, and pump tones (for the 4WM case) given by

$$2\omega_p = \omega_s + \omega_i \tag{5.17}$$

where ω_p , ω_s, and ω_i are the pump,signal and idler frequencies respectively.

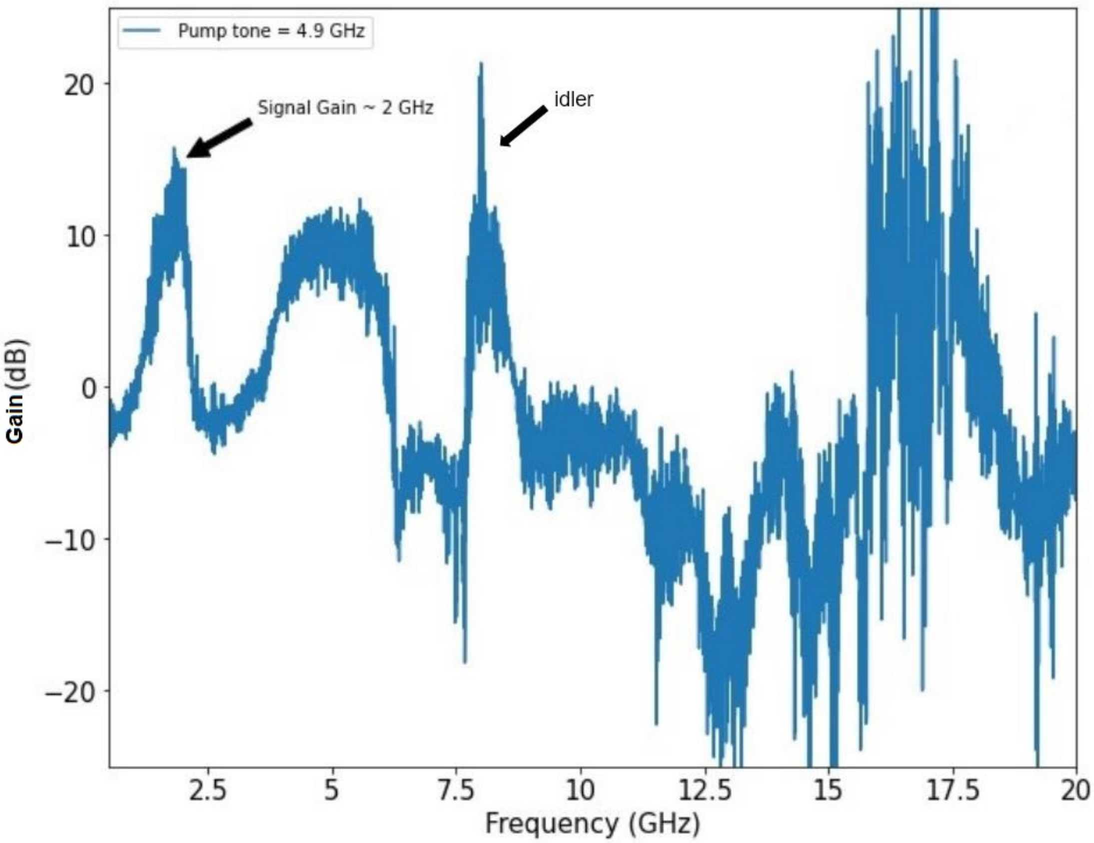

Figure 5.9: Plot of Measured Gain of the 19b5 Device with Pump Tone at 4.9 GHz. The Signal Gain Measured Here is at 2 GHz, and the Mirrored Image of the Signal or the Idler Tone is at $\sim$ 7 GHz. Using Equation (5.12), the Measured Values Agree with the Relationship Between Different Tones in the 4WM Mode of Operation for the KI-TWPA. We Can Use This Operating Mode of the KI-TWPAs to Amplify a Low-frequency Signal and Terminate the Amplified Signal and Measure the Idler Tone Instead.

The above relation indicates that changing the pump tone will shift both the signal and idler gain frequencies. Fig. 5.9 shows a measurement of a 4-wave mixing gain with frequency translation property measured at 4 Kelvin. The pump tone is set to $\omega_p = 2\pi \times 4.9$ GHz, and signal tone gain is observed at $\omega_s = 2\pi \times 2$ GHz with idler tone at $\omega_i = 2\pi \times 7.6$ GHz. Using Equation (5.12), the measured values agree with the relationship between different tones in the 4WM mode of operation for the KI-TWPA. We can use this operating mode of the KI-TWPAs to amplify a low-frequency signal and terminate the amplified signal and measure the idler tone instead. Since the idler tone is higher in frequency, we can acquire more gain and tune the idler frequency in a band where commercial electronics are available.

5.3.3 Diplexers

To improve the performance of the KI-TWPA devices, there will be a need for on-chip superconducting circuitry to reduce ripples and manage the pump tone. Using a diplexer, we direct the pump tone into the transmission line and direct it out with a second diplexer, and terminate at the 4K stages (Fig. 5.10).

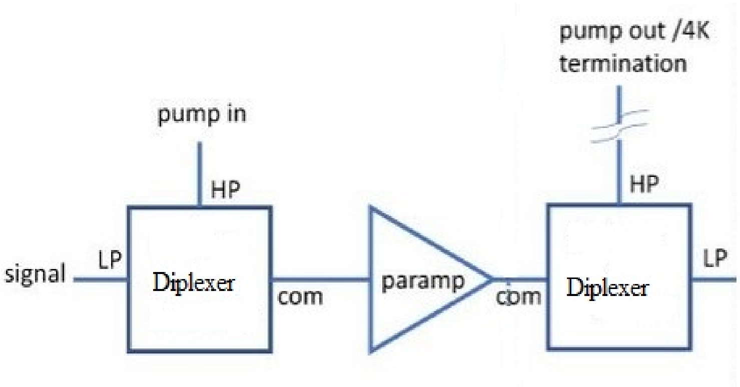

Figure 5.10: Drawing of the Diplexer Paramp Circuit for Pump Management and Ripple Reduction.

The low-pass port of the diplexer can be used to DC bias the transmission line for a 3WM KI-TWPA or terminated otherwise. In addition, a high return loss at the common port can help reduce the gain ripples by suppressing reflections. Currently, we have been using commercial diplexers for some of the paramp measurements. However, moving forward, we need to use superconducting on-chip circuitry integrated with the paramp chip for the following reasons: (a) different diplexer cross-over frequencies can be easily designed for a specific application. (b) superconducting circuits are ultra-low loss (c) filtering on-chip immediately after and before the transmission line improves the overall performance of the KI-TWPA.

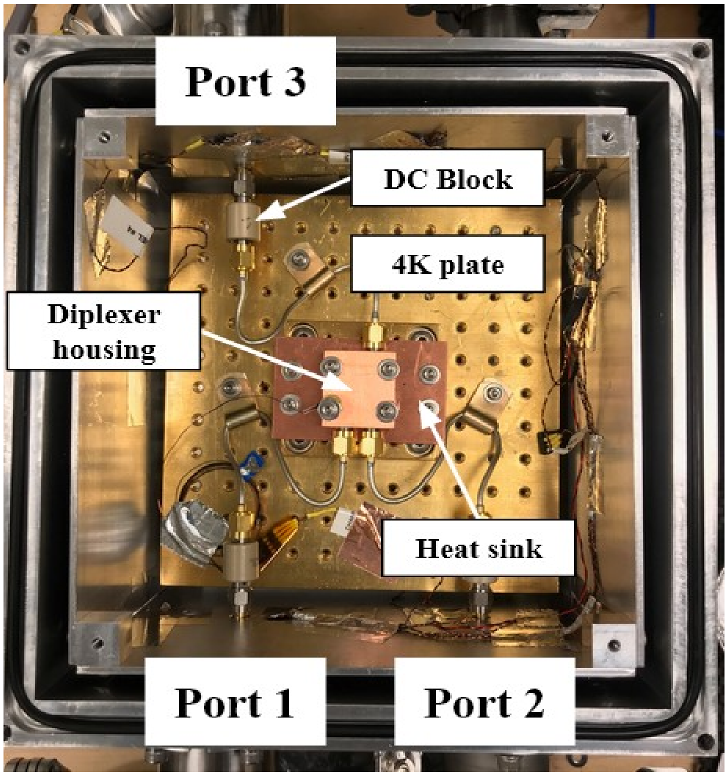

Figure 5.11: Picture of the 4 Kelvin Cryogenic Testbed Used for Measuring Diplexers. We Used Three Ports of a 4-Port VNA to Measure All the S Parameters of the Device Simultaneously.

The diplexers were designed by Dr. Peter Day and fabricated at StarCryo CO. They are made of a thick Nb layer (~ 200 nm), and a 500 nm thick SiN layer has been used as the dielectric layer. The chip was housed in a copper enclosure with a PCB bridging the V-connectors on the enclosure to the wirebonds and the chip. We used three ports of a 4-port Rhode & Schwartz Z24 VNA to measure all the s-parameters of the diplexers simultaneously.

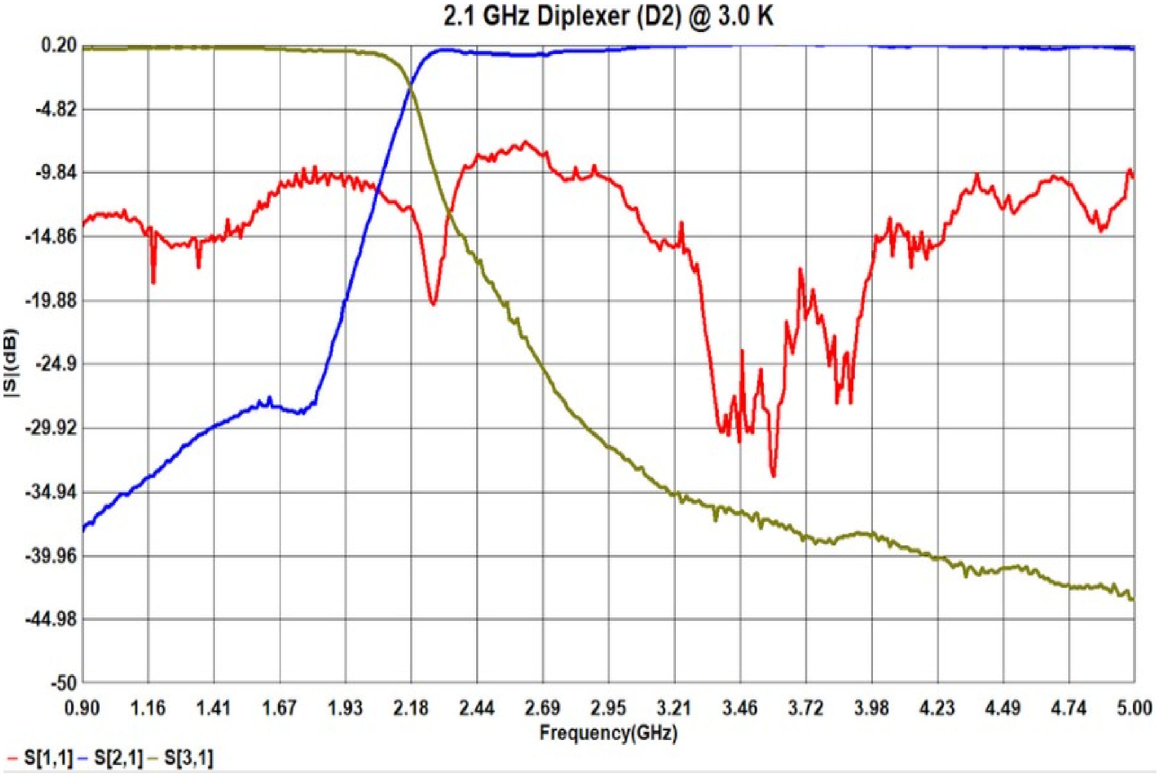

Figure 5.12: Plot of Measured S-Parameters of Diplexer D2 with a Cross-Over Frequency of 2.1 GHz. *Blue* and *Green* are the Response of the High-Pass and Low-Pass Ports, Respectively. *Red* is the Return Loss of the Common Port.

Four diplexers were designed with cross-over frequencies of 2, 4, 10, and 26 GHz. We measured the first three at ASU at 3.05 Kelvin. Fig. 5.12 shows the measured S-parameters of the device. The return loss of the common port is shown in red, which is not as low as expected. Usually, a return loss of 15 dB or higher would minimize the gain ripples.

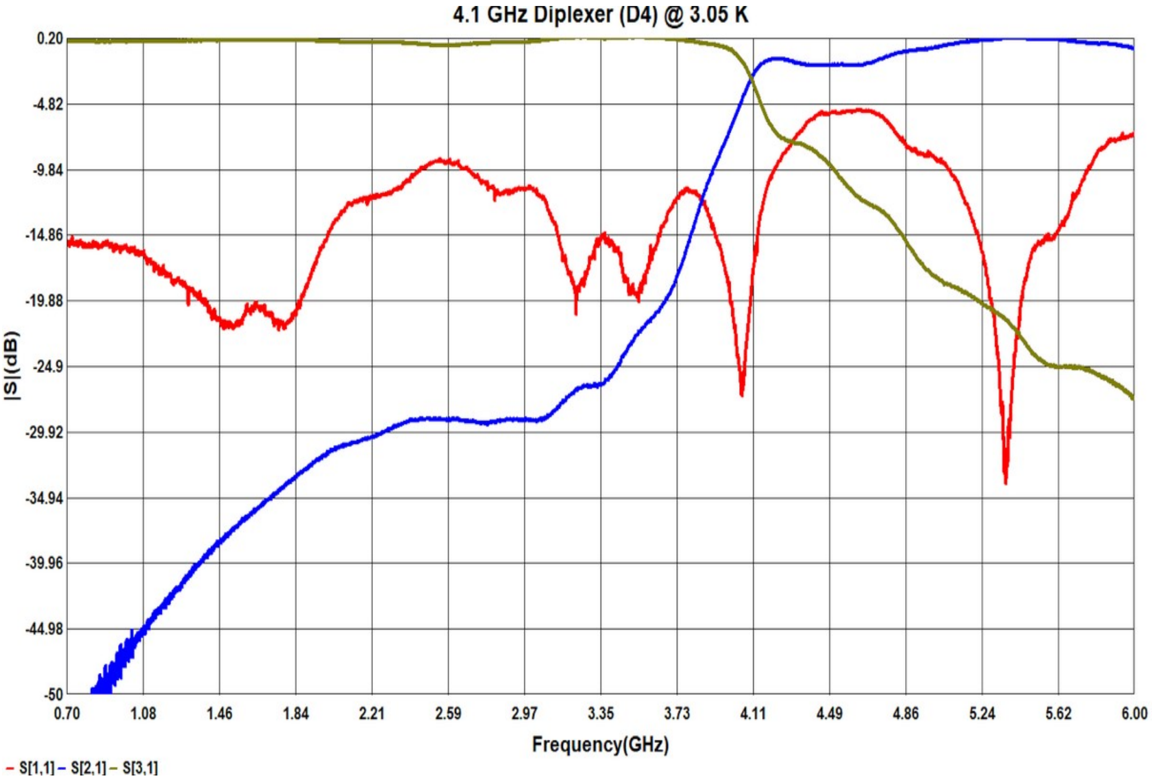

Figure 5.13: Plot of Measured S-Parameters of Diplexer D4 with a Cross-Over Frequency of 4.1 GHz. Blue and Green are the Response of the High-Pass and Low-Pass Ports, Respectively. Red is the Return Loss of the Common Port.

The diplexer with a cross-over frequency of 4 GHz has a very low return loss on the common port above 4 GHz, which not only is not ideal, but it is degrading the performance of the high pass port due to reflections.

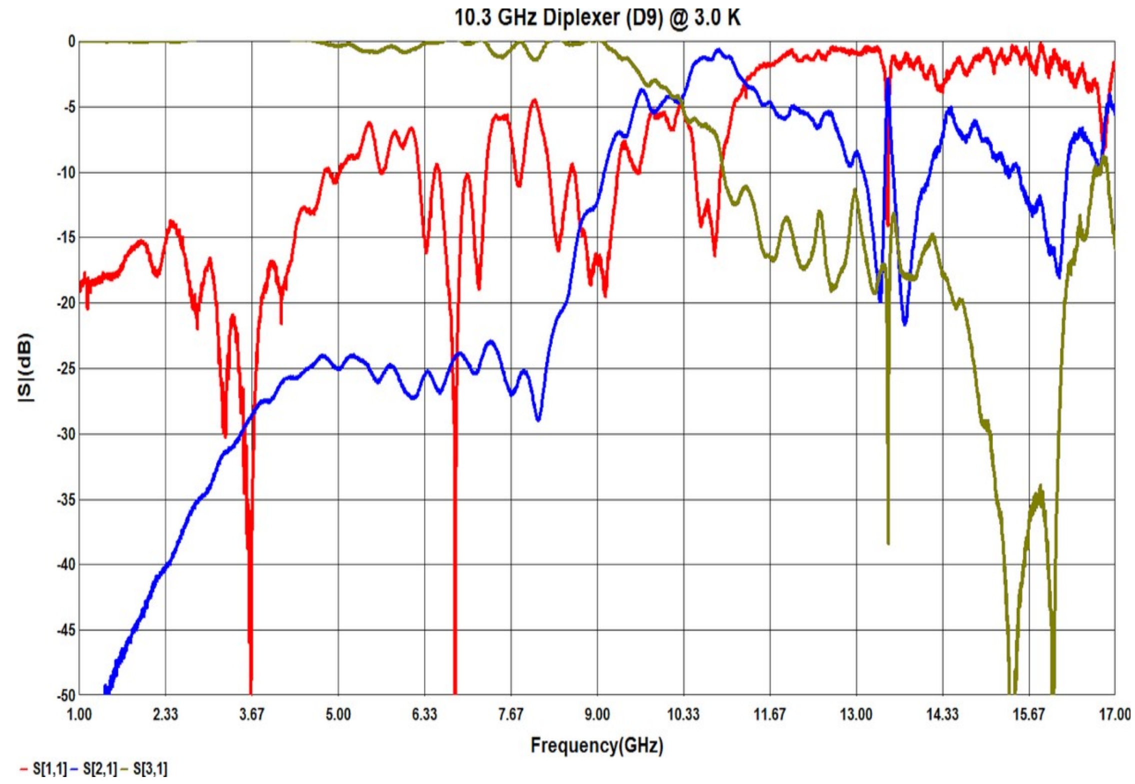

Figure 5.14: Plot of Measured S-Parameters of Diplexer D9 with a Cross-Over Frequency of 10 GHz. Blue and Green are the Response of the High-pass and Low-pass Ports, Respectively. Red is the Return Loss of the Common Port. This Diplexer Did not Perform as Expected Due to the High Return Loss of the Common Port ($\geq$ -10 dB) on Average Across the Measurement Band and the Poor Transmission of the High Pass Filter Above the Cross-over Frequency.

Unfortunately, the 10 GHz diplexer we tested at 4K did not perform as expected due to the high return loss of the common port ($\geq$ -10 dB) on average across the measurement band and the poor transmission of the high pass filter above the cross-over frequency as shown in Fig. 5.14. Moving forward, we need to test more diplexer chips and add more wirebonds from the chip ground plane to the housing ground.

5.3.4 One-Kelvin measurements

The one-Kelvin measurements were carried out at JPL in Dr. Peter Day's laboratory with the help of Caltech graduate student Ryan Stephenson and ASU graduate student Sasha Sypkens and supervised by Dr. Day. The device measured in this section was designed to yield gain at very low frequencies.

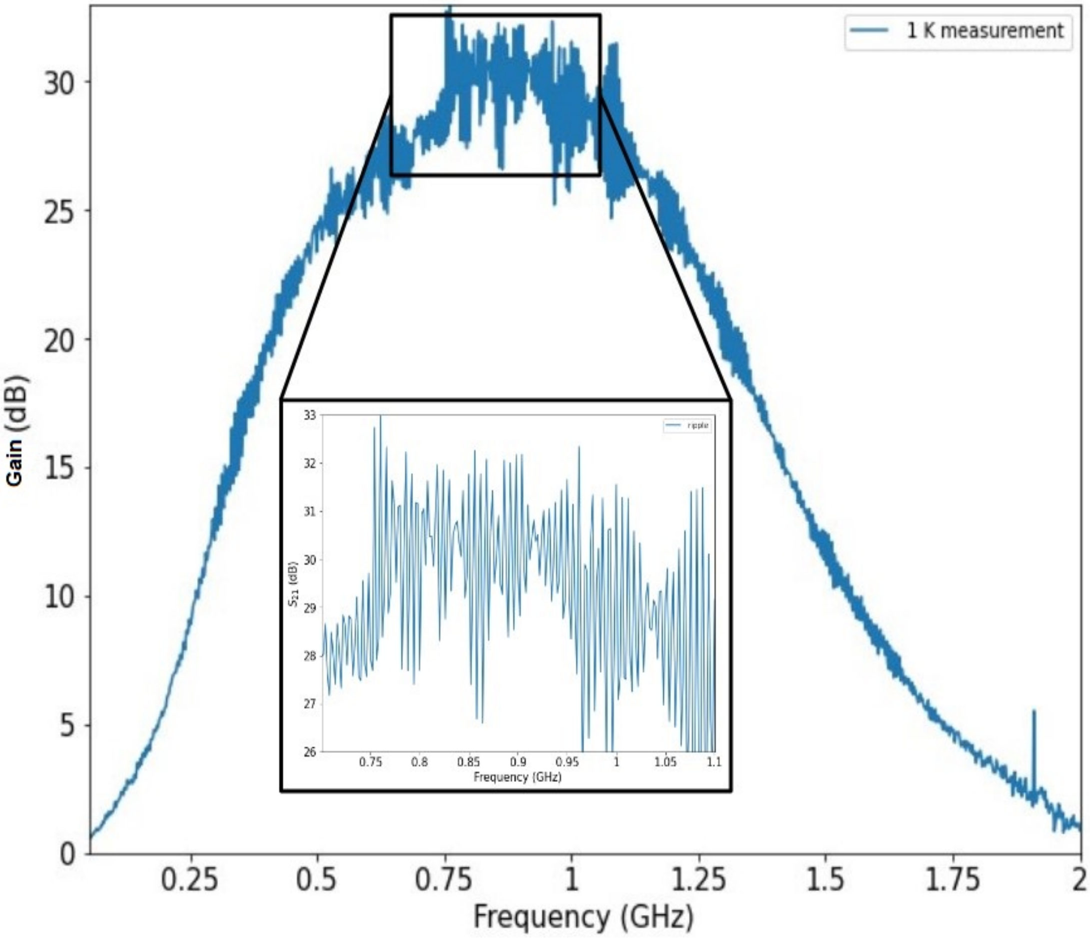

Figure 5.15: The Measured Gain of a Low-Frequency KI-TWPA After Dividing by the Pump-off Measurement at 1K. The Inset Shows a Zoomed-in View of the Gain with a Very Low Gain Ripple.

From the gain plot shown in Fig. 5.15 we see a maximum gain of 30 dB. The inset of Fig.5.15 shows a zoomed-in view of the gain plot at its highest gain with relatively low gain ripples of 1 - 3 dB.

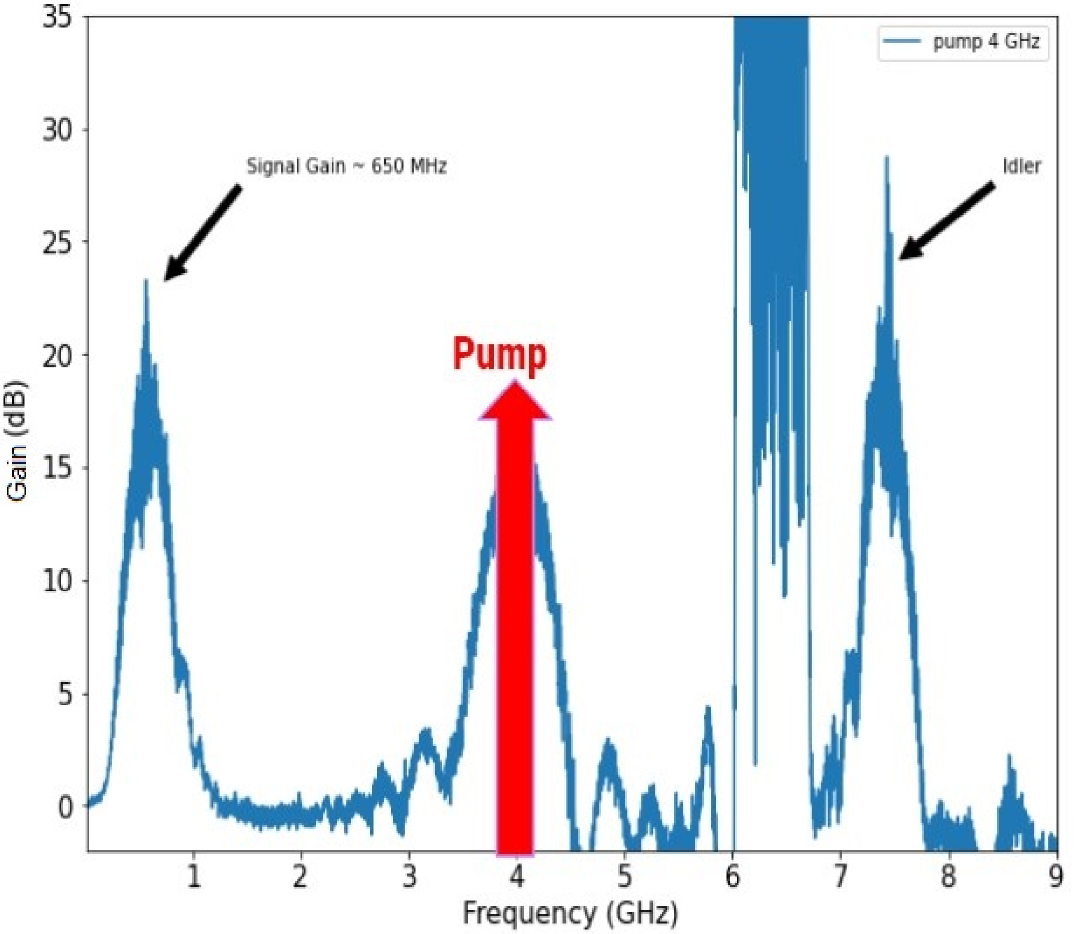

Figure 5.16: Plot of the Measured Gain with Locations of the Signal, Idler, and Pump Tones Depicted. The Pump Tone for this Measurement was Set to 4 GHz.

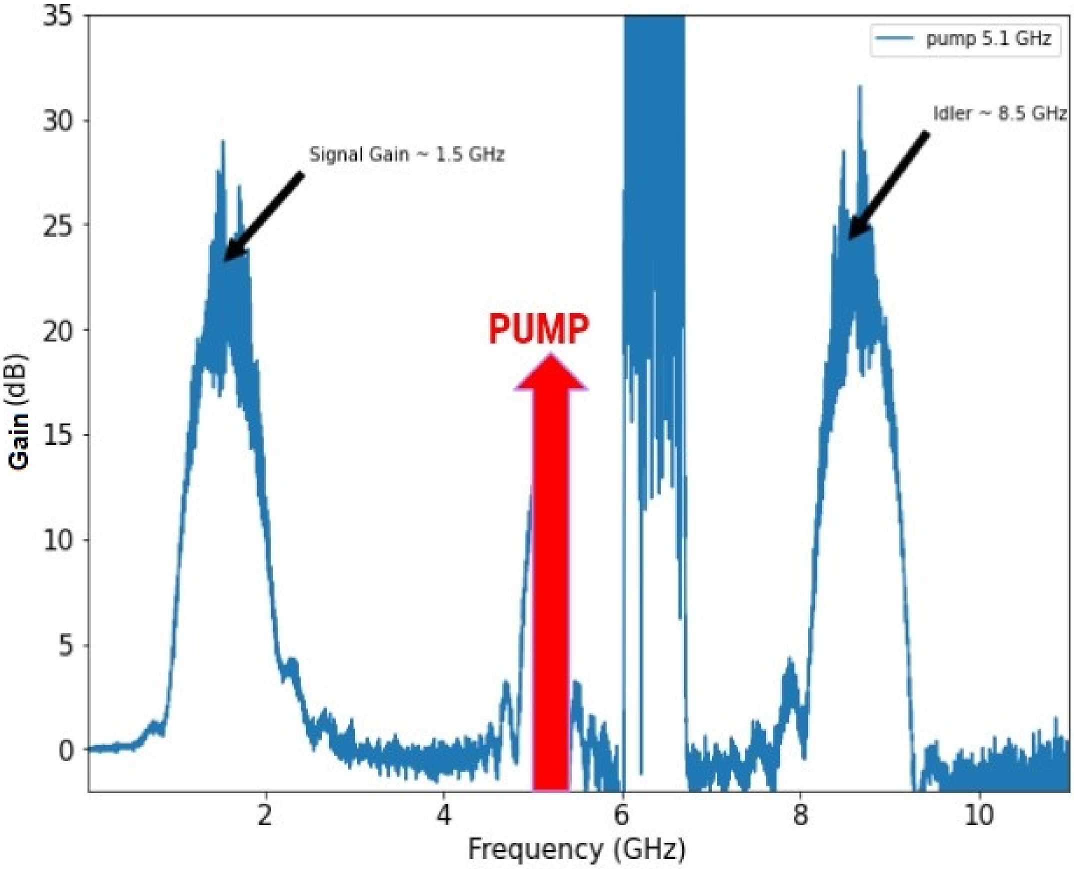

Figure 5.17: Plot of the Measured Gain with Locations of the Signal, Idler, and Pump Tones Depicted. The Pump Tone for this Measurement was Set to 5.1 GHz.

Figures 5.16 and 5.17 show measurements of the gain with pump tones set to 4 GHz in Fig.5.17 and 5.1 GHz for Fig. 5.17. These measurements show the frequency translating gain property explained in section 5.3.2.

5.4 W-band KI-TWPA

The W-band KI-TWPA devices were also made of NbTiN thin films but on a 100-um silicon substrate to minimize box modes in the device and maximize optical coupling to the antenna probes. The width of the microstrip line and the shunted stubs is 250 nm. The housing is made of copper, incorporating the input-output waveguides and backshorts (Fig. 5.18).

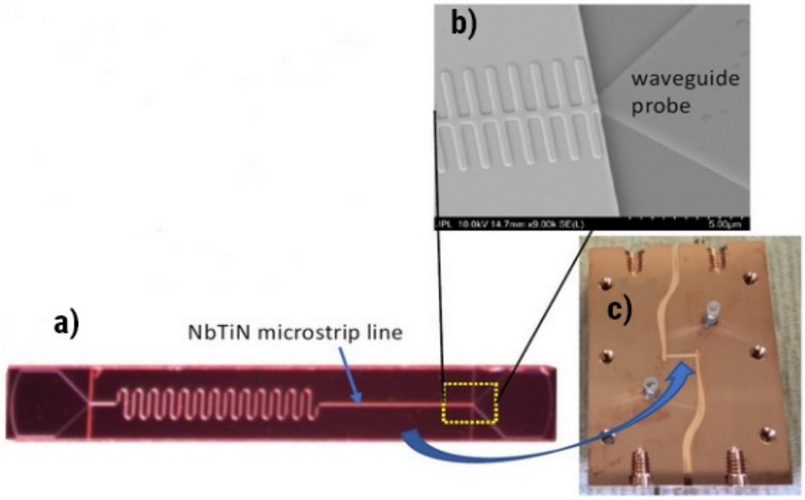

Figure 5.18: W-band Paramp Chip and Housing. a) NbTiN Microstrip Line W-band KI-TWPA Chip. b) SEM Micrograph of the Microstrip Line with Open Stubs and the Radial Probe. c) Picture of Copper Waveguide Housing.

The input signal was generated from a VNA extender and passed through a fixed 20 dB attenuator and then directed to a mechanical variable attenuator. The pump tone was generated using a 1 kHz - 40 GHz Rhode & Schwartz signal generator, and then a passive ×3 multiplier was used to multiply the signal to a higher frequency. After the frequency multiplier, we use another mechanical variable attenuator to adjust the pump tone power. The pump tone and the signal from the VNA are combined using a magic tee (3 dB hybrid coupler) and directed into cryostat into a 20 dB attenuator and finally to the paramp sitting at 4 Kelvin. A full band isolator is placed after the paramp at the 4 K stages.

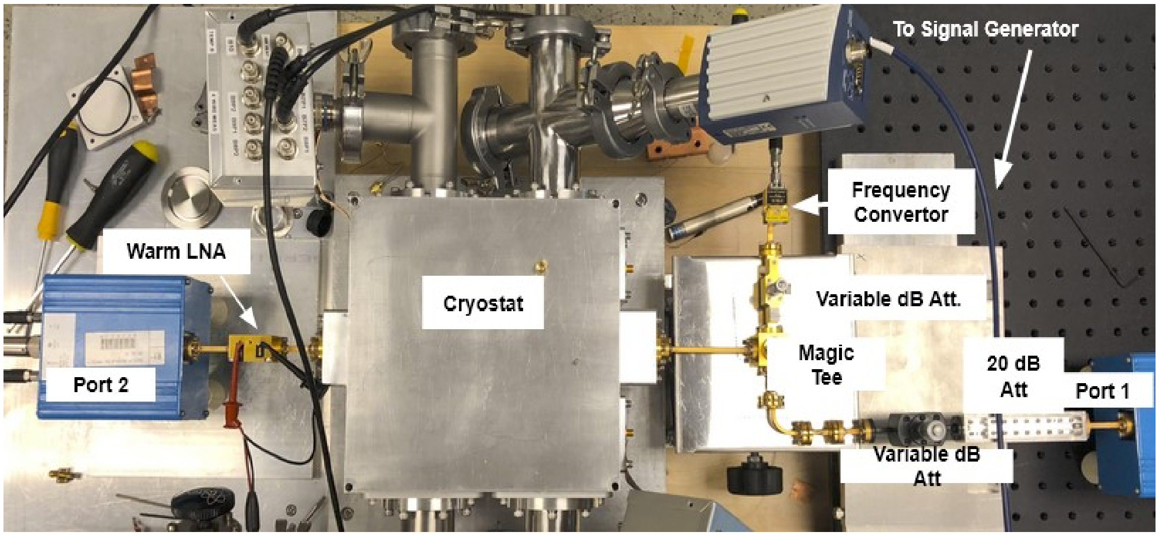

Figure 5.19: Picture of the Cryogenic Test Setup with the Room Temperature Waveguide Components.

The amplified signal is then directed out of the cryostat and further amplified using a room-temperature W-band low-noise amplifier (LNA). The signal then goes back to the VNA via the extender. Before putting the KI-TWPA in the cryostat, we used a waveguide section instead of the paramp to measure the insertion loss of the whole setup. The blue curve in Fig. 5.20 shows the measured S_{21} on a waveguide section, and the orange curve is the measure S_{21} of the paramp.

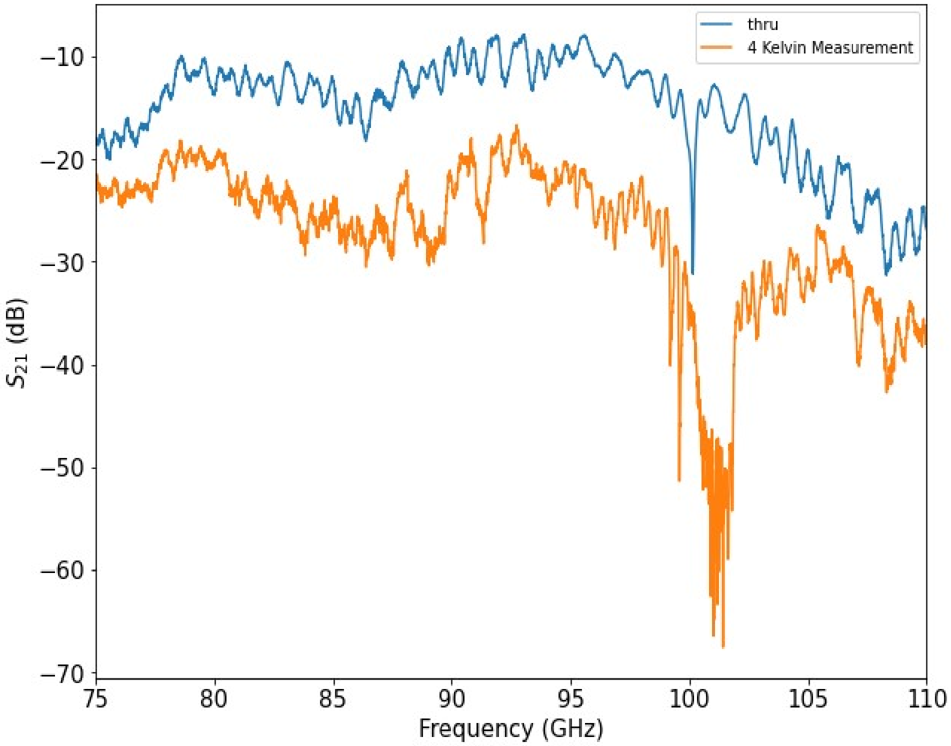

Figure 5.20: Measured S_{21} of the Waveguide Section (Blue) Compared to the Measured S_{21} of the W-band KI-TWPA with the Pump Off. The Lower Transmission of The KI-TWPA/housing System Indicates Loss Either Due to Optical Coupling or in the Transmission Line.

The difference between these two measurements can be attributed to two possible issues (1) the loss in the superconductor due to the relatively high temperature and (2) poor optical coupling due to lack of air channel (or a trench), which can dissipate energy in unwanted modes of the box-substrate structure under the paramp chip.

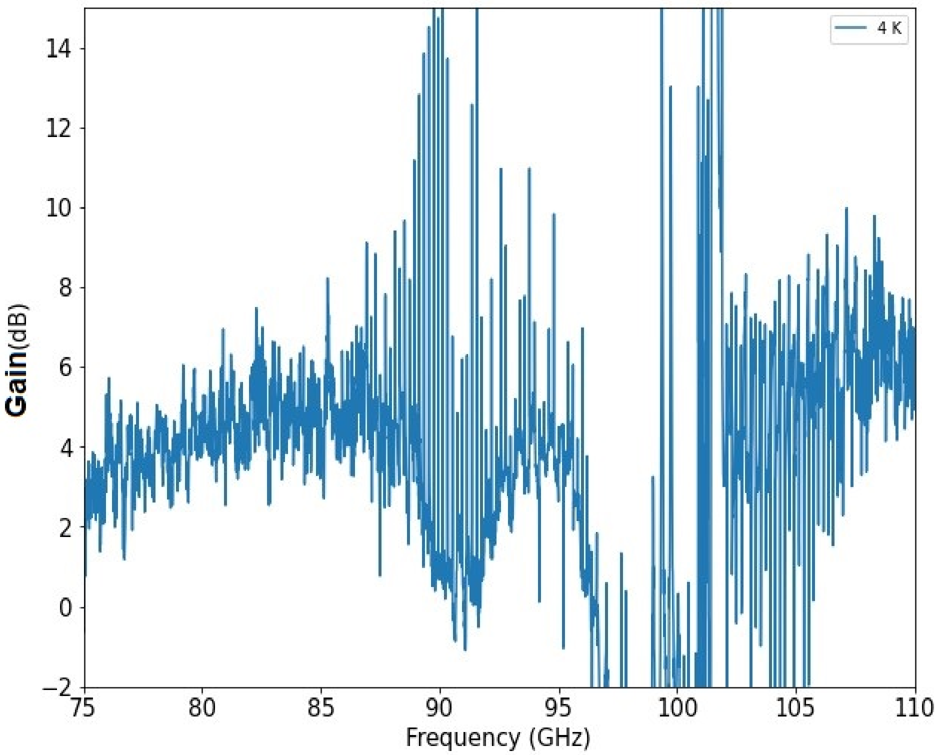

Figure 5.21: Plot of Measured Gain with Pump Tone Frequency of 95.61 GHz and Output Power of 17 dBm at the Signal Generator. We See a Wideband Gain Between 4-6 dB in the 75 - 88 GHz.

To find the optimal gain, a range of pump tone frequencies below the bandgap were swept with different pump tones, and the best results are shown in figures 5.21 and 5.22. We see a wideband gain of between 4-6 dB in the 75 - 88 GHz in Fig. 5.21 and in Fig.5.22 we see a narrow band gain of 6 dB from 75-78 GHz, and a wider band gain of around 5 dB from 80 - 85 GHz.

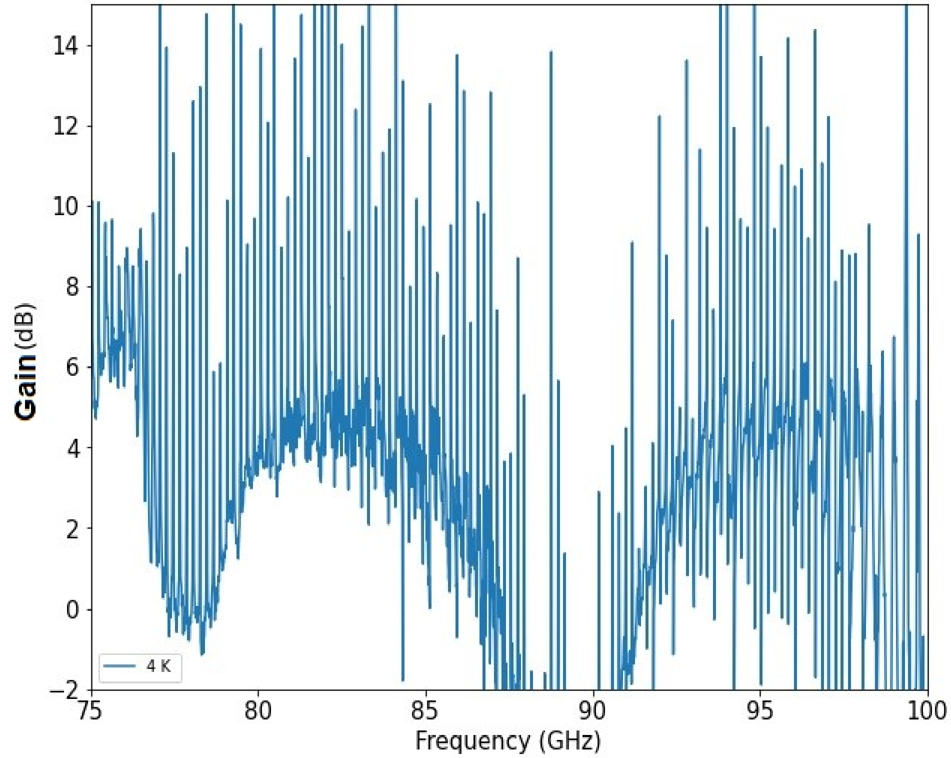

Figure 5.22: Plot of Measured Gain with Pump Tone Frequency of 89 GHz and Output Power of 17 dBm at the Signal Generator. The Oscillations Seen in the Plot are More Likely Due to Impedance Mismatch.

Chapter 6

KINETIC INDUCTANCE QUBIT

6.1 W-band Resonators

6.1.1 Introduction

Characterizing and understanding the superconducting material properties such as kinetic inductance and critical current, in addition to the loss tangent of dielectrics and Two-State States (TSS) noise (Chamberlin *et al.* (2021)), are essential for circuit design in the millimeter-wave region. For superconducting resonators, pushing into the millimeter wave regime, for example, the W-band (75-110 GHz) range, is relatively new and so characterizing materials at that frequency is the first step toward making superconducting W-band devices. We chose to characterize and work with NbTiN due to its relatively high T_c of 16 K, which complements the high-frequency range we aim for.

6.1.2 Resonator Design

The design of the resonators was done by Dr. Peter Day and fabricated by Dr. Henry LeDuc at Micro Devices Laboratory (MDL) at JPL. The design consists of E-plane antenna probes, a microstrip transmission line, and hair clip-shaped resonators. The resonators are capacitively coupled to the transmission line by proximity. The fabrication stack is made of 100 μm of a silicon substrate, 35 nm of NbTiN layer, 5 μm of amorphous silicon (a-Si) and a 150 nm of NbTiN as the ground plane as shown in Fig. 6.1.

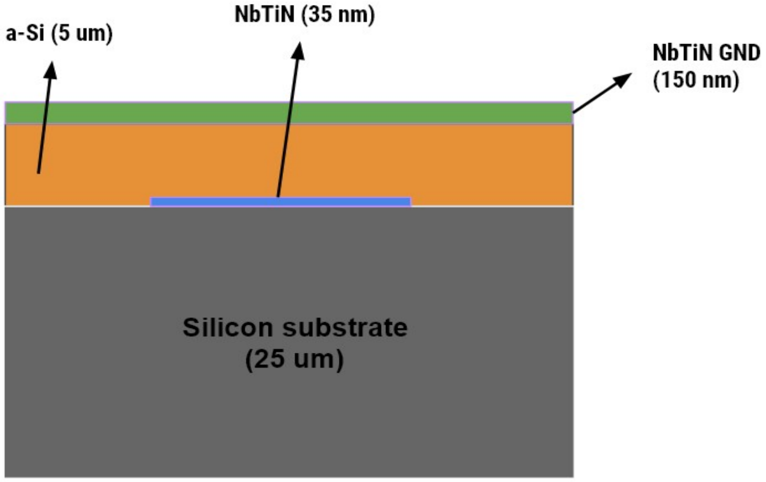

Figure 6.1: This Picture Shows the Fabrication Stack of the W-band Resonators Coupled to a Transmission Line (Not to Scale).

The ground plane is interrupted over the radial probes to allow for the coupling of the W-band signal.

The length of the resonators is chosen to set the resonant frequencies, and a total of nine resonators were designed. The mask layout of the resonator circuit is shown in Fig. 6.2

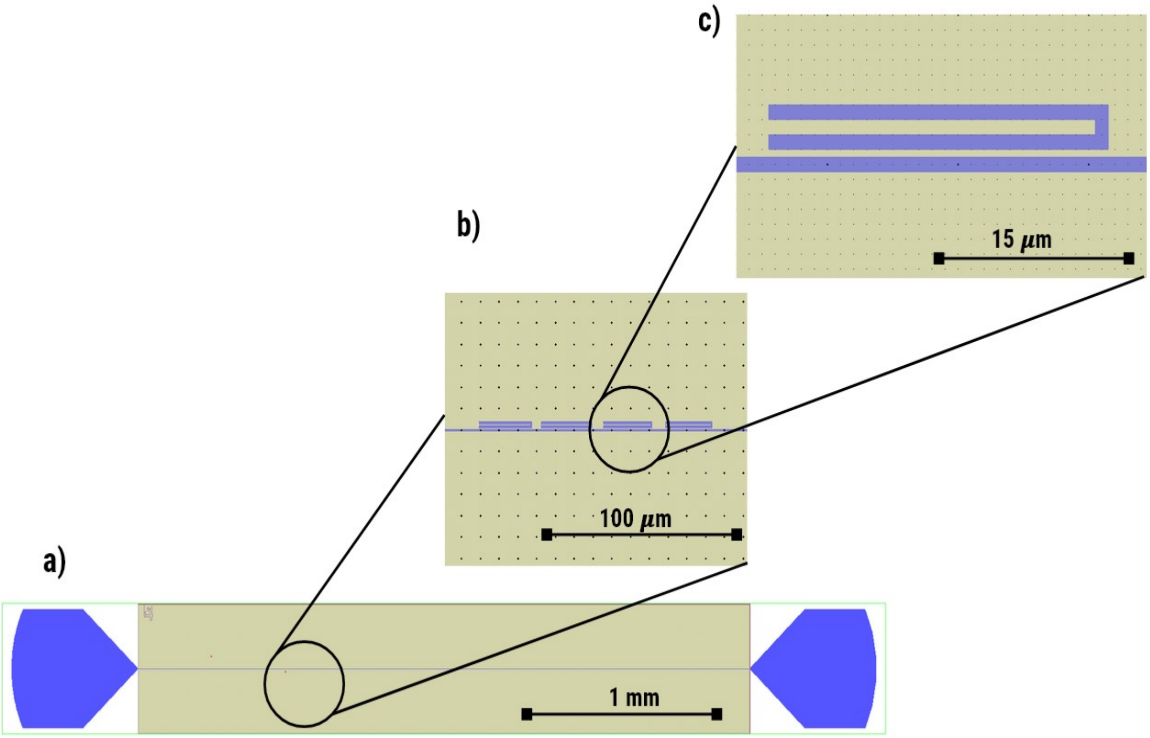

Figure 6.2: a) Drawing of the Full Size of the Chip with Two Radial Probes on Either End, and the Gold Color Shows the Ground Plane. b) a Close-up View of Resonators Next to the Transmission Line. c) Single Resonator Coupled to a Microstrip Transmission Line.

The chip sits in a copper housing (Fig. 6.3) with a backshort below the probes and a channel height design to maximize the coupling between the waveguide and the radial probe as described in Kooi *et al.* (2003).

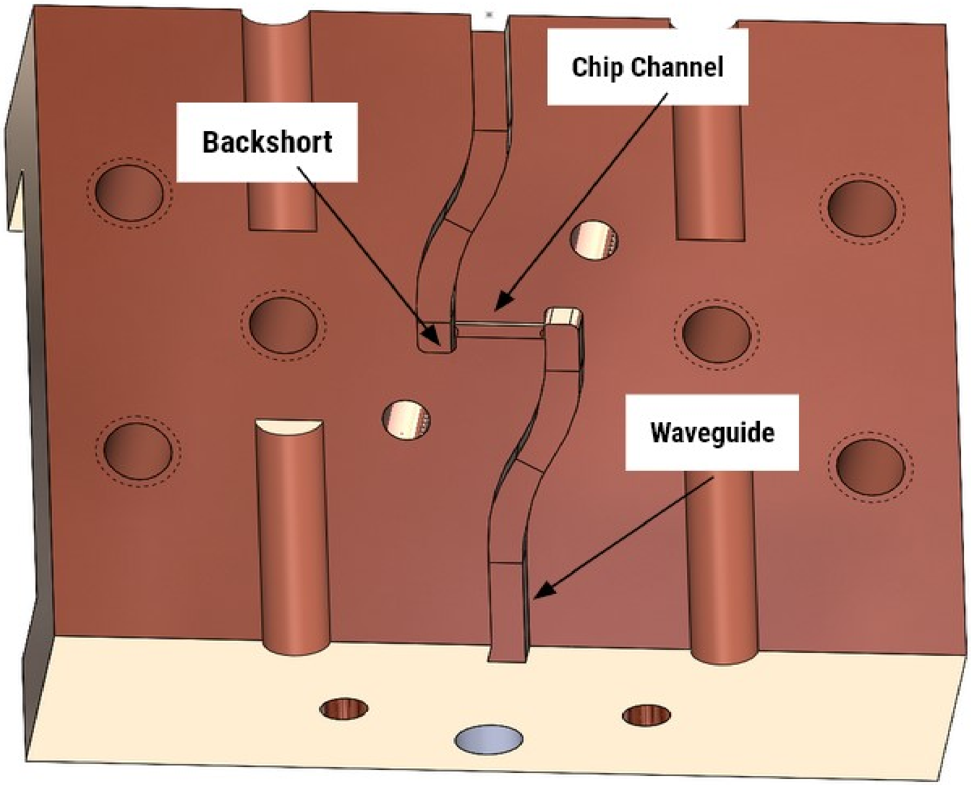

Figure 6.3: SolidWorks Picture of the W-band Housing Used for the W-band Resonators Cryogenic Measurements.

There is an additional cut-out to avoid unwanted shorts between the waveguide housing and the probes.

6.1.3 *Test setup and Measurements*

The cryogenic measurements were done in Dr. Peter Day's laboratory at JPL and with the help of Caltech graduate student Ryan Stephenson. The measurements were taken at 1 K with the W-band resonator housing mounted to the He^4 sorption fridge as shown in Fig. 6.4.

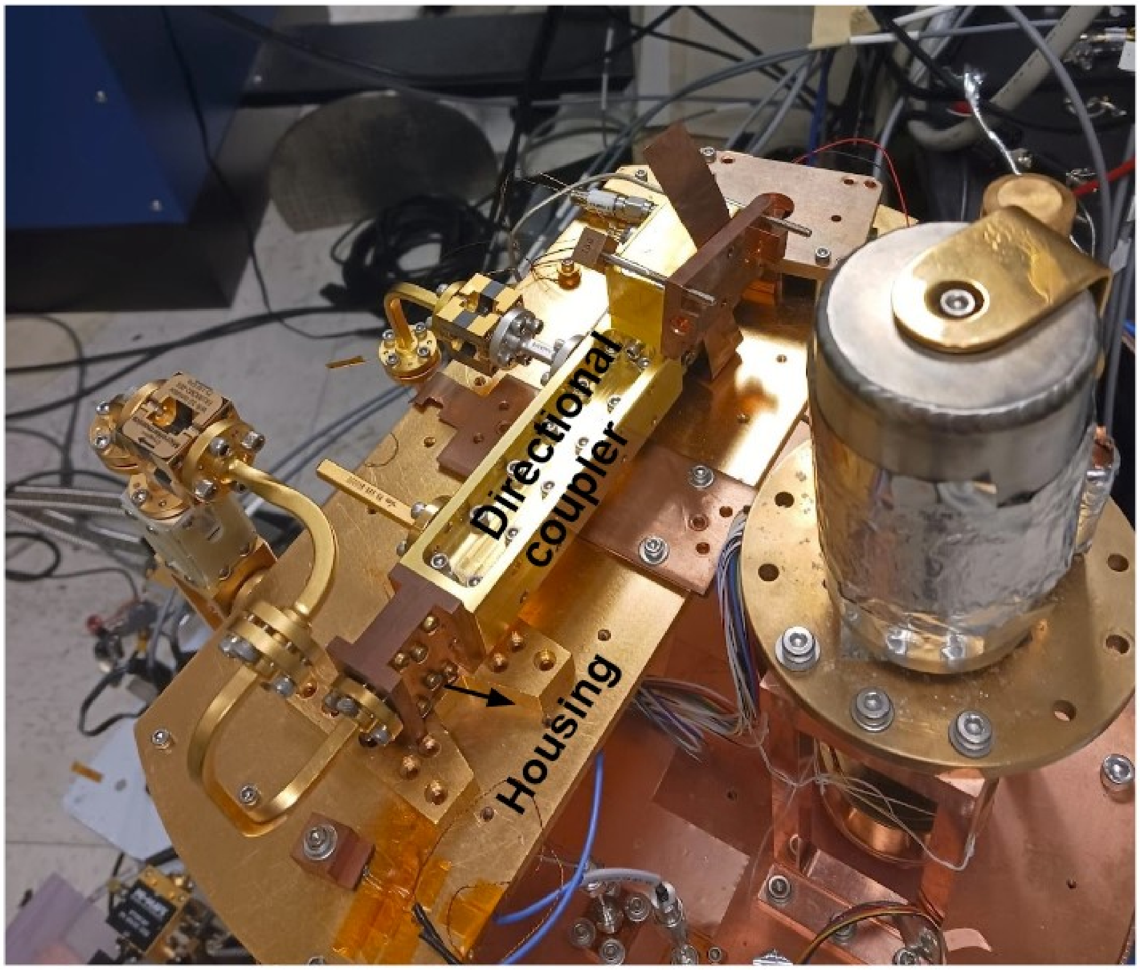

Figure 6.4: Shows the 1K Stage of the Cryostat with the Copper Housing of the W-band Resonators Connected to the Gold-Plated Waveguides and a Directional Coupler.

We used a Vector Network Analyser (VNA) with frequency extenders to sweep in the 75 - 110 GHz frequency range. We used a programmable W-band attenuator at the input of the frequency extender to set the readout power. A series of waveguides were used to go from the attenuator to the cryostat. We also used W-band thermal breaks and stainless steel waveguides between each cryogenic stage to reduce thermal conduction between the stages. Two full-band cryogenic isolators were used before and after the W-band resonator housing. In addition, a W-band cryogenic amplifier and a W-band room temperature amplifier were used at the output of the measurement setup to amplify the signal. Fig. 6.1.3 shows the circuit diagram of the measurement setup next to the actual picture of the cryostat.

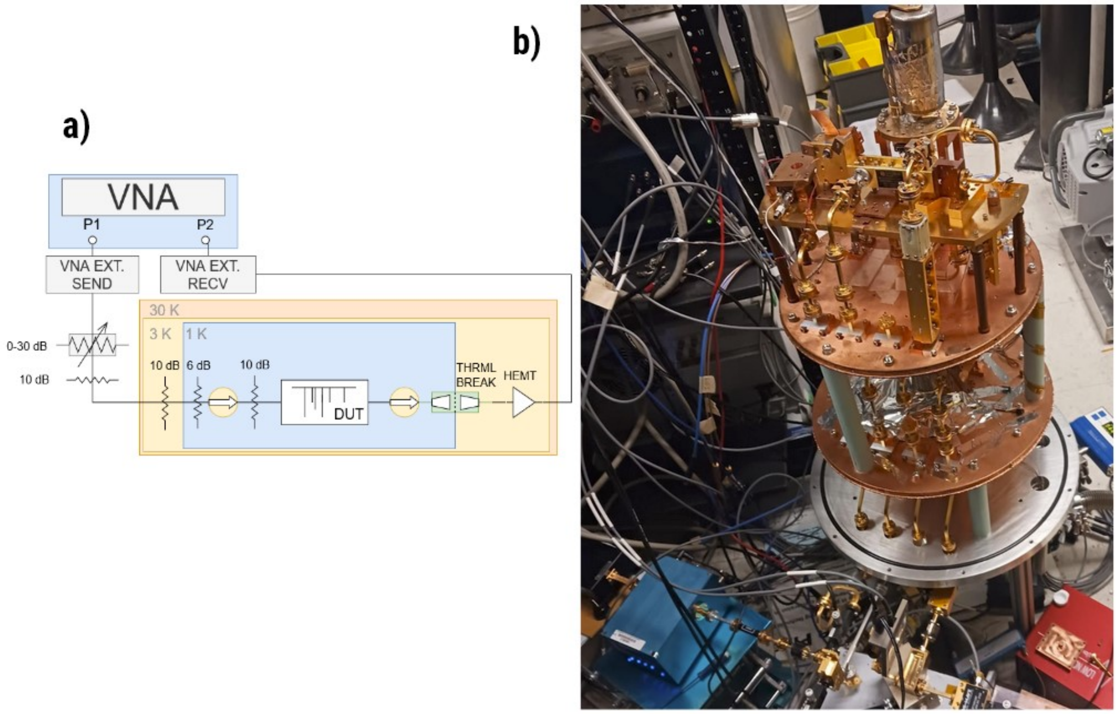

Figure 6.5: a) The Circuit Diagram of the Measurement Setup. b) Shows a Picture of the Cryostat with the Circuit Elements Depicted in the Circuit Drawing.

The first measurement we made was to compare the transmission through the housing, probes, and the microstrip line with a previously made measurement of a waveguide section that was replaced with housing. As we can see in Fig. 6.6, the measured transmission of the device compared to that of a waveguide section is very similar. This tells us that the probes designed have very high coupling efficiencies.

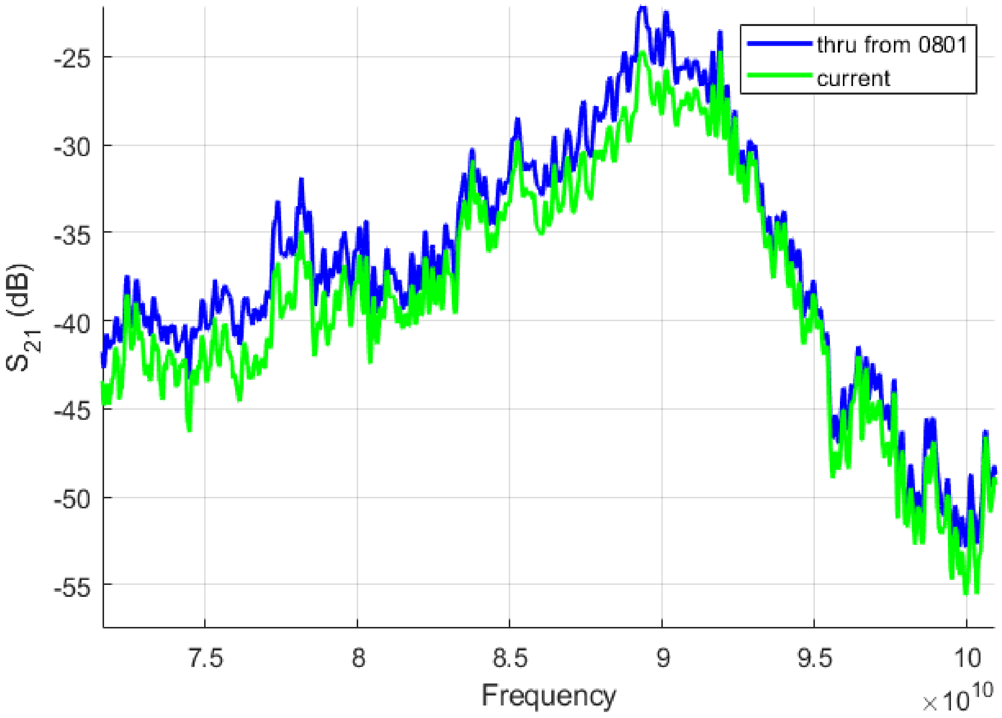

Figure 6.6: *Blue* is the Measured S_{21} of a Waveguide Section Placed Instead of the Resonator Housing System in the Prior Cooldown. *Green* is the S_{21} measurement of the housing-microstrip.

We then looked for the resonances and found four working resonators in the 75 - 110 GHz frequency range. Fig. 6.7 shows the measurement of the in-phase and quadrature of the voltage and transmission magnitude and unwrapped phase as a function of the frequency of a resonator with input power of -60 dBm at the device at 900 mK.

The extracted internal quality factor from the fit for this resonator is $\sim$ 53000, and the coupling quality factor is $\sim$ 49000. The following table shows some of the extracted parameters from the fit of the resonators data using the open-source python package called Scraps (SuperConducting Resonator Analysis and Plotting Software) developed by Carter *et al.* (2017).

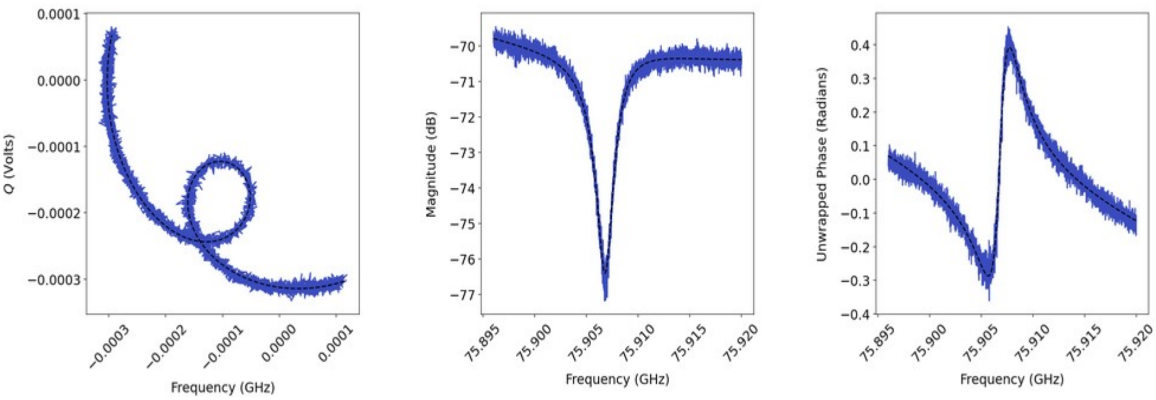

Figure 6.7: *Left,* the Fit and Data of In-Phase-Quadrature (IQ) of a Resonator with the Resonant Frequency of 75.9 GHz. The IQ Circle is Due to the Resonator. *Middle,* Magnitude of S_{21} of a Measured Resonator as a Function of Frequency. *Right,* Unwrapped Phase of a Measured Resonator as a Function of Frequency.

Resonator name	Res. Freq. f_0 (GHz)	Internal Q_i	Coupling Q_c
RES-1	75.90	69156	49857.44
RES-2	82.246	47664.2	43784.03
RES-3	101.23	47886.7	50696.17
RES-4	103.20	38703	78844.01

Table 6.1: Table of Measured Resonators with Their Resonant Frequencies and Internal and Coupling Quality Factors.

The power response measurements of the resonators were taken by adjusting the output of the variable attenuator. We then did a frequency measurement sweep of each resonator. Fig. 6.8 the power response of the RES-2 with power values being the relative power at the output of the programmable attenuator.

As we can see from Fig. 6.8, by increasing the input power of the resonator, we drive it into the non-linear regime, and at around -15 dBm, we start to saturate the resonator. Therefore, we can observe the bifurcation of the resonator.

The transfer function of the resonator in the low power limit is given by

$$S_{21}(\omega) = 1 - \frac{Q_r Q_c^{-1}}{1 + 2iQ_r x}, \tag{6.1}$$

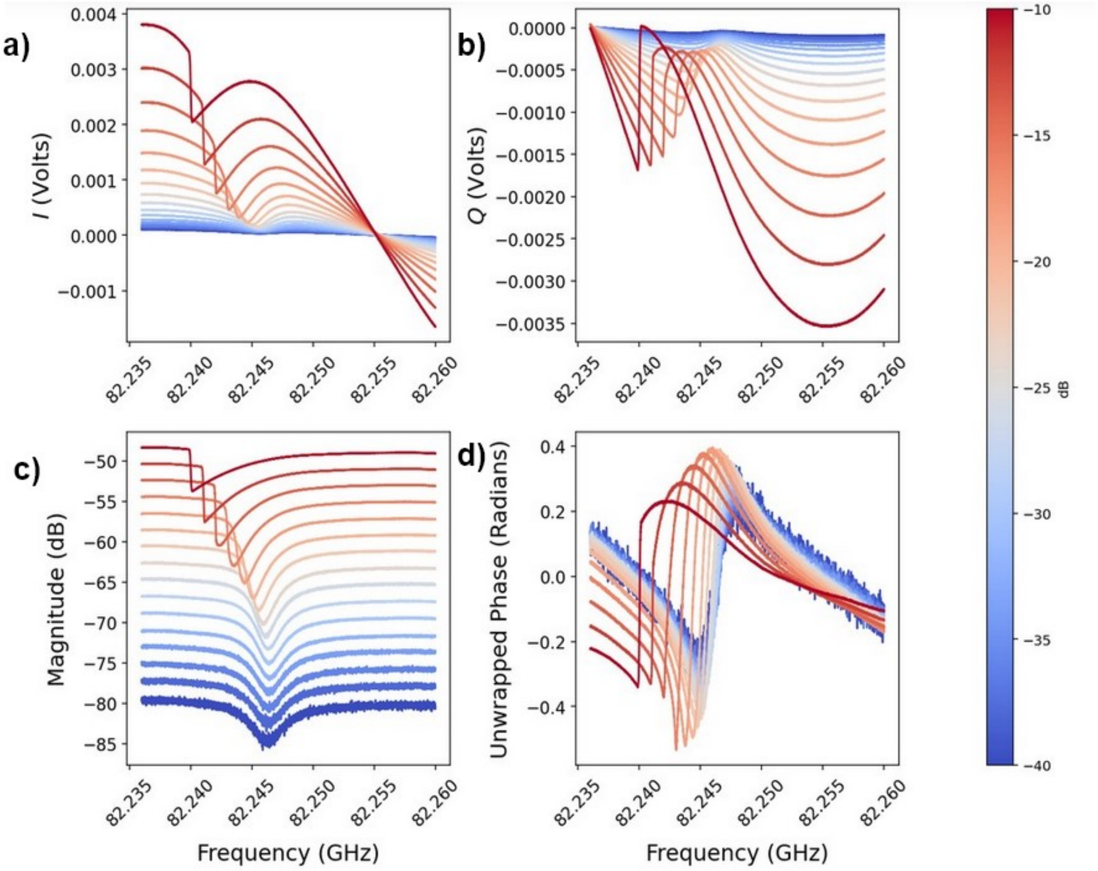

Figure 6.8: a) Plot of the Real Part (In-phase) of the Transmission as a Function of Frequency for Different Power Levels at the Output of the Programmable Attenuator Ranging from -40 dB to -10 dB. b) Plot of the Imaginary Part (Quadrature) of the Transmission as a Function of Frequency. c) Plot of Transmission in dB of the Resonator as a Function of Frequency. d) Plot of the Resonator's Unwrapped Phase as a Frequency Function.

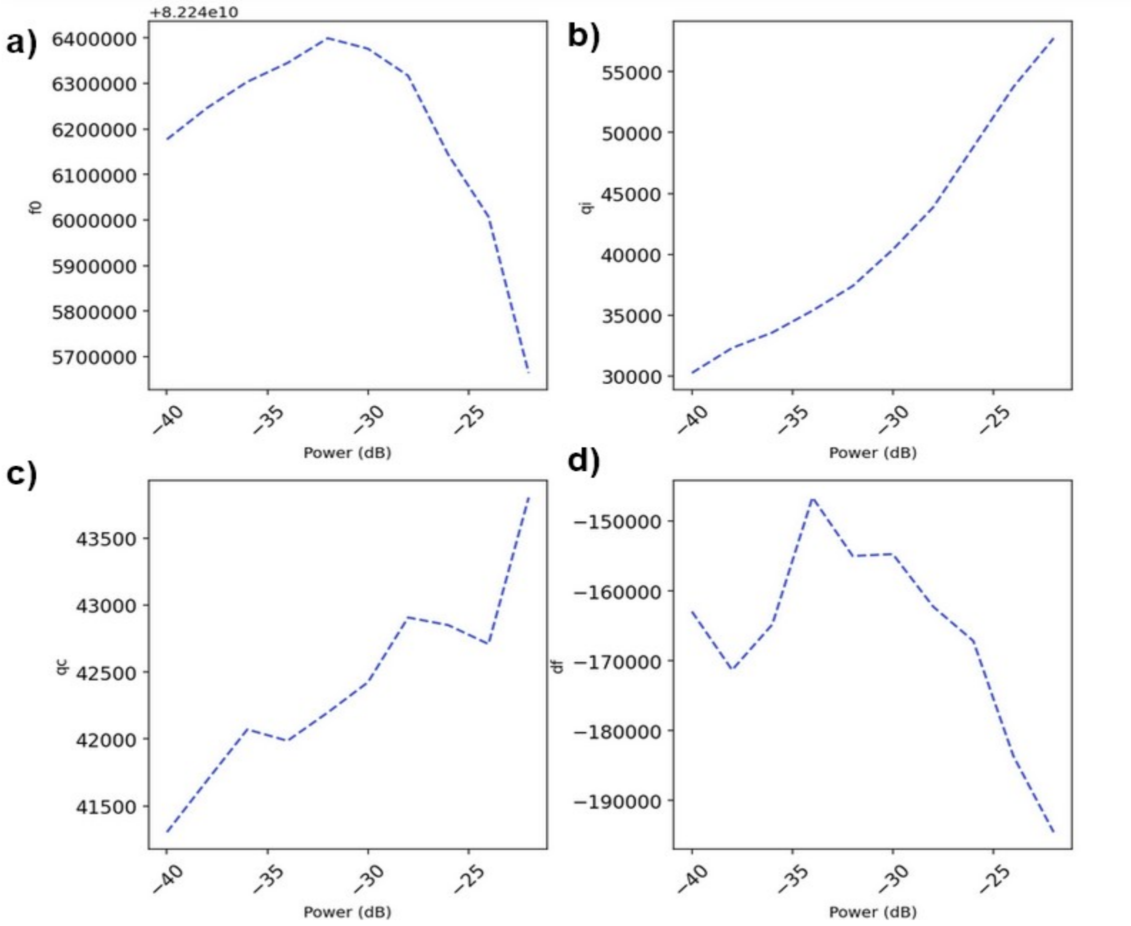

Figure 6.9: All Plots Are as a Function of Readout Power. a) Plot of the Resonant Frequency. b) Plot of the Internal Quality Factor of the Resonator. c) Plot of the Coupling Quality Factor of the Resonator to the Transmission Line. d) Change in Resonant Frequency.

where Q_r is the total quality factor of the resonator, and it is related to the coupling quality factor by

$$\frac{1}{Q_r} = \frac{1}{Q_i} + \frac{1}{Q_c}. \tag{6.2}$$

Q_i is the resonator's intrinsic or internal quality factor. The detuning frequency x is defined as follows:

$$x = \frac{\omega - \omega_r}{\omega_r}, \tag{6.3}$$

where ω_r is the resonant frequency of the resonator.

For a non-linear resonator, the shift in the resonant frequency is given by

$$\omega_r = \omega_r(0) + \delta\omega \tag{6.4}$$

where $\omega_r(0)$ is the resonant frequency in the low readout power limit, and $\delta\omega$ is the shift in resonant frequency due to the application of power. Following Swenson *et al.* (2013) the detuning is calculated

$$x \approx x(0) - \delta x, \tag{6.5}$$

where $x(0) = \omega - \omega_r(0)/\omega_r(0)$. δx is given by

$$\delta x = -\frac{E}{E_*} \tag{6.6}$$

where E is the energy stored in the resonator and E_* is the energy that sets the scale of the non-linearity, and it is on the order of the condensation energy (Zmuidzinas (2012)). The power absorbed in the resonator in terms of drive power at the device is given by Swenson *et al.* (2013) and, it is

$$P_{abs} = P_d \left[\frac{2Q_r^2}{Q_i Q_c} \frac{1}{1 + 4Q_r^2 x^2} \right] \tag{6.7}$$

where P_d is the drive power at the device. Using the internal quality factor of the resonator, we can calculate the energy stored in the resonator.

$$E = \frac{2Q_r^2}{Q_c} \frac{P_d}{\omega_r} \frac{1}{1 + 4Q_r^2 x^2} \tag{6.8}$$

substituting Equation (5.8) in Equation (5.6), the detuning term becomes

$$x = x(0) + \frac{a}{1 + 4Q_r^2 x^2}. \tag{6.9}$$

We define the non-linear factor a as

$$a = \frac{2Q_r^3}{Q_c} \frac{P_d}{\omega_r E_*} \tag{6.10}$$

following Swenson *et al.* (2013), we can rewrite Equation (5.9) as

$$y = \frac{a}{1 + 4y^2} + y_0 \tag{6.11}$$

where $y_0 = x_0 Q_r$ and $y = xQ_r$. By solving for y in Equation (5.11) in terms of y_0 and picking the proper root of the polynomial equation according to Swenson *et al.* (2013) we can find x and substitute it in Equation (5.9) and extract the nonlinearity parameter a from the fit as shown in Fig.6.10. The code to fit the nonlinear resonators was developed based on the work in Wandui *et al.* (2020) and Minutolo *et al.* (2019).

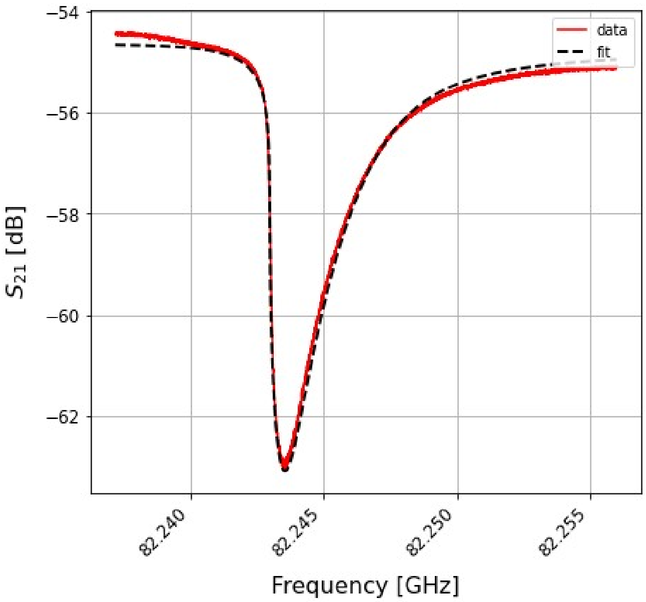

Figure 6.10: Plot of the Measured Response of the Non-Linear Resonator as a Function of Frequency (Solid Red Line) and the Response Fit of the Resonator(Dashed Black Line).

From this fit, we extract the following parameters RES-2 with variable attenuator power set to -16 dBm: $Q_i =$ 69775.4, $Q_c =$ 42059.8 , $\omega_r = 2\pi \times 8.22 \times 10^{10}$ Hz and a = 0.743. Calculating the drive power at the device at the onset of bifurcation, we can estimate E_* when the attenuator power is set to -16 dB. Using the information in Fig. 6.11, we can determine the output power of the extender at 82.2 GHz. Ryan Stephenson carried out this measurement at JPL.

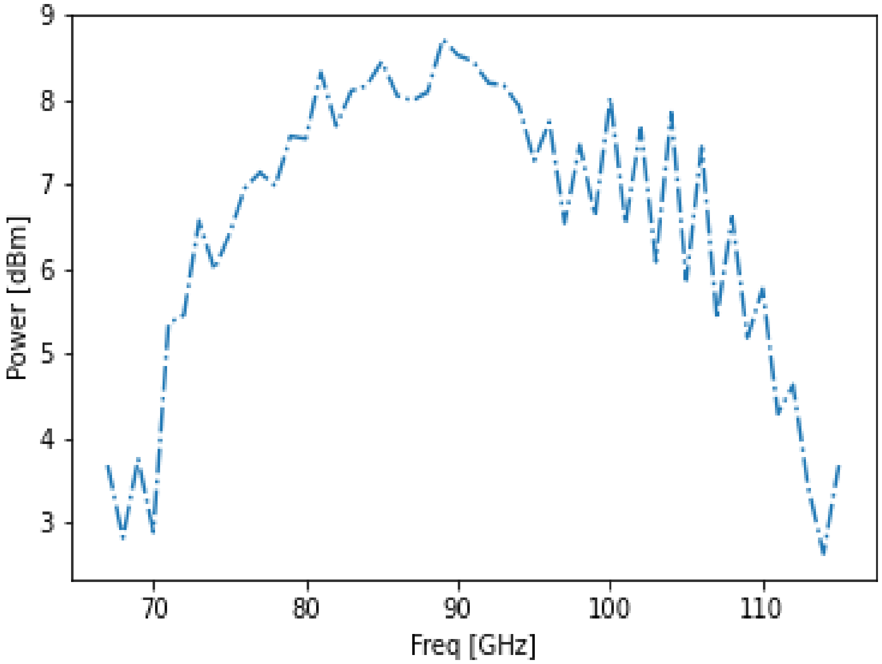

Figure 6.11: Plot of the Measured Output Power (in dBm) of the VNA Extender in the W-band. Courtesy of Ryan Stephenson.

As obtained from the plot above, the output power of the extender at 82.2 GHz is roughly 8 dBm and using the variable and fixed attenuation values, we reach a value of -54 dBm or 3.8 nW. From these values, we calculate E_* to be 9.53×10^{-12} J. The condensation energy is given in Kher (2017)

$$E_p = 2N(0)\Delta_0^2 V \tag{6.12}$$

where $N(0)$ is the single-spin density of states at the Fermi level, Δ_0 is the bandgap energy at absolute zero, approximately 1.76 $k_B T_c$ with T_c being the critical temperature of the superconducting material. V is the volume of the resonator. For the NbTiN resonator of roughly $V \approx 1.785\ \mu\text{m}^3$ with $T_c = 14$ K and $N(0) \approx 2.75 \times 10^{47}$ J^{-1}m^{-3} (Sidorova *et al.* (2021)) is $E_c \approx 8.2 \times 10^{-12}$ J which is close to the value we estimated for E_* from the fit.

To estimate the average number of photons absorbed in the resonator, we need to calculate the power absorbed by the resonator.

$$P_{abs} = P_{input} - P_{ref} - P_{trans}, \tag{6.13}$$

in which P_{input} is the input power, P_{ref} is the reflected power and P_{trans} is the transmitted power. Following Bruno *et al.* (2015), we get

$$P_{abs} = \frac{2Q_r^2}{Q_c Q_i} P_{input} \tag{6.14}$$

The energy stored in a harmonic oscillator is $\langle n \rangle \hbar\omega_r$. We can calculate the average number of photons using the input power as follows

$$P_{abs} = \langle E \rangle \Gamma, \tag{6.15}$$

where Γ is the resonator's bandwidth and can be written in terms of internal quality factor and resonant frequency: $\Gamma = \frac{\omega_r}{Q_i}$. Combining Eq.5.13 and Eq.5.14, we get

$$\langle n \rangle = \frac{2Q_r^2 \, P_{input}}{\hbar \, \omega_r^2 \, Q_c}. \tag{6.16}$$

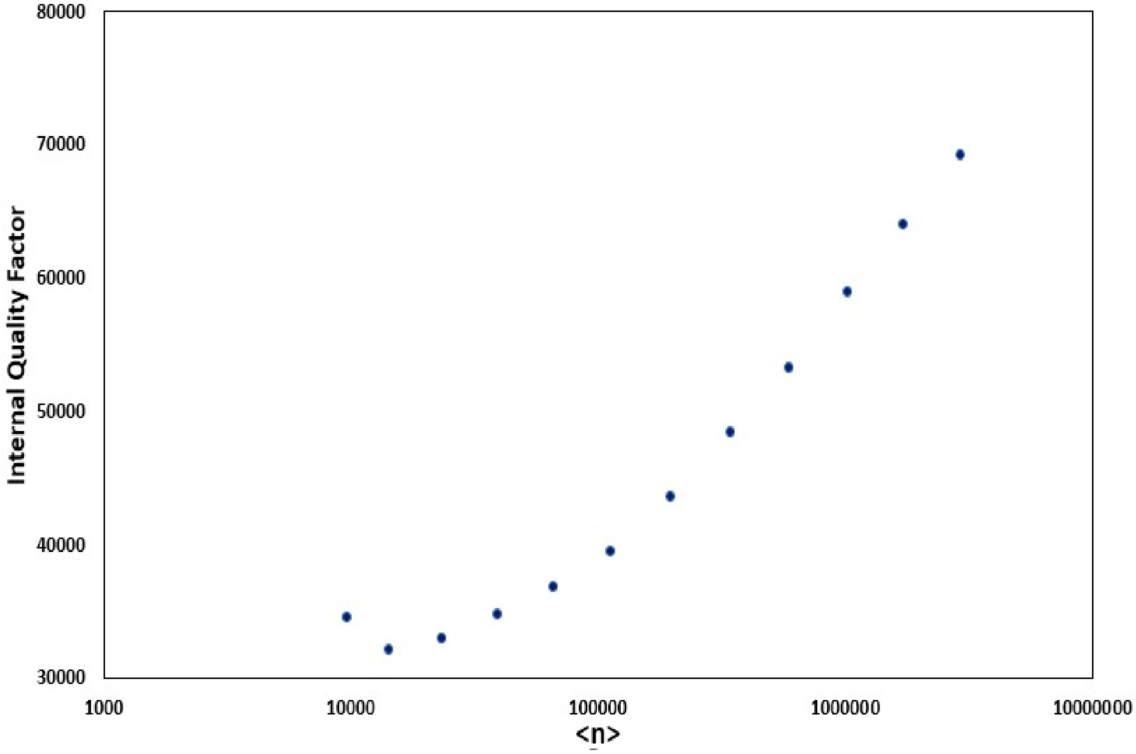

Figure 6.12: Plot of the Internal Quality Factor of a Resonator as a Function of the Average Photon Number Absorbed by the Resonator.

Fig. 6.12 shows that the average photon number in the resonator at -40 dB of applied power from the attenuator is $\sim$ 10,000. We are not in the single photon limit, and to reach that regime, we need to apply around -82 dBm of power after the input of the VNA extender.

6.2 A mm-Wave Kinetic Inductance Qubit (Kineticon)

6.2.1 Introduction

Superconducting qubits are one of the leading platforms for building quantum computers. Recently, quantum supremacy, in which a quantum computer performs an infeasible computation on a classical computer, was demonstrated using 53 superconducting qubits (Arute (2019)). Several academic institutions and companies (IBM, Rigetti, QuTech, and Amazon) offer cloud quantum computing services based on superconducting transmon qubits. These devices, operating in the 4-10 GHz band, utilize Josephson junctions formed by an aluminum oxide layer between aluminum contacts. Scaling up these early quantum computers to the thousands or millions of physical qubits needed to realize quantum error correction (National Academies of Sciences (2018) report) faces several significant hurdles, including limited coherence (10-100 T_2^* is typical), lack of room temperature interconnects, and the large physical size of superconducting qubits (typical qubits have 0.1-1 mm lateral dimensions). The standard aluminum or niobium Josephson tunnel junction is becoming a bottleneck to increasing qubit coherence and yield requirements:

- spurious two-state systems (TSS) cause decoherence Klimov *et al.* (2018); Burnett *et al.* (2019); Schlör *et al.* (2019); Chamberlin *et al.* (2021)
- imprecision in qubit frequencies reduces yield for fixed frequency qubit architectures Chamberland *et al.* (2020)
- Quasiparticles cause charge parity fluctuations and heating Serniak *et al.* (2018)

Superconducting kinetic inductance qubits operating in the W-band (75-110 GHz) have the potential to lift these bottlenecks. The nonlinear inductance of superconducting nanowires has been used in experiments involving cavity-based parametric amplifiers Vijay *et al.* (2009); Levenson-Falk *et al.* (2011) and qubits Winkel *et al.* (2020); Schön *et al.* (2020); Kerman (2010) in the sub-10 GHz regime and a parametric amplifier in the W-band Anferov *et al.* (2020b). Thus far, a viable superconducting qubit has not been demonstrated in the W-band.

In particular, exploration of high-frequency qubits is encouraged because they have the potential to solve problems with state-of-the-art transmon qubits. To achieve the highest coherence times, IBM uses fixed-frequency transmons and an all-microwave operation to entangle pairs of qubits together (the cross resonance gate). However, the speed and performance of the cross resonance gate depend heavily on the exact frequency allocation between the qubits Chamberland *et al.* (2020) and spectator qubits Takita *et al.* (2016). Fabricating the nonlinear inductive part of the qubit from well-defined lithographic processes of non-linear kinetic superconductors instead of amorphous growth of an aluminum oxide layer in the Josephson junction could allow repeatable frequency allocation between qubits. Also, operating at a higher frequency allows us to scale the systems down in size as we look to scale to ever larger numbers of qubits.

The construction of a quantum computer implementing error correction imposes constraints on size, operating frequency, and operating temperature. The computer will require at least thousands of physical qubits, a scale at which the physical size of the circuits residing at milliKelvin temperatures becomes a limitation. This is particularly true for qubits coupled to 3D microwave cavities but also holds for 2D circuits. An interesting possibility is to scale the circuits to a much higher frequency. Millimeter-wave operation requires superconductors with relatively high T_c, which implies a high gap frequency, $2\Delta/h$, beyond which photons break Cooper pairs. For example, NbTiN with $T_c \approx 15\,\mathrm{K}$ Basu Thakur *et al.* (2020) has a gap frequency near 1.4 THz, much higher than that of aluminum (90 GHz), allowing for operation throughout the millimeter-wave band. We introduce the new term Kineticon to refer to qubits that take advantage of the nonlinear response of superconducting wires as opposed to relying on Josephson junctions.

6.2.2 Increasing Operating Frequency of Qubits

Addressing individual states in a qubit requires a large relative anharmonicity, $\alpha = |E_{10} - E_{21}|/E_{10}$, where E_{10} is the transition energy from the ground state to the first excited state and E_{21} is the transition energy from first-excited state to the second-excited state. Here, we derive this expression for the Kineticon qubit and discuss the implications of this requirement.

Increasing both the qubit and readout resonator frequency to W-band ($\sim$ 100 GHz) could allow for the operation of the quantum processor at a higher temperature. While the 90 GHz gap frequency of aluminum represents a barrier for conventional qubit technologies, it may be possible to realize a qubit with a transition frequency in the millimeter band that uses nonlinear kinetic inductance to provide the required anharmonicity. For a Kineticon qubit the relative anharmonicity, α can be written as follows

$$\alpha \approx 3\frac{I_{zpf}^2}{I_*^2} \tag{6.17}$$

where $I_{zpf} = \sqrt{\frac{hf_r}{2L}}$ is the zero-point fluctuation current and I_* is the characteristic current of the nanowire. Factor 3 comes from energy eigenvalue calculations for a nanowire in the weak anharmonic limit. For a Kineticon qubit with $f_r = 100$ GHz, we can plot the relative anharmonicity as functions of the total inductance of the nanowire L and the characteristic current I_*. As we can see from Fig.6.13, lowering both total inductance L and the characteristic current I_* increases the relative anharmonicity. To improve the anharmonicity of a Kineticon qubit, it is possible to control

J_*, and L_s of the nanowire during the fabrication process Aref and Bezryadin (2011); Annunziata *et al.* (2010) in addition to changing its dimensions.

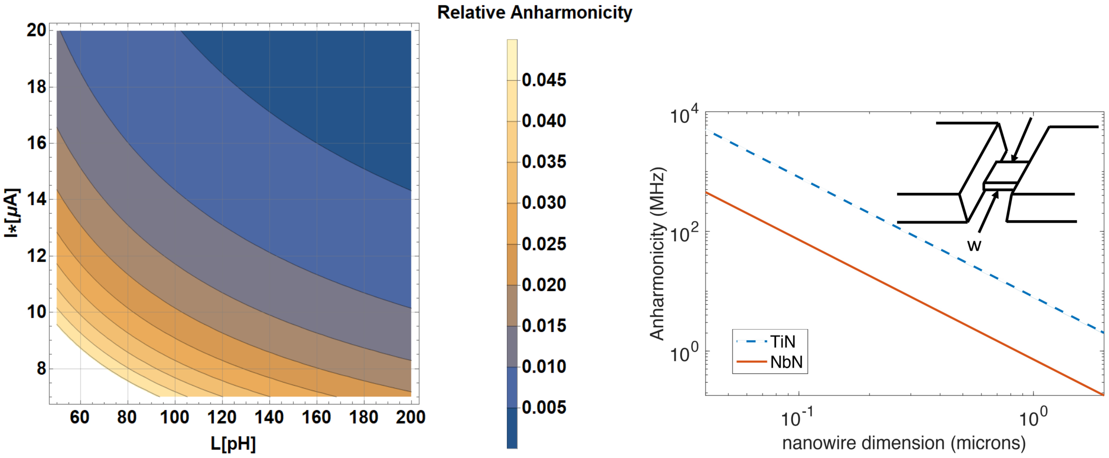

Figure 6.13: *Left:* Contour Plot of the Relative Anharmonicity of a Nanowire Qubit as a Function of total Inductance L and the Characteristic Current I_*. *Right:* Anharmonicity Versus Nanowire Dimension for a 100 GHz Resonator with an Inductance Dominated by an Embedded TiN and NbN Nanowire. The Anharmonicity Increases with Decreasing Nanowire Dimensions and is Larger for TiN than NbN.

We can express I_* of the nanowire in terms of the material parameters using Mattis-Bardeen TheoryMattis and Bardeen (1958b) and following Zmuidzinas (2012) as

$$I_* = J_* wt = \sqrt{\frac{\pi N(0)\Delta^3}{\hbar \rho_n}} wt \tag{6.18}$$

where w and t are the width and thickness of the nanowire, respectively, and ρ_n is the normal state resistivity of the thin film. Using $L_s = \hbar R_s/\pi\Delta$, we can express the relative anharmonicity in terms of the volume, V, of the nanowire:

$$\alpha \approx 3\frac{hf_r}{2N(0)\Delta^2 V}, \tag{6.19}$$

Where f_r is the resonator frequency, $N(0)$ is the density of states at the Fermi level, and Δ is the gap parameter. Here we assume that the nanowire dominates the resonator inductance. The denominator in this expression is the superconducting condensation energy, which may also be expressed in terms of the critical field. Using $N(0) = 8.7 \times 10^9$ eV$^{-1}\mu$ m^{-3} Leduc *et al.* (2010) and $\Delta = 0.5$ meV for a thin TiN film ($T_c = 4.5$ K and gap frequency of $f_{gap} \approx 265$ GHz), $N(0) = 2\times\ 10^{10}$ eV $^{-1}\mu$ m^{-3} and $\Delta = 1.1$ meV Schroeder (2018); Semenov *et al.* (2009) for an NbN thin film, and setting a nanowire thickness to 5 nm and the length and width to be equal, the anharmonicity is shown in Fig. 6.13.

While an absolute anharmonicity comparable to a transmon (~ 200 MHz) may be achieved with dimensions that are more or less straightforward to produce, the question is whether TSS or other loss mechanisms will contribute a loss tangent of ($\sim 10^{-6}$) for this type of qubit, as they do for current state-of-the-art microwave qubits. In that case, to maintain the decay time ratio to read time, the anharmonicity would need to be increased accordingly, requiring increased length or decreased width, so the fabrication becomes more challenging. We need to investigate non-linearity in resonators with embedded nanowires to understand the design requirements better.

6.2.3 Cavity-Qubit Full Quantization and Design

Eventually, this technology will require coupling to other qubits, which can be achieved by embedding the qubit in a three-dimensional cavity. That cavity also could reduce the influence of defects in the thin-film system by increasing the mode volume and reducing the field density Paik *et al.* (2011). We use the Energy-Participation Ratio (EPR) method to quantize the cavity-qubit system as described in Minev *et al.* (2021). We start quantizing the kineticon qubit by writing the Lagrangian for the circuit shown in Fig. 6.14 following the procedure in Vool and Devoret (2017).

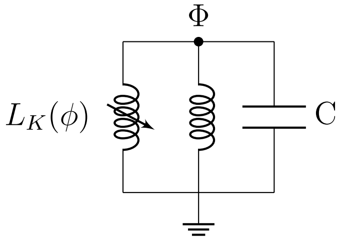

Figure 6.14: Circuit Diagram of an Ideal Superconducting LC Resonator with the Shunted Nonlinear Inductive Element.

Choosing $\{\Phi, \dot{\Phi}\}(=0)$ as the general coordinates the Lagrangian is

$$\mathcal{L} = U_c - U_L = \frac{1}{2}C\dot{\Phi}^2 - \frac{1}{2}\frac{\Phi^2}{L} \tag{6.20}$$

where C is the capacitance and L is the total inductance of the circuit $L = L_K(I) + L_g$. To obtain the Hamiltonian, we Legendre transform and change the general coordinates to $\{\Phi, Q\}(=0)$

$$\mathcal{H} = \frac{1}{2}\frac{Q^2}{C} + \frac{1}{2}\frac{\Phi^2}{L} \tag{6.21}$$

Using canonical transformation, we can replace the general coordinates with quantum operator counterparts $[\mathbf{\Phi}, \mathbf{Q}] = -i\hbar$. The quantum Hamilton operator can now be written as

$$\mathbf{H} = \frac{1}{2}\frac{\mathbf{Q}^2}{C} + \frac{1}{2}\frac{\mathbf{\Phi}^2}{L} \tag{6.22}$$

where bold H, Q and Φ are the quantum operators.

Suppose we assume the kinetic inductance ratio is close to one, which is the case for a nanowire. In that case, the total inductance of the qubit is found to be dominated by the non-linear kinetic inductance $L \approx L_K(I)$. Using

$$L_k(\Phi) \approx L_{0k}\left(1 + \frac{\Phi^2}{\Phi_*^2}\right) \tag{6.23}$$

where L_{0K} is the kinetic inductance with zero bias and $\Phi_* \equiv I_* L_{0K}$ where I_* is a characteristic current parameter of the nonlinearity, we can rewrite the Hamiltonian

$$\mathbf{H} = \frac{1}{2}\frac{\mathbf{Q}^2}{C} + \frac{1}{2L_{0K}}\left(\mathbf{\Phi}^2 - \frac{\mathbf{\Phi}^4}{\Phi_*^2}\right) \tag{6.24}$$

following orl (2022) we rewrite the Hamiltonian as

$$\mathbf{H} = 4E_c\mathbf{n}^2 + \frac{1}{2}E_K\left(\boldsymbol{\phi}^2 - \lambda\,\boldsymbol{\phi}^4\right) \tag{6.25}$$

where $E_K = \frac{\phi_0^2}{2L_K}$ and we define $\lambda = \left(\frac{\phi_0}{\Phi_*}\right)^2$. Writing the above equation in the second quantization language using the ladder operators $\boldsymbol{a}$ and $\boldsymbol{a}^\dagger$, we get

$$\mathbf{H} = \hbar\omega\boldsymbol{a}_{\boldsymbol{k}}^\dagger\boldsymbol{a}_{\boldsymbol{k}} - E_K'\left[\boldsymbol{\phi}^4 + ...\right] \tag{6.26}$$

where E_K' is the energy of the non-linear term.

Now adding the Hamiltonian of the cavity resonator, we arrive at the full Hamiltonian of the Kineticon-cavity system.

$$\mathbf{H}_{fulll} = \hbar\omega\boldsymbol{a}_{\boldsymbol{c}}^\dagger\boldsymbol{a}_{\boldsymbol{c}} + \hbar\omega\boldsymbol{a}_{\boldsymbol{k}}^\dagger\boldsymbol{a}_{\boldsymbol{k}} - E_K'\left[\boldsymbol{\phi}^4 + ...\right] \tag{6.27}$$

where the subscript c stands for the cavity. The first two terms are the linear part of the full Hamiltonian, and the third term is the non-linear part, therefore

$$\mathbf{H}_{full} = \mathbf{H}_{lin} + \mathbf{H}_{nol} \tag{6.28}$$

Where we defined the linear as follows

$$\mathbf{H}_{lin} = \sum_{m=1}^{2} \hbar\omega_m \boldsymbol{a_m^\dagger a_m} \tag{6.29}$$

where m is the mode number, and in this case, $m = 1$ is the qubit mode and $m = 2$ is the cavity's mode. We can now re-write Equation (6.28) as follows.

$$\mathbf{H}_{full} = \sum_{m=1}^{2} \hbar\omega_m \boldsymbol{a_m^\dagger a_m} - E_K' \left[\boldsymbol{\phi}^4 + ...\right] \tag{6.30}$$

Therefore we have combined the linear part of the qubit Hamiltonian with that of the cavity. We can now solve the linear part using a Finite Element (FE) solver such as HFSS to determine the linear part of the total Hamiltonian. Since the nonlinear part of the total Hamiltonian is a function of ϕ, we can determine the nonlinear part of the Hamiltonian. The ϕ operator is given by (See the Appendix for more details)

$$\boldsymbol{\phi} = \sum_{m=1}^{2} \phi_m \left(\boldsymbol{a_m^\dagger} + \boldsymbol{a_m}\right) \tag{6.31}$$

Here, ϕ_m is the zero-point fluctuation of the nanowire due to mode m, and it can be thought of as fluctuations in voltage drop across the nanowire. Finding ϕ_m will allow us to construct the $\boldsymbol{\phi}$ operator and determine the nonlinear Hamiltonian portion of the total Hamiltonian.

We start by calculating the energy participation ratio p_m of the qubit mode as defined in Minev *et al.* (2021) using HFSS.

$$p_m = \frac{\mathcal{E}_{elec} - \mathcal{E}_{mag}}{\mathcal{E}_{elec}} \tag{6.32}$$

This is a classical result from the FE analysis and tells us the amount of energy stored in the nanowire for mode m. The quantum mechanical description of the EPR is as follows.

$$p_m = \frac{\left\langle \frac{\phi^2}{2L_K} \right\rangle}{\left\langle \frac{1}{2}\mathcal{E} \right\rangle} = \frac{2\phi_m^2}{L_K \hbar\omega_m} \tag{6.33}$$

combining Equations (6.32) and (6.33), we arrive at the following equation for ϕ_m

$$\phi_m^2 = p_m \frac{\hbar\omega_m}{2E} \tag{6.34}$$

Once we solve the Hamiltonian, we can extract the values of anharmonicity, cross Kerr coefficient, Lamb shift, etc.

We set up our HFSS simulations as follows. To embed the Kineticon qubit in a 3D readout cavity, we have designed and simulated a $\sim$ 100 GHz resonant cavity coupled to a waveguide using an evanescent coupler as shown in Fig. 6.17.a. The cavity dimensions were adjusted such that the cavity's resonant frequency of the cavity-substrate system is nearly 100 GHz. In this case, the cavity dimensions are; width = 1 mm, height = 2.54, and depth = 1.4 mm. The Kineticon qubit is placed in the cavity's middle, where the qubit's dipole moment is aligned with the TE_{101} mode and where the electric field is maximum. However, we would like to make sure the higher modes, such as TE_{102} and TE_{103}, will not have a substantial effect on the qubit. We can simulate these higher modes in the cavity with the qubit present to adjust the position of the qubit in the cavity, as shown in Fig. 6.15.

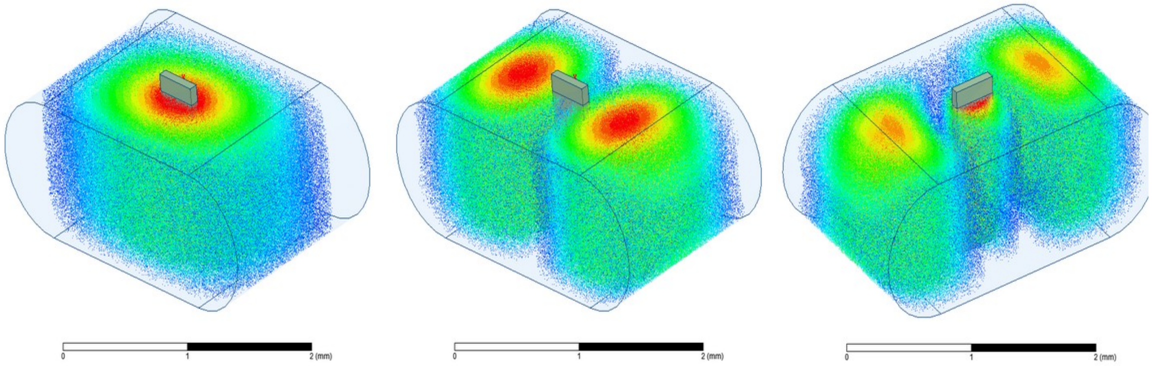

TE_{101} = 98.5 GHz TE_{102} = 154 GHz TE_{103} = 179.7 GHz

Figure 6.15: The 3D plot of HFSS Simulation of the Intensity of the Electric Field for Modes TE_{101}, TE_{102} and TE_{103} in the Cavity Where Red Spots Correspond to the Higher Magnitude Electric Fields and the Blue Spots are Lower Magnitudes Electric Fields.

The transmission response of the cavity-qubit system is shown in Fig.6.17.c, where both qubit and cavity modes are visible. The qubit is designed to have two capacitive pads with dimensions of $45\,\mu m \times 30\,\mu m$ and a nanowire section of $50\,nm\ \times 100\,nm$ on a $25\,\mu m$ thick silicon substrate.

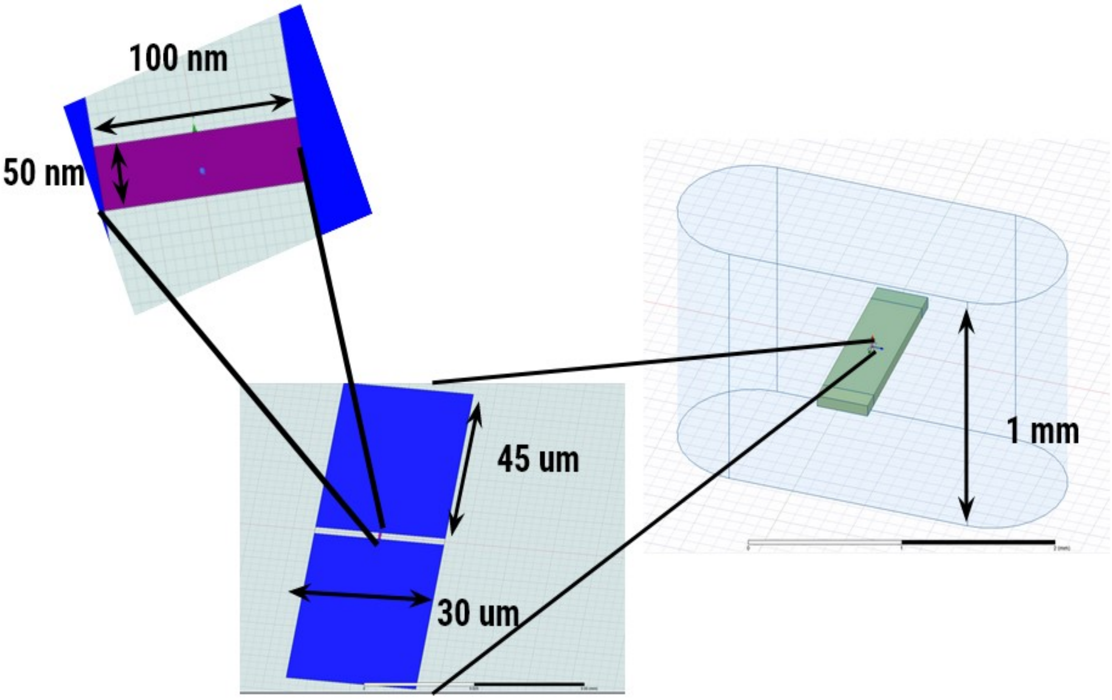

Figure 6.16: HFSS Drawings of the Cavity with Embedded Kineticon Chip. The Cavity Dimensions are in the Order of mm, the Capacitive Pads are in the Order of Microns, and the Nanowire is $50\,nm \times 100\,nm$.

Fig. 6.17 shows the cavity-qubit system coupled to a straight waveguide section through an evanescent coupling section. The simulated S_{21} response of the whole system is shown in Fig. 6.17, where we can see both the qubit and the cavity modes as indicated in the figure.

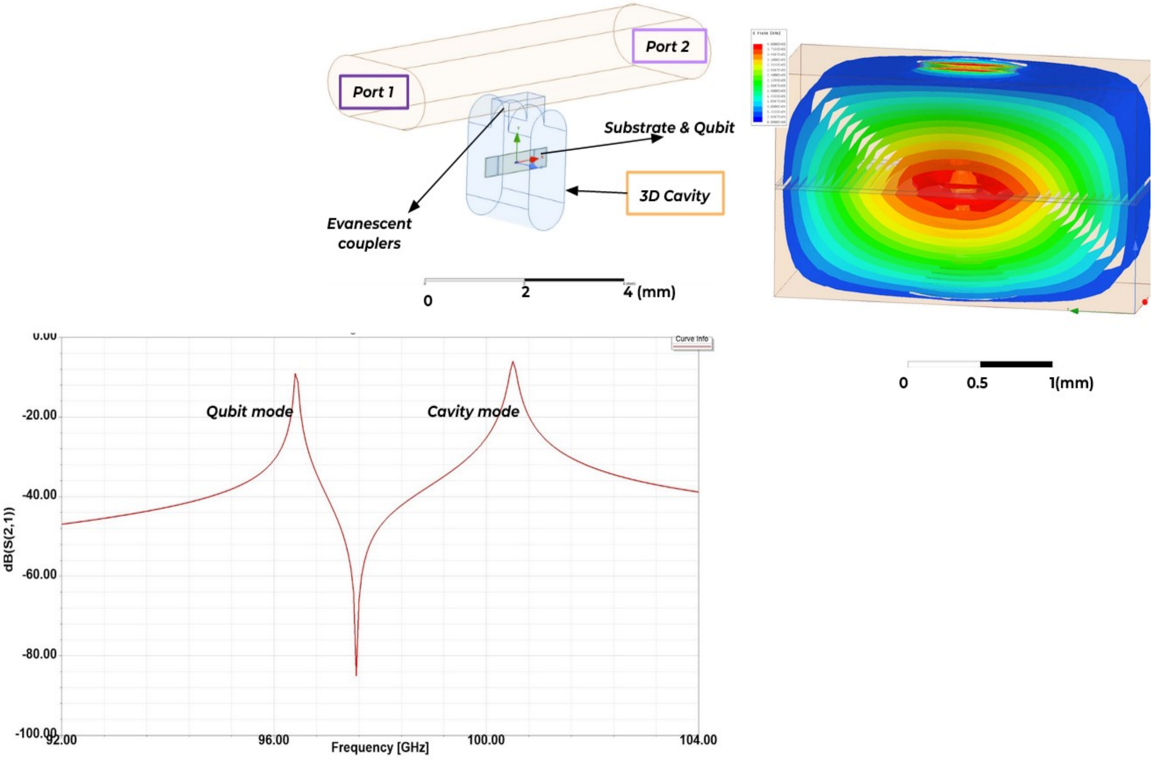

Figure 6.17: *a)* HFSS Overview Drawing of the 3D System of a Qubit Coupled to a 3D Readout Cavity, Coupled Evanescently to Readout Waveguides. A Gray Slab in the Middle of the 3D Cavity Would Hold the Qubit Device. *b)* The Magnitude of the Electric Field at the Cavity Mode in the 3D Readout Cavity. Qubit is Located at the Center of this Cavity, Where the Electric Field is Maximum. *c)* S_{21} Calculated Response of the Qubit-Cavity System Showing Separation of the Qubit and Cavity Resonances.

Calculating the energy participation ratios p_m of both the qubit and the cavity and using the following equations

$$\alpha_1 = p_1^2 \frac{\hbar\omega_1^2}{8E_K} \tag{6.35}$$

$$\alpha_2 = p_2^2 \frac{\hbar\omega_2^2}{8E_K} \tag{6.36}$$

$$\chi_{12} = p_2^2 \frac{\hbar\omega_2^2}{8E_K} \tag{6.37}$$

$$\Delta = \alpha_1 - \frac{1}{2}\chi_{12} \tag{6.38}$$

Where α_1 and α_2 are the anharmonicities of the qubit and the cavity, respectively. χ_{12} is the cross Kerr coefficient and Δ is the Lamb shift. Calculating the energy participation ratios for the cavity-qubit system and solving the full Hamiltonian, we get the following parameters.

qubit α	cavity α	cross Kerr χ	Lamb shift	coupling rate	detuning $\Delta\omega$
388 MHz	715.16 kHz	36.8 MHz	369 MHz	163 MHz	5.1 GHz

Table 6.2: Optimized Kineticon-Cavity Parameters Using the Energy Participation Ratio (EPR) Method.

The detuning frequency $\Delta\omega = \omega_c - \omega_q$ is much larger than the coupling rate g, which will allow us to conduct non-demolition measurement of the qubit by looking at the shift in the resonant frequency of the cavity.

6.2.4 Decoherence and Loss

Apart from the possibility of high-frequency operation, an advantage of circuits made from relatively high T_c materials is that they can be less affected by quasiparticles:

- The thermal quasiparticle density goes as $e^{-2\Delta/T}$.
- The mean number of non-thermal quasiparticles produced by absorption of a phonon of a given energy is $\xi h\nu/\Delta$, where ν is the phonon frequency, and ξ is a material-dependent parameter (around 0.5 for most materials).
- Quasiparticles that are created through leakage of radiation into the cryogenic environment recombine at a rate that scales as T_c^{-3} Kaplan *et al.* (1976).

In addition to lower quasiparticle loss, the nitride superconductors we will study may be affected less by loss and decoherence associated with two-level systems. It is known, for example, that TiN and NbTiN have high-quality surfaces and form more stable and thinner oxide layers Zhang *et al.* (2018), unlike elemental superconductors such as Al, Nb, and Ta. TiN, in particular, is a hard material used as a coating on machine tools, drill bits, etc. Groups working on kinetic inductance detectors have found that fabricating the non-photoresponsive parts of the detectors out of NbTiN leads to lower TSS noise Bueno *et al.* (2017); Janssen *et al.* (2014). Recent results on transmon qubits using Ta electrodes have shown an improvement over state-of-the-art coherence times Place *et al.* (2020), which was associated with the favorable properties of the tantalum oxide surface, so it is interesting to ask whether the metal nitride superconductors and other potential materials for Kineticons, will provide further improvement.

6.2.5 Implantation and Path Forward

To realize an mm-wave qubit, we started with fabricating the cavity waveguide housing for the qubit. The cavity was machined out of QC aluminum by our collaborators Bradly Johnson and Peter Dow at the University of Virginia. Fig. 6.18 shows a picture of the machined cavity.

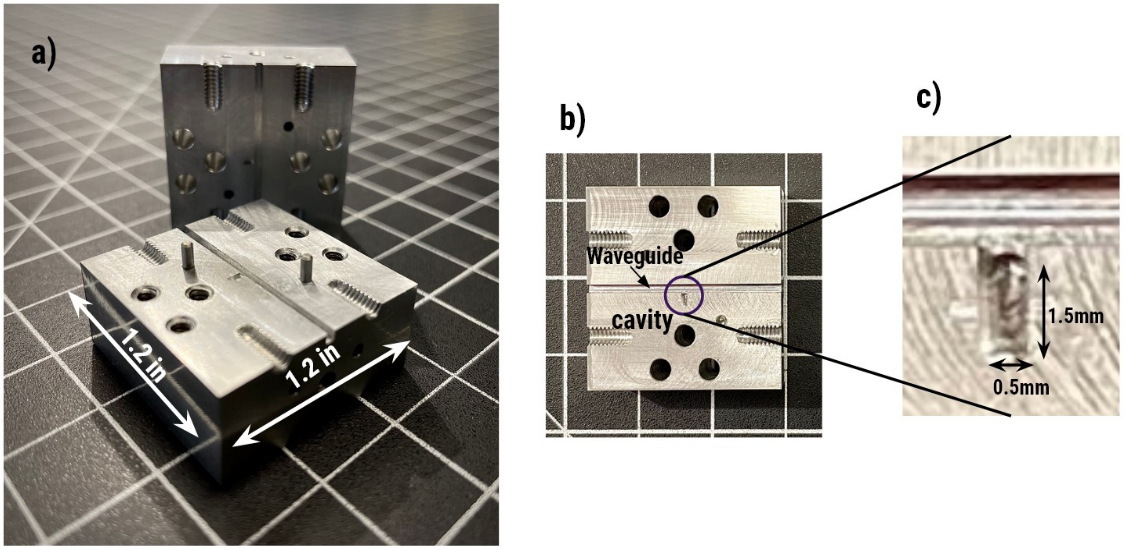

Figure 6.18: *a)* shows the Split Block Structure, Which Contains the Waveguide, Evanescent Coupler, and Cavity. *b,c)* Shows the Location of the Cavity and the Size of the Cavity with a Depth of 1.8 mm.

The S_{21} transmission of the waveguide-cavity housing was measured at room temperature using VNA extenders, as shown in Fig. 6.19. The resonant frequency of the empty cavity is higher than the cavity with the qubit mounted inside the cavity because the silicon substrate changes the effective dielectric constant of the cavity and consequently lowers the resonant frequency. The extracted internal quality factor from the fit is 1582 at room temperature.

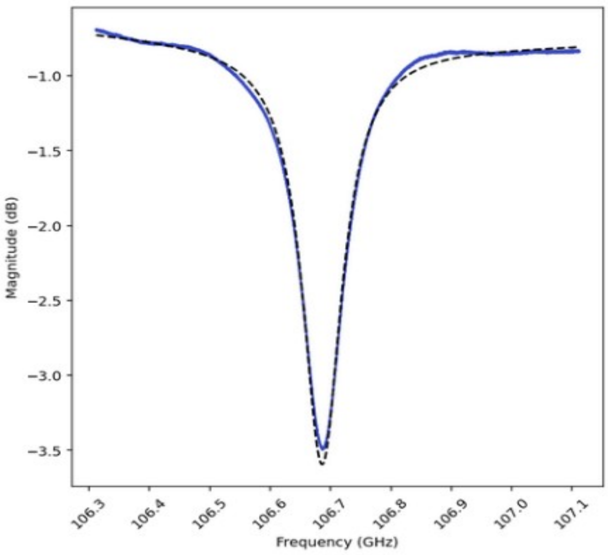

Figure 6.19: Plot of Measured Response of the Aluminum Cavity Resonator at 300 K with Qi = 1582 and Qc = 4133.

We attempted to measure the cavity at lower temperatures multiple times; however, the lowest temperature we could reach with the current setup was about 23K. The test setup is shown in Fig. 6.21. To improve the test setup, we need to make adjustments to copper heat sinks, add more of them, and ensure each waveguide section and waveguide component is heat sunk properly to different cooling stages of the cryostat. For this measurement, we used a combination of an attenuator, isolator, and waveguide sections routed in the cryostat as mentioned in previous chapters with the circuit diagram shown in Fig. 6.20. From Fig.6.22 the plot of S_{21} of the cavity, we can see that the resonant frequency has shifted to 107.125 GHz, and this is due to the contraction of aluminum at a lower temperature which reduces the size of the cavity and shifts the resonance frequency to a higher value. From the fit of the resonator, we extract a value of 2250 for the internal quality, which is higher than the value of 1582 at room temperature because of the lower surface resistance of aluminum at lower temperatures.

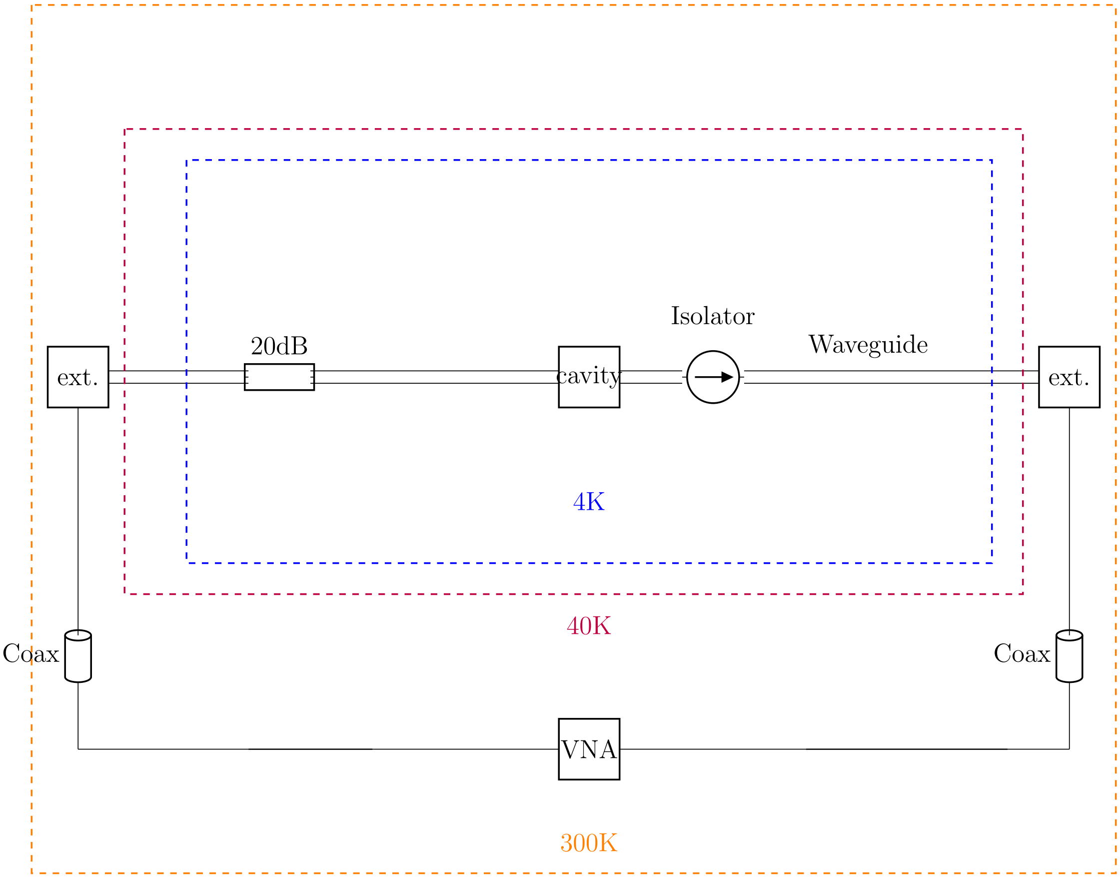

Figure 6.20: Circuit Diagram of the Measurement Test Setup Used for the W-band Cavity.

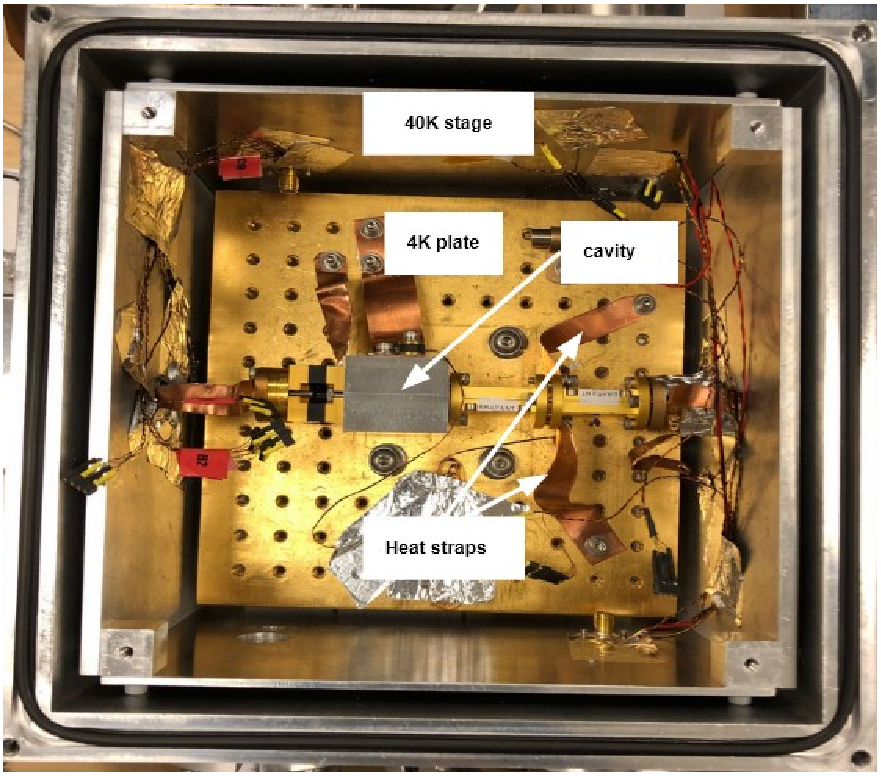

Figure 6.21: Image of the Cryogenic Test Setup for Cavity Measurements.

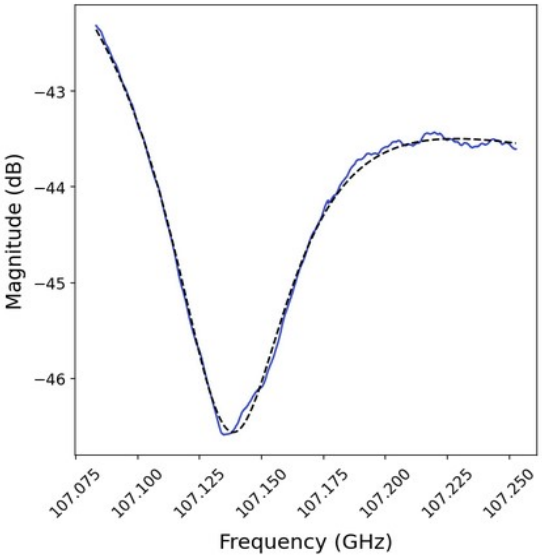

Figure 6.22: Plot of S_{21} of the Cavity Resonator in dB Versus Frequency at 23 Kelvin.

Moving forward, we can improve the internal quality factor by sputtering with niobium on the cavity and measuring it at temperatures below ~ 1 K.

For the qubit chip, the first approach would be to make the whole qubit structure out of a single layer of NbN for ease of fabrication. A design for such a device is shown in Fig. 6.23 with 14 nm thick NbN film on a Silicon-on-Insulator (SOI) wafer with a device layer thickness of 25 microns. We can use an e-beam lithography method to pattern both the capacitive pads with the nanowire. Then, we need to etch the device layer silicon to the shape of the chip borders and remove the handle silicon and the SiO_2 layer very carefully. This last step needs to be done very cautiously such that the very fragile devices would not get damaged or get lost.

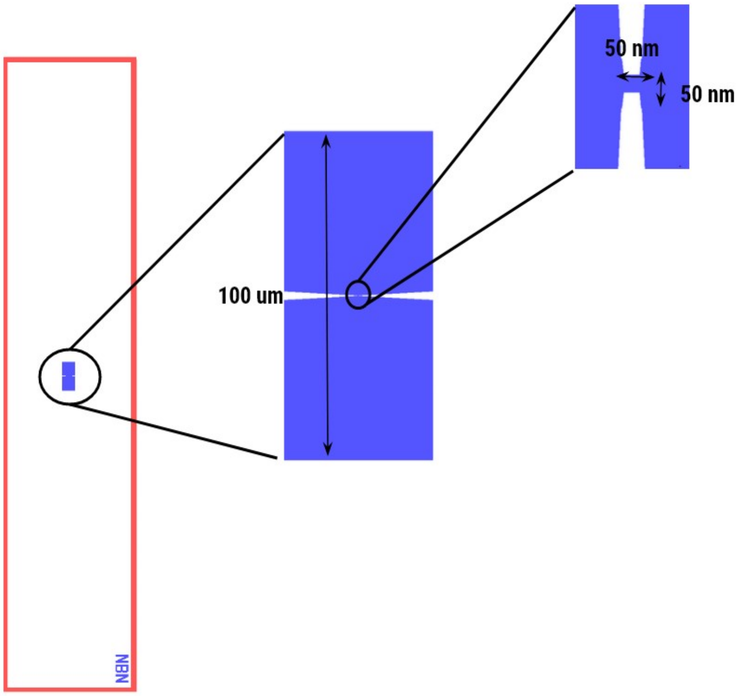

Figure 6.23: Fabrication Mask Drawing of a Single Layer NbN Kineticon Design with a $50\,nm \times\ 50\,nm$ Size Nanowire.

Chapter 7

CONCLUSIONS AND OUTLOOK

This thesis has shown different designs and utilities of non-linear kinetic inductance-based superconducting and quantum devices. These devices operate in the millimeter wave region of the electromagnetic spectrum and have applications in observational cosmology, astrophysics, and quantum computing and sensing. We presented design considerations and examples for millimeter wave superconducting and quantum devices using multiple EM simulation platforms. Fabrication of such devices and the development of cryogenic test structures and measurement methods and techniques were also discussed.

We mainly focused on the non-linear kinetic inductance property of superconducting thin films with high normal resistivities, such as NbN and NbTiN. The non-linearity was exploited by biasing with DC and AC signals. The devices presented in this work include kinetic inductance traveling wave parametric amplifiers, superconducting on-chip Mach-Zehnder interferometers, millimeter wave resonators, and a new type of qubit operating in the millimeter wave regime, which we have called Kineticon.

The Superconducting On-chip Fourier Transform Spectrometer (SOFTS) device explained in this thesis has received a significant amount of attention from the observational cosmology community, and it was awarded a NASA APRA grant in 2021. In this work, we showed and demonstrated the necessary steps for the design, fabrication, and measurement of the device. We have identified the shortcomings and the path forward toward a successful device. For one of the next steps, I suggest fabricating single DC-biased W-band transmission lines and measuring the current-induced phase shift in the transmission line below 1 Kelvin. The transmission lines have already been designed by our collaboration and are currently in the fabrication process. Additionally, we plan to use commercially available W-band components such as power splitters and absolute power detectors to build the Mach-Zehnder circuit with waveguide components and two packaged DC-biased transmission lines. This way, we can identify any possible shortcomings in the circuit with the interferometric measurement. In parallel with this effort, I suggest designing a 4-port housing structure for developing and testing other mm-wave sub-systems, such as the on-chip hybrids and diplexers.

The path forward for millimeter wave parametric amplifiers is redesigning and using housings that maximize the coupling between the waveguides and the probe antennas, such as adding an air channel below the chip to suppress unwanted modes. Improving the fabrication yield for these devices is of utmost importance due to the small quarter-micron-wide structures. The nanofabrication experts led by Dr. Henry LeDuc are leading this effort at the Microdevices Lab at Jet Propulsion Laboratory. A significant amount of improvements have already been achieved with newly fabricated devices, such as the low-frequency parametric amplifiers presented in this thesis. Another important step forward for the millimeter wave paramp is to make noise measurements using a cryogenic noise source at 1 Kelvin and demonstrate the quantum noise limit performance. The gain of these devices also needs improvement from currently 5 dB to a higher gain.

Millimeter resonators discussed in the thesis were designed and measured with the purpose of determining loss in the microstrip line geometry used for other devices. Their relatively high-quality factors of $> 60,000$ are very promising. Also, the measurement of these resonators in the nonlinear regime has given us insight into the performance of nonlinear kinetic inductance devices in the millimeter range by calculating the characteristic energy and the nonlinearity factor. Moving forward, two avenues would be interesting to explore. One is to measure resonators with no dielectric deposited on top and compare their quality factors with the ones we have already measured. This will allow us to estimate how much of the loss is due to the loss tangent of the a-Si. The second would be patterning ring-shaped resonators on the silicon substrate and coupling them to a waveguide directly through dipole interaction. Using the ring geometry for the resonators will allow us to DC-bias the resonators with a Helmholtz coil and measure their current-dependent resonant frequency response. This will be a direct way of measuring the current dependence of kinetic inductance at millimeter waves.

Kineticon can be used as a qubit for quantum computation and as a millimeter wave single photon counter. In this thesis, we have shown theoretically that the construction of such a qubit is possible through numerical calculations and simulations. We have also designed a cavity and a qubit for measurements. In this thesis, we were able to show measurements of the cavity, and the next step would be to fabricate the qubit chip and incorporate it into the cavity. The fabrication steps need to be thought out carefully and implemented with care to keep the fragile chips from damage. Moving forward, we need to measure the cavity-qubit system at 1 Kelvin and identify both the cavity and qubit tones using one-tone and two-tone spectroscopy measurements. Eventually, we must perform a Rabi oscillation measurement to find the qubit relaxation times.

REFERENCES

"Planck 2015 cosmological results", AIP Conference Proceedings (2016).

"Superconducting qubits", Quantum Information and Quantum Optics with Superconducting Circuits p. 106–155 (2022).

Aalto, S., Polatidis, A. G., Hüttemeister, S. and Curran, S. J., "Cn and hnc line emission in ir luminous galaxies", A&A **381**, 3, 783–794, URL `https://doi.org/10.1051/0004-6361:20011514` (2002).

Anferov, A., A. Suleymanzade, A. Oriani, J. Simon and D. I. Schuster, "Millimeter-wave four-wave mixing via kinetic inductance for quantum devices", Physical Review Applied **13**, 2 (2020a).

Anferov, A., A. Suleymanzade, A. Oriani, J. Simon and D. I. Schuster, "Millimeter-wave four-wave mixing via kinetic inductance for quantum devices", Phys. Rev. Applied **13**, 024056 (2020b).

Annunziata, A. J., D. F. Santavicca, L. Frunzio, G. Catelani, M. J. Rooks, A. Frydman and D. E. Prober, "Tunable superconducting nanoinductors", Nanotechnology **21**, 44, 445202, URL `https://doi.org/10.10882F0957-44842F212F442F445202` (2010).

Anthore, A., H. Pothier and D. Esteve, "Density of states in a superconductor carrying a supercurrent", Physical Review Letters **90**, 12 (2003).

Aref, T. and A. Bezryadin, "Precisein situtuning of the critical current of a superconducting nanowire using high bias voltage pulses", Nanotechnology **22**, 39, 395302, URL `https://doi.org/10.10882F0957-44842F222F392F395302` (2011).

Arute, "Quantum supremacy using a programmable superconducting processor", Nature **574**, 7779, 505–510, URL `https://www.nature.com/articles/s41586-019-1666-5` (2019).

Asztalos, S. J., G. Carosi, C. Hagmann, D. Kinion, K. van Bibber, M. Hotz, L. J. Rosenberg, G. Rybka, J. Hoskins, J. Hwang and et al., "Squid-based microwave cavity search for dark-matter axions", Physical Review Letters **104**, 4 (2010).

Auston, D. H. and K. P. Cheung, "Coherent time domain far-infrared spectroscopy", Springer Series in Optical Sciences p. 336–339 (1985).

Bardeen, J., L. N. Cooper and J. R. Schrieffer, "Theory of superconductivity", Physical Review **108**, 5, 1175–1204 (1957).

Bartram, C., "Dark matter axion search using a josephson traveling wave parametric amplifier", Preprint at ArXiv (2021).

Barzanjeh, S., D. P. DiVincenzo and B. M. Terhal, "Dispersive qubit measurement by interferometry with parametric amplifiers", Physical Review B **90**, 13 (2014).

Basu Thakur, R., N. Klimovich, P. K. Day, E. Shirokoff, P. Mauskopf, F. Faramarzi and P. S. Barry, "Superconducting on-chip fourier transform spectrometer", Journal of Low Temperature Physics **200**, 342–352 (2020).

Basu Thakur, R., A. Steiger, S. Shu, F. Faramarzi, N. Klimovich, P. K. Day, E. Shirokoff, P. D. Mauskopf and P. S. Barry, "Development of superconducting on-chip fourier transform spectrometers", Journal of Low Temperature Physics (2022).

Bradford, C. M., J. J. Bock, M. Harwit, G. Helou, H. Matsuhara, T. Matsumoto, T. Nakagawa, E. Young, BLISS Collaboration and SPICA Team, "BLISS and SPICA: Revealing the History of Energy Production in Dusty Galaxies with Far-IR Spectroscopy at the Background Limit", in "American Astronomical Society Meeting Abstracts", vol. 205 of *American Astronomical Society Meeting Abstracts*, p. 100.07 (2004).

Bruno, A., G. de Lange, S. Asaad, K. L. van der Enden, N. K. Langford and L. DiCarlo, "Reducing intrinsic loss in superconducting resonators by surface treatment and deep etching of silicon substrates", Applied Physics Letters **106**, 18, 182601 (2015).

Bryerton, E. W., M. Morgan and M. W. Pospieszalski, "Ultra low noise cryogenic amplifiers for radio astronomy", 2013 IEEE Radio and Wireless Symposium (2013).

Bueno, J., O. Yurduseven, S. J. C. Yates, N. Llombart, V. Murugesan, D. J. Thoen, A. M. Baryshev, A. Neto and J. J. A. Baselmans, "Full characterisation of a background limited antenna coupled kid over an octave of bandwidth for thz radiation", Applied Physics Letters **110**, 23, 233503, URL `https://doi.org/10.1063/1.4985060` (2017).

Burnett, J. J., A. Bengtsson, M. Scigliuzzo, D. Niepce, M. Kudra, P. Delsing and J. Bylander, "Decoherence benchmarking of superconducting qubits", npj Quantum Information **5**, 1, 1–8, URL `https://www.nature.com/articles/s41534-019-0168-5`, number: 1 Publisher: Nature Publishing Group (2019).

Carter, F. W., T. S. Khaire, V. Novosad and C. L. Chang, "scraps: An open-source python-based analysis package for analyzing and plotting superconducting resonator data", IEEE Transactions on Applied Superconductivity **27**, 4, 1–5 (2017).

Casey, C. M., D. Narayanan and A. Cooray, "Dusty star-forming galaxies at high redshift", Physics Reports **541**, 2, 45–161, URL `https://www.sciencedirect.com/science/article/pii/S0370157314000477`, dusty star-forming galaxies at high-redshift (2014).

Chamberland, C., G. Zhu, T. J. Yoder, J. B. Hertzberg and A. W. Cross, "Topological and Subsystem Codes on Low-Degree Graphs with Flag Qubits", Physical Review X **10**, 1, 011022, URL `https://link.aps.org/doi/10.1103/PhysRevX.10.011022`, publisher: American Physical Society (2020).

Chamberlin, R., M. Clark, V. Mujica and G. Wolf, “Multiscale thermodynamics: Energy, entropy, and symmetry from atoms to bulk behavior”, (2021).

Combescot, R., *Superconductivity: An introduction* (Cambridge University Press, 2022).

Day, P. K., H. G. LeDuc, B. A. Mazin, A. Vayonakis and J. Zmuidzinas, “A broadband superconducting detector suitable for use in large arrays”, Nature **425**, 6960, 817–821 (2003).

Devoret, J., M. H. Zinn-Justin, “Quantum fluctuations in electrical circuits”, (1997).

Didier, N., A. Kamal, W. D. Oliver, A. Blais and A. A. Clerk, “Heisenberg-limited qubit read-out with two-mode squeezed light”, Physical Review Letters **115**, 9 (2015).

Dixit, A. V., S. Chakram, K. He, A. Agrawal, R. K. Naik, D. I. Schuster and A. Chou, “Searching for dark matter with a superconducting qubit”, Physical Review Letters **126**, 14 (2021).

Earle, L., P. Ade, J. Aguirre, R. Aikin, J. Battle, J. Bock, C. M. Bradford, M. Dragovan, L. Duband, J. Glenn, G. Griffin, V. Hristov, P. Maloney, H. Matsuhara, B. Naylor, H. Nguyen, M. Yun and J. Zmuidzinas, “Z-Spec: a broadband direct-detection millimeter-wave spectrometer – instrument status and first results”, in “Millimeter and Submillimeter Detectors and Instrumentation for Astronomy III”, edited by J. Zmuidzinas, W. S. Holland, S. Withington and W. D. Duncan, vol. 6275, pp. 311 – 319, International Society for Optics and Photonics (SPIE, 2006), URL `https://doi.org/10.1117/12.672309`.

Endo, A., P. Werf, R. M. J. Janssen, P. J. Visser, T. M. Klapwijk, J. J. A. Baselmans, L. Ferrari, A. M. Baryshev and S. J. C. Yates, “Design of an Integrated Filterbank for DESHIMA: On-Chip Submillimeter Imaging Spectrograph Based on Superconducting Resonators”, Journal of Low Temperature Physics **167**, 3-4, 341–346 (2012).

Eom, B., P. K. Day, H. G. LeDuc and J. Zmuidzinas, “A wideband, low-noise superconducting amplifier with high dynamic range”, Nature Physics **8**, 8, 623–627 (2012).

Faramarzi, F., P. Day, J. Glasby, S. Sypkens, M. Colangelo, R. Chamberlin, M. Mirhosseini, K. Schmidt, K. K. Berggren, P. Mauskopf and et al., “Initial design of a w-band superconducting kinetic inductance qubit”, IEEE Transactions on Applied Superconductivity **31**, 5, 1–5 (2021).

Fixsen, D. J., E. Dwek, J. C. Mather, C. L. Bennett and R. A. Shafer, “The spectrum of the extragalactic far-infrared background from theCOBE-FIRAS observations”, The Astrophysical Journal **508**, 1, 123–128, URL `https://doi.org/10.1086/306383` (1998).

Galati, G., E. G. Piracci and M. Ferri, “High resolution, millimeter-wave radar applications to airport safety”, 2016 8th International Conference on Ultrawideband and Ultrashort Impulse Signals (UWBUSIS) (2016).

Ghribi, A., B. Bélier, F. Boussaha, E. Bréelle, M. Piat, S. Spinelli, A. Tartari and M. Zannoni, “Superconducting planar devices for cosmology”, AIP Conference Proceedings **1185**, 1, 506–510, URL `https://aip.scitation.org/doi/abs/10.1063/1.3292390` (2009).

Goldstein, S., N. Kirsh, E. Svetitsky, Y. Zamir, O. Hachmo, C. E. de Oliveira and N. Katz, “Four wave-mixing in a microstrip kinetic inductance travelling wave parametric amplifier”, Applied Physics Letters **116**, 15, 152602 (2020).

Gong, Y., A. Cooray and M. G. Santos, “PROBING THE PRE-REIONIZATION EPOCH WITH MOLECULAR HYDROGEN INTENSITY MAPPING”, The Astrophysical Journal **768**, 2, 130, URL `https://doi.org/10.1088/0004-637x/768/2/130` (2013).

Greve, T. R., F. Bertoldi, I. Smail, R. Neri, S. C. Chapman, A. W. Blain, R. J. Ivison, R. Genzel, A. Omont, P. Cox, L. Tacconi and J.-P. Kneib, “An interferometric CO survey of luminous submillimetre galaxies”, Monthly Notices of the Royal Astronomical Society **359**, 3, 1165–1183, URL `https://doi.org/10.1111/j.1365-2966.2005.08979.x` (2005).

Gurvits, L. I., “Space vlbi: From first ideas to operational missions”, Advances in Space Research **65**, 2, 868–876 (2020).

Hansryd, J., P. Andrekson, P.-O. Hedekvist, J. Li and M. Westlund, “Optical parametric amplifiers and their applications”, Optical Fiber Communication Conference and Exhibit (2002).

Hashimoto, T., “The onset of star formation 250 million years after the big bang”, Proceedings of the International Astronomical Union **15**, S341, 221–225 (2019).

Helmich, F., “Herschel hifi - the heterodyne instrument for the far-infrared”, EAS Publications Series **52**, 15–20 (2011).

Irwin, K. D., “Phonon-mediated particle detection using superconducting tungsten transition-edge sensors”, (1995).

Janssen, R. M. J., J. J. A. Baselmans, A. Endo, L. Ferrari, S. J. C. Yates, A. M. Baryshev and T. M. Klapwijk, “Performance of hybrid NbTiN-Al microwave kinetic inductance detectors as direct detectors for sub-millimeter astronomy”, in “Millimeter, Submillimeter, and Far-Infrared Detectors and Instrumentation for Astronomy VII”, edited by W. S. Holland and J. Zmuidzinas, vol. 9153, pp. 261 – 267, International Society for Optics and Photonics (SPIE, 2014), URL `https://doi.org/10.1117/12.2055537`.

Jepsen, P., D. Cooke and M. Koch, “Terahertz spectroscopy and imaging - modern techniques and applications”, Laseramp; Photonics Reviews **5**, 1, 124–166 (2010).

Kaplan, S., C. Chi, D. Langenberg, J.-J. Chang, S. Jafarey and D. Scalapino, "Quasiparticle and phonon lifetimes in superconductors", Physical Review B **14**, 11, 4854 (1976).

Kerman, A. J., "Metastable superconducting qubit", Phys. Rev. Lett. **104**, 027002, URL `https://link.aps.org/doi/10.1103/PhysRevLett.104.027002` (2010).

Kerr, A. R., S.-K. Pan, S. M. Claude, P. Dindo, A. W. Lichtenberger, J. E. Effland and E. F. Lauria, "Development of the alma band-3 and band-6 sideband-separating sis mixers", IEEE Transactions on Terahertz Science and Technology **4**, 2, 201–212 (2014).

Kher, A. S., *Superconducting nonlinear kinetic inductance devices*, Ph.D. thesis (2017).

Klimov, P. V., J. Kelly, Z. Chen, M. Neeley, A. Megrant, B. Burkett, R. Barends, K. Arya, B. Chiaro, Y. Chen, A. Dunsworth, A. Fowler, B. Foxen, C. Gidney, M. . Giustina, R. Graff, T. Huang, E. Jeffrey, E. Lucero, J. Y. Mutus, O. Naaman, C. Neill, C. Quintana, P. Roushan, A. Sank, Daniel a nd Vainsencher, J. Wenner, T. C. White, S. Boixo, R. Babbush, V. N. Smelyanskiy, H. Neven and J. M. Martinis, "Fluctuations of Energy-Relaxation Times in Superconducti ng Qubits", Physical Review Letters **121**, 9, 090502, URL `https://link.aps.org/doi/10.1103/PhysRevLett.121.090502` (2018).

Klimovich, N. S., *Traveling wave parametric amplifiers and other nonlinear kinetic inductance devices*, Ph.D. thesis (2022).

Kooi, J. W., G. Chattopadhyay, S. Withington, F. Rice, J. Zmuidzinas, C. Walker and G. Yassin, International Journal of Infrared and Millimeter Waves **24**, 3, 261–284 (2003).

Kouveliotou, C., E. Agol, N. Batalha, J. Bean, M. Bentz, N. Cornish, A. Dressler, E. Figueroa-Feliciano, S. Gaudi, O. Guyon, D. Hartmann, J. Kalirai, M. Niemack, F. Ozel, C. Reynolds, A. Roberge, K. S. A. Straughn, D. Weinberg and J. Zmuidzinas, "Enduring quests-daring visions (nasa astrophysics in the next three decades)", (2014).

Lawrence, N. P., B. W.-H. Ng, H. J. Hansen and D. Abbott, "5g terrestrial networks: Mobility and coverage—solution in three dimensions", IEEE Access **5**, 8064–8093 (2017).

Lazareff, B., "Instrumentation for heterodyne mm-wave astronomy", EAS Publications Series **37**, 37–48 (2009).

Leduc, H. G., B. Bumble, P. K. Day, B. H. Eom, J. Gao, S. Golwala, B. A. Mazin, S. McHugh, A. Merrill, D. C. Moore *et al.*, "Titanium nitride films for ultrasensitive microresonator detectors", Applied Physics Letters **97**, 10, 102509 (2010).

Leisawitz, D., "Nasa's far-ir/submillimeter roadmap missions: Safir and specs", Advances in Space Research **34**, 3, 631–636 (2004).

Levenson-Falk, E. M., R. Vijay and I. Siddiqi, “Nonlinear microwave response of aluminum weak-link josephson oscillators”, Applied Physics Letters **98**, 12, 123115 (2011).

Mattis, D. C. and J. Bardeen, “Theory of the anomalous skin effect in normal and superconducting metals”, Physical Review **111**, 2, 412–417 (1958a).

Mattis, D. C. and J. Bardeen, “Theory of the anomalous skin effect in normal and superconducting metals”, Phys. Rev. **111**, 412–417, URL `https://link.aps.org/doi/10.1103/PhysRev.111.412` (1958b).

Minev, Z. K., Z. Leghtas, S. O. Mundhada, L. Christakis, I. M. Pop and M. H. Devoret, “Energy-participation quantization of josephson circuits”, npj Quantum Information **7**, 1 (2021).

Minutolo, L., B. Steinbach, A. Wandui and R. O’Brient, “A flexible gpu-accelerated radio-frequency readout for superconducting detectors”, IEEE Transactions on Applied Superconductivity **29**, 5, 1–5 (2019).

Mirhosseini, M., A. Sipahigil, M. Kalaee and O. Painter, “Superconducting qubit to optical photon transduction”, Nature **588**, 7839, 599–603 (2020).

Multani, K. K., H. Stokowski, E. Snively, R. Patel, W. Jiang, N. Lee, P. B. Welander, E. A. Nanni and A. H. Safavi-Naeini, “Development of a millimeter-wave transducer for quantum networks”, 2020 45th International Conference on Infrared, Millimeter, and Terahertz Waves (IRMMW-THz) (2020).

National Academies of Sciences, E., *Quantum Computing: Progress and Prospects* (2018), URL `https://www.nap.edu/catalog/25196/quantum-computing-progress-and-prospects`.

Naylor, B. J., P. A. R. Ade, J. J. Bock, C. M. Bradford, M. Dragovan, L. Duband, L. Earle, J. Glenn, H. Matsuhara, H. Nguyen, M. Yun and J. Zmuidzinas, “Z-Spec: a broadband direct-detection millimeter-wave spectrometer”, in “Millimeter and Submillimeter Detectors for Astronomy”, edited by T. G. Phillips and J. Zmuidzinas, vol. 4855, pp. 239 – 248, International Society for Optics and Photonics (SPIE, 2003), URL `https://doi.org/10.1117/12.459419`.

Naylor, D. A. and B. G. Gom, “SCUBA-2 imaging Fourier transform spectrometer”, in “Imaging Spectrometry IX”, edited by S. S. Shen and P. E. Lewis, vol. 5159, pp. 91 – 101, International Society for Optics and Photonics (SPIE, 2004), URL `https://doi.org/10.1117/12.506395`.

Paik, H., D. I. Schuster, L. S. Bishop, G. Kirchmair, G. Catelani, A. P. Sears, B. R. Johnson, M. J. Reagor, L. Frunzio, L. I. Glazman, S. M. Girvin, M. H. Devoret and R. J. Schoelkopf, “Observation of high coherence in josephson junction qubits measured in a three-dimensional circuit qed architecture”, Phys. Rev. Lett. **107**, 240501, URL `https://link.aps.org/doi/10.1103/PhysRevLett.107.240501` (2011).

Pechal, M. and A. H. Safavi-Naeini, “Millimeter-wave interconnects for microwave-frequency quantum machines”, Physical Review A **96**, 4 (2017).

Peng, K., M. Naghiloo, J. Wang, G. D. Cunningham, Y. Ye and K. P. O’Brien, “Floquet-mode traveling-wave parametric amplifiers”, PRX Quantum **3**, 2 (2022).

Piironen, P., “Millimetre-wave direct detection receivers for earth observation instruments – trends and challenges”, 2022 14th Global Symposium on Millimeter-Waves amp; Terahertz (GSMM) (2022).

Pilbratt, G. L., J. R. Riedinger, T. Passvogel, G. Crone, D. Doyle, U. Gageur, A. M. Heras, C. Jewell, L. Metcalfe, S. Ott and et al., “herschelspace observatory”, Astronomy and Astrophysics **518** (2010).

Place, A. P., L. V. Rodgers, P. Mundada, B. M. Smitham, M. Fitzpatrick, Z. Leng, A. Premkumar, J. Bryon, S. Sussman, G. Cheng *et al.*, “New material platform for superconducting transmon qubits with coherence times exceeding 0.3 milliseconds”, arXiv preprint arXiv:2003.00024 (2020).

Pogosian, L., M. Shimon, M. Mewes and B. Keating, “Future cmb constraints on cosmic birefringence and implications for fundamental physics”, Physical Review D **100**, 2 (2019).

Pospieszalski, M. W., “Cryogenic amplifiers for jansky very large array receivers”, 2012 19th International Conference on Microwaves, Radar amp; Wireless Communications (2012).

Pozar, D. M., *Microwave Engineering*, vol. 4 (Wiley, 2011), 4 edn.

Ramanathan, K., N. Klimovich, R. B. Thakur, B. H. Eom, H. G. LeDuc, S. Shu, A. D. Beyer and P. K. Day, “Wideband direct detection constraints on hidden photon dark matter with the qualiphide experiment”, URL `https://arxiv.org/abs/2209.03419` (2022).

Ranzani, L., M. Bal, K. C. Fong, G. Ribeill, X. Wu, J. Long, H.-S. Ku, R. P. Erickson, D. Pappas, T. A. Ohki and et al., “Kinetic inductance traveling-wave amplifiers for multiplexed qubit readout”, Applied Physics Letters **113**, 24, 242602 (2018).

Rappaport, T. S., S. Sun, R. Mayzus, H. Zhao, Y. Azar, K. Wang, G. N. Wong, J. K. Schulz, M. Samimi, F. Gutierrez and et al., “Millimeter wave mobile communications for 5g cellular: It will work!”, IEEE Access **1**, 335–349 (2013).

Renard, S., F. Malbet, E. Thiébaut and J.-P. Berger, “Imaging reconstruction for infrared interferometry: First images of ysos environment”, SPIE Proceedings (2008).

Roh, W., J.-Y. Seol, J. Park, B. Lee, J. Lee, Y. Kim, J. Cho, K. Cheun and F. Aryanfar, “Millimeter-wave beamforming as an enabling technology for 5g cellular communications: Theoretical feasibility and prototype results”, IEEE Communications Magazine **52**, 2, 106–113 (2014).

Rose-Innes, A. C. and E. H. Rhoderick, *Introduction to superconductivity* (Pergamon Press, 1994).

Schillaci, Alessandro, D'Alessandro, Giuseppe, de Bernardis, Paolo, Masi, Silvia, Novaes, Camila Paiva, Gervasi, Massimo and Zannoni, Mario, "Efficient differential fourier-transform spectrometer for precision sunyaev-zeldovich effect measurements", A&A **565**, A125, URL `https://doi.org/10.1051/0004-6361/201423631` (2014).

Schlör, S., J. Lisenfeld, C. Müller, A. Bilmes, A. Schneider, D. P. Pappas, A. V. Ustinov and M. Weides, "Correlating Decoherence in Transmon Qubits: Low Frequency Noise by Single Fluctuators", Physical Review Letters **123**, 19, 190502, URL `https://link.aps.org/doi/10.1103/PhysRevLett.123.190502`, publisher: American Physical Society (2019).

Schroeder, E., *Development of superconducting nanowire single photon detector technologies for advanced applications*, Ph.D. thesis, Arizona State University (2018).

Schön, Y., J. N. Voss, M. Wildermuth, A. Schneider, S. T. Skacel, M. P. Weides, J. H. Cole, H. Rotzinger and A. V. Ustinov, "Rabi oscillations in a superconducting nanowire circuit", npj Quantum Materials **5**, 1, 1–5, URL `https://www.nature.com/articles/s41535-020-0220-x`, number: 1 Publisher: Nature Publishing Group (2020).

Scott, D., "The standard cosmological model", Canadian Journal of Physics **84**, 6-7, 419–435 (2006).

Semenov, A., B. Günther, U. Böttger, H.-W. Hübers, H. Bartolf, A. Engel, A. Schilling, K. Ilin, M. Siegel, R. Schneider *et al.*, "Optical and transport properties of ultrathin nbn films and nanostructures", Physical Review B **80**, 5, 054510 (2009).

Serniak, K., M. Hays, G. de Lange, S. Diamond, S. Shankar, L. D. Burkhart, L. Frunzio, M. Houzet and M. H. Devoret, "Hot Nonequilibrium Quasiparticles in Transmon Qubits", Physical Review Letters **121**, 15, 157701, URL `https://link.aps.org/doi/10.1103/PhysRevLett.121.157701`, publisher: American Physical Society (2018).

Serra, P., O. Doré and G. Lagache, "DISSECTING THE HIGH-zINTERSTELLAR MEDIUM THROUGH INTENSITY MAPPING CROSS-CORRELATIONS", The Astrophysical Journal **833**, 2, 153, URL `https://doi.org/10.3847/1538-4357/833/2/153` (2016).

Shan, W., S. Shi, T. Matsunaga, M. Takizawa, A. Endo, T. Noguchi and Y. Uzawa, "Design and development of sis mixers for alma band 10", IEEE Transactions on Applied Superconductivity **17**, 2, 363–366 (2007).

Shu, S., N. Klimovich, B. H. Eom, A. D. Beyer, R. B. Thakur, H. G. Leduc and P. K. Day, "Nonlinearity and wide-band parametric amplification in a (nb,ti)n microstrip transmission line", Physical Review Research **3**, 2 (2021).

Sidorova, M., A. D. Semenov, H.-W. Hübers, S. Gyger, S. Steinhauer, X. Zhang and A. Schilling, "Magnetoconductance and photoresponse properties of disordered nbtin films", Physical Review B **104**, 18 (2021).

Sizov, F., "Terahertz radiation detectors: The state-of-the-art", Semiconductor Science and Technology **33**, 12, 123001 (2018).

Stolen, R. and J. Bjorkholm, "Parametric amplification and frequency conversion in optical fibers", IEEE Journal of Quantum Electronics **18**, 7, 1062–1072 (1982).

Suleymanzade, A., *MILLIMETER WAVE PHOTONS FOR HYBRID QUANTUM SYSTEMS*, Ph.D. thesis (2021).

Swenson, L. J., P. K. Day, B. H. Eom, H. G. Leduc, N. Llombart, C. M. McKenney, O. Noroozian and J. Zmuidzinas, "Operation of a titanium nitride superconducting microresonator detector in the nonlinear regime", Journal of Applied Physics **113**, 10, 104501 (2013).

Swinyard, B. M., E. T. Polehampton, R. Hopwood, I. Valtchanov, N. Lu, T. Fulton, D. Benielli, P. Imhof, N. Marchili, J.-P. Baluteau, G. J. Bendo, M. Ferlet, M. J. Griffin, T. L. Lim, G. Makiwa, D. A. Naylor, G. S. Orton, A. Papageorgiou, C. P. Pearson, B. Schulz, S. D. Sidher, L. D. Spencer, M. H. D. v. d. Wiel and R. Wu, "Calibration of the Herschel SPIRE Fourier Transform Spectrometer", Monthly Notices of the Royal Astronomical Society **440**, 4, 3658–3674, URL `https://doi.org/10.1093/mnras/stu409` (2014).

Takita, M., A. D. Córcoles, E. Magesan, B. Abdo, M. Brink, A. Cross, J. M. Chow and J. M. Gambetta, "Demonstration of weight-four parity measurements in the surface code architecture", Phys. Rev. Lett. **117**, 210505, URL `https://link.aps.org/doi/10.1103/PhysRevLett.117.210505` (2016).

Tinkham, M., *Introduction to Superconductivity* (Dover Publications, 2014), 2 edn.

Tinkham, M., *Introduction to superconductivity* (Dover Publications, 2015).

Usadel, K. D., "Generalized diffusion equation for superconducting alloys", Physical Review Letters **25**, 8, 507–509 (1970).

Uzawa, Y., Y. Fujii, T. Kojima, M. Kroug, W. Shan, S. Ezaki, A. Miyachi, H. Kiuchi and A. Gonzalez, "Superconducting receiver technologies supporting alma and future prospects", Radio Science **56**, 5 (2021).

Vijay, R., J. D. Sau, M. L. Cohen and I. Siddiqi, "Optimizing anharmonicity in nanoscale weak link josephson junction oscillators", Phys. Rev. Lett. **103**, 087003 (2009).

Visbal, E. and A. Loeb, "Measuring the 3d clustering of undetected galaxies through cross correlation of their cumulative flux fluctuations from multiple spectral lines", Journal of Cosmology and Astroparticle Physics **2010**, 11, 016–016, URL `https://doi.org/10.1088/1475-7516/2010/11/016` (2010).

Vissers, M. R., R. P. Erickson, H.-S. Ku, L. Vale, X. Wu, G. C. Hilton and D. P. Pappas, “Low-noise kinetic inductance traveling-wave amplifier using three-wave mixing”, Applied Physics Letters **108**, 1, 012601 (2016).

Vool, U. and M. Devoret, “Introduction to quantum electromagnetic circuits”, International Journal of Circuit Theory and Applications **45**, 7, 897–934 (2017).

Wandui, A., J. J. Bock, C. Frez, M. Hollister, L. Minutolo, H. Nguyen, B. Steinbach, A. Turner, J. Zmuidzinas, R. O’Brient and et al., “Thermal kinetic inductance detectors for millimeter-wave detection”, Journal of Applied Physics **128**, 4, 044508 (2020).

Wheeler, J., S. Hailey-Dunsheath, E. Shirokoff, P. S. Barry, C. M. Bradford, S. Chapman, G. Che, J. Glenn, M. Hollister, A. Kovács, H. G. LeDuc, P. Mauskopf, R. McGeehan, C. M. McKenney, R. O’Brient, S. Padin, T. Reck, C. Ross, C. Shiu, C. E. Tucker, R. Williamson and J. Zmuidzinas, “SuperSpec: development towards a full-scale filter bank”, in “Millimeter, Submillimeter, and Far-Infrared Detectors and Instrumentation for Astronomy VIII”, edited by W. S. Holland and J. Zmuidzinas, vol. 9914, pp. 904 – 912, International Society for Optics and Photonics (SPIE, 2016), URL `https://doi.org/10.1117/12.2233798`.

Wiedner, M. C., I. Mehdi, A. Baryshev, V. Belitsky, V. Desmaris, A. M. DiGiorgio, J.-D. Gallego, M. Gerin, P. Goldsmith, F. Helmich and et al., “A proposed heterodyne receiver for the origins space telescope”, IEEE Transactions on Terahertz Science and Technology **8**, 6, 558–571 (2018).

Winkel, P., K. Borisov, L. Grünhaupt, D. Rieger, M. Spiecker, F. Valenti, A. V. Ustinov, W. Wernsdorfer and I. M. Pop, “Implementation of a transmon qubit using superconducting granular aluminum”, Phys. Rev. X **10**, 031032, URL `https://link.aps.org/doi/10.1103/PhysRevX.10.031032` (2020).

Zhang, L., L. You, L. Ying, W. Peng and Z. Wang, “Characterization of surface oxidation layers on ultrathin nbtin films”, Physica C: Superconductivity and its Applications **545**, 1 – 4, URL `http://www.sciencedirect.com/science/article/pii/S0921453417300588` (2018).

Zmuidzinas, J., “Cramér–rao sensitivity limits for astronomical instruments: implications for interferometer design”, J. Opt. Soc. Am. A **20**, 2, 218–233, URL `http://josaa.osa.org/abstract.cfm?URI=josaa-20-2-218` (2003).

Zmuidzinas, J., “Superconducting microresonators: Physics and applications”, Annual Review of Condensed Matter Physics **3**, 1, 169–214 (2012).

Zmuidzinas, J. and P. Richards, “Superconducting detectors and mixers for millimeter and submillimeter astrophysics”, Proceedings of the IEEE **92**, 10, 1597–1616 (2004).

Zorin, A., “Flux-driven josephson traveling-wave parametric amplifier”, Physical Review Applied **12**, 4 (2019).

APPENDIX A

HAMILTONIAN CALCULATION

A Kineticon qubit is very similar to an LC resonator circuit, save for the inductive part of the circuit, which is non-linear. A simple Kineticon qubit circuit can be imagined as in Fig. A.1, with one active node and no current bias. Defining a branch flux at this node, the kinetic inductance of the nanowire in the weak anharmonic limit, $\Phi \approx L_{0k} I$ can be written as Zmuidzinas (2012)

$$L_k(\Phi) \approx L_{0k}\left(1 + \frac{\Phi^2}{\phi_*^2}\right) \tag{A.1}$$

where L_{0k} is the kinetic inductance with zero bias and $\phi_* \equiv I_* L_{0k}$ where I_* is a characteristic current parameter of the nonlinearity.

The energy stored in the capacitor and the nonlinear inductor can be found using

$$E(t) = \int_{-\infty}^{t} v_b(t') i_b(t') dt' \tag{A.2}$$

where v_b and i_b are the voltage and current of the branch, respectively (Devoret (1997)). Calculated energies are as follows

$$U_C = \frac{1}{2} C \dot{\Phi}^2 \tag{A.3}$$

$$U_L \approx \frac{1}{2L_{k0}}\left(\Phi^2 - \frac{\Phi^4}{\phi_*^2}\right) \tag{A.4}$$

The Lagrangian is given by

$$\mathcal{L} = U_C - U_L = \frac{1}{2} C \dot{\Phi}^2 - \frac{1}{2L_{k0}}\left(\Phi^2 - \frac{\Phi^4}{\phi_*^2}\right). \tag{A.5}$$

Now using Legendre transformation $\mathcal{H} = \dot{\phi} Q - \mathcal{L}$ we can write the Hamiltonian as follows

$$\mathcal{H} = \frac{Q^2}{2C} + \frac{1}{2L_{k0}}\left(\Phi^2 - \frac{\Phi^4}{\phi_*^2}\right). \tag{A.6}$$

We can quantize the circuit by replacing Q and ϕ with their quantum operators that satisfy the following commutation relation

$$[Q, \Phi] = -i\hbar. \tag{A.7}$$

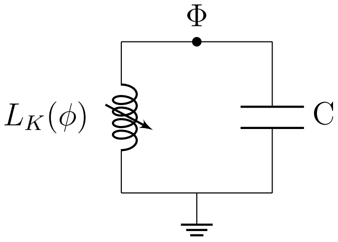

Figure A.1: Circuit diagram of an ideal superconducting LC resonator with the non-linear inductive element.

The Hamiltonian operator now can be written as follows by replacing charge and flux with their quantum operators and multiplying and dividing the inductive energy with flux quantum ϕ_0

$$\tilde{H} = \frac{\tilde{Q}^2}{2C} + \frac{\phi_0^2}{2L_{0k}}\left(\frac{\tilde{\Phi}^2}{\phi_0^2} - \frac{\tilde{\Phi}^4}{\phi_0^2\phi_*^2}\right). \tag{A.8}$$

Defining $E_K \equiv \frac{\phi_0^2}{2L_{k0}}$ and $\frac{\tilde{\Phi}}{\phi_0} \equiv \tilde{\phi}$

$$\tilde{H} = \frac{\tilde{Q}^2}{2C} + E_K\left(\tilde{\phi}^2 - \frac{\phi_0^2}{\phi_*^2}\,\tilde{\phi}^4\right) \tag{A.9}$$

defining λ as $\frac{\phi_0^2}{\phi_*^2}$ we can rewrite the above equation as

$$\tilde{H} = \frac{\tilde{Q}^2}{2C} + E_K\left(\tilde{\phi}^2 - \lambda\,\tilde{\phi}^4\right) \tag{A.10}$$

In the second quantization language, we can define the following creation and annihilation operators

$$\tilde{a} = \frac{1}{\sqrt{\hbar\omega_r}}\left[\frac{1}{\sqrt{2L_{0k}}}\tilde{\phi} + i\frac{1}{\sqrt{2C}}\tilde{Q}\right] \tag{A.11}$$

$$\tilde{a}^\dagger = \frac{1}{\sqrt{\hbar\omega_r}}\left[\frac{1}{\sqrt{2L_{0k}}}\tilde{\phi} - i\frac{1}{\sqrt{2C}}\tilde{Q}\right]. \tag{A.12}$$

The reduced charge and flux operators in terms of $\tilde{a}$ and $\tilde{a}^\dagger$ are given by

$$\tilde{q} = \frac{\tilde{Q}}{q_{zpf}} = i\left(\tilde{a} - \tilde{a}^\dagger\right) \tag{A.13}$$

$$\tilde{\phi} = \frac{\tilde{\Phi}}{\varphi_{zpf}} = \left(\tilde{a} + \tilde{a}^\dagger\right). \tag{A.14}$$

where $Z_0 = \sqrt{\frac{L_{0k}}{C}}$ and we defined $\varphi_{zpf} = \sqrt{\frac{\hbar Z_0}{2}}$ and $q_{zpf} = \sqrt{\frac{\hbar}{2Z_0}}$ as zero-point fluctuations of flux and charge respectively.

The Hamiltonian of our weakly anharmonic oscillator (AHO) becomes

$$\tilde{H} = \hbar\omega_r \left[a^\dagger a + \frac{1}{2} + \frac{1}{4}\lambda \left(a^\dagger + a \right)^4 \right] \tag{A.15}$$

where $\omega_r = \sqrt{\frac{1}{L_{0k}C}}$.

APPENDIX B

CIRCUIT DIAGRAMS

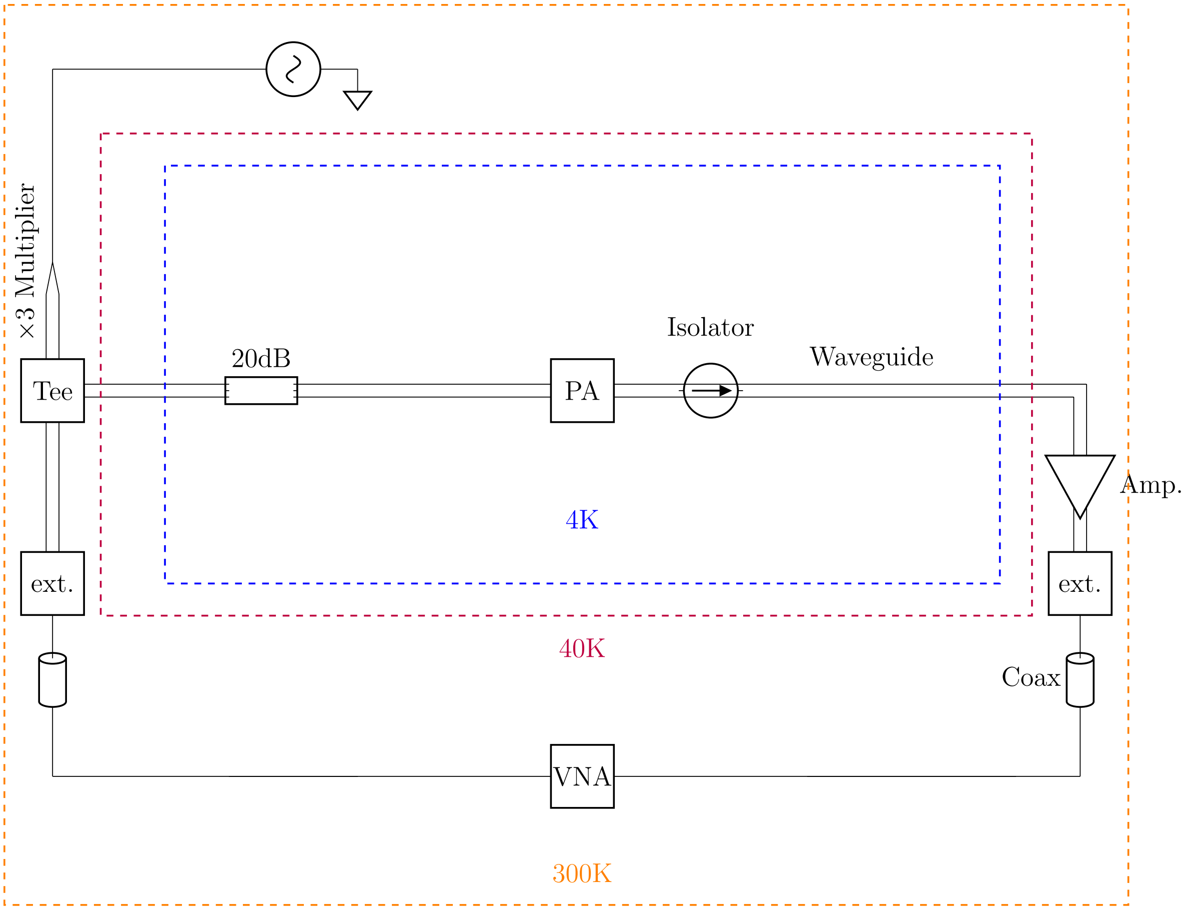

Figure B.1: Circuit diagram of the measurement test setup used for W-band kinetic inductance parametric amplifier.